THE IMPACT OF VIBRATIONS ON MOBILE INFRASOUND SENSING AND THE DEVELOPMENT OF A CUSTOM SENSOR PACKAGE

By

BRYCE B. LINDSEY

Bachelor of Science in Aerospace Engineering
Oklahoma State University
Stillwater, OK
2021

Bachelor of Science in Mechanical Engineering
Oklahoma State University
Stillwater, OK
2021

Submitted to the Faculty of the
Graduate College of the
Oklahoma State University
in partial fulfillment of
the requirements for
the Degree of
MASTER OF SCIENCE
May, 2023

THE IMPACT OF VIBRATIONS ON MOBILE INFRASOUND SENSING AND THE DEVELOPMENT OF A CUSTOM SENSOR PACKAGE

Thesis Approved:

Dr. Brian Elbing

Thesis Advisor

Dr. Jamey Jacob

Dr. Ryan Paul

ACKNOWLEDGMENTS

First, I would like to thank my parents, siblings, and extended family for their endless support and love. They've always been in my corner, and I feel lucky to call them my family. I would also like to thank all of the Marines I served alongside during my time in the Marine Corps; you all taught me how to find joy and humor in times of adversity. Additionally, I'd like to thank the other students and collaborators in the Experimental Flow Physics Lab for their assistance, with a special thanks to Trevor Wilson, Zac Yap, and Brandon White for their extensive guidance.

Furthermore, I'd like to thank the members of my committee as well as all of the faculty I was able to work with at Oklahoma State University. I'd like to single out Dr. Elbing in this regard for all of his professional and personal guidance throughout my time in his lab. Dr. Elbing cares for his team as much as he values good research, and he is a crucial role model for all of his students.

Lastly, I'd like to thank my fiancé, Lauren, for constantly bearing the weight of living with and loving someone as busy and distracted as I am. My graduate school journey has been as demanding of her as it was of me, and she tackled it with a smile.

Acknowledgments reflect the views of the author and are not endorsed by committee members or Oklahoma State University.

Name: BRYCE B. LINDSEY

Date of Degree: MAY, 2023

Title of Study: THE IMPACT OF VIBRATIONS ON MOBILE INFRASOUND SENSING AND THE DEVELOPMENT OF A CUSTOM SENSOR PACKAGE

Major Field: MECHANICAL AND AEROSPACE ENGINEERING

Abstract: Acoustic frequencies below 20 Hz, referred to as "infrasound", are emitted by various phenomena. Events such as volcanoes, tornadoes, earthquakes, industrial processes, detonations, and bolides, can be analyzed via the infrasound they produce. Researchers often use fixed-location sensors to observe correlations between infrasound signals and the location, strength, and behavior of these events. However, recent efforts to deploy infrasound sensors on-board a storm-chasing vehicle (targeting tornado-induced infrasound) have yielded unexpected results. Following an initial investigation, it was suspected that vibrations were responsible for abnormal spectral content observed while deployed on-board the vehicle. To explore the mitigation of vibrations on mobile infrasound acquisition, a custom seismo-acoustic sensor was constructed: the Cloud-capable Low-cost Acoustic and Seismic sensor Package (CLASP). CLASP consists of a pressure transducer mounted orthogonally to the dominant vibration vector component on common mobile platforms and utilizes an open source cloud-based storage protocol, both of which aim to optimize the sensor package for mobile infrasound measurements. Following its construction, data collected from both CLASP and a previously fielded sensor were compared during lab and field testing: acoustic and acceleration data was acquired while mounted to an unmanned aerial vehicle, automobile, and shaker table. Throughout controlled lab tests, the CLASP design helped decouple vibrations from the acoustic signals collected from the pressure transducer. However, field tests revealed that the primary contributor to seismo-acoustic coupling is static pressure oscillations due to changes in altitude as the package vibrates; a mechanism that is not mitigated by the CLASP design. Ultimately, CLASP and its source code, components, and methodology are presented in this work, as well as a summary of guidelines for infrasound data acquisition in vibrationally-active environments.

TABLE OF CONTENTS

Chapter Page

LIST OF TABLES

LIST OF FIGURES

Figure Page

Figure Page

CHAPTER I

INTRODUCTION

1.1 Motivations

Certain energetic phenomena such as volcanoes, detonations, and tornadoes, can be studied via the sound they emit in certain frequency bands. The frequencies of interest in the work presented are in the "infrasound" regime, covered in Section 1.3.1. Most existing studies acquire infrasound with fixed-location sensors [1, 2, 3, 4, 5, 6]. However, extending infrasound acquisition to mobile platforms would provide some advantages over fixed-location sensing. For example, mobile infrasound sensing could give researchers the flexibility of varying the location of sensors during deployments, potentially *targeting* events of interest, rather than leaving expensive assets in fixed locations for extended periods of time. Additionally, utilizing mobile packages could substantially increase the quantity of data collected near infrasound-emitting events which, in turn, may further our understanding of the underlying dynamics at play.

Recently, multiple mobile infrasound sensing packages were deployed on-board a storm chasing vehicle and collected data near a tornado [7, 8]. However, unexpected behavior was observed in the data collected by both sensor packages. Ultimately, the nature in which vehicles, and mobile platforms in general, affect infrasound sensors is an area of research that has not been extensively explored. To determine the validity of existing mobile infrasound measurements, a custom seismo-acoustic sensor package was needed and experiments were required to establish an understanding of mobile infrasound sensing and the challenges that accompany the task. Additionally, this insight could establish guidelines for future sensor

design endeavors.

This thesis is composed of six chapters. Chapter I introduces key concepts and background material. Chapters II and IV are closely related in that Chapter II provides information about a mobile infrasound sensing package that served as momentum for the custom seismo-acoustic sensor presented in Chapter IV which was, at least partially, created for the purposes of this thesis. Chapter III covers the equipment and methods used to complete the experiments that were performed. Chapter V covers the experiments performed in support of this thesis, and Chapter VI summarizes the implications of the experimental results and recommended future work.

1.2 Nomenclature and Common Acronyms

Throughout this thesis, symbols represented data in plots and parameters in equations. Additionally, acronyms were used during contextual discussions and when results were presented. Table 1 and Table 2 provide the symbols and acronyms, respectively, used in this paper.

Unit / Symbol	**Description**
c	local speed of sound
C	capacitance (acoustic, electrical)
η	shear viscosity
f	frequency
γ	symbol for cross-power spectral density
$\hat{g}$	gravity unit vector
Hz	unit of frequency
l	length
Pa	Pascals
Φ	symbol for power spectral density
R	resistance (acoustic, electrical)
r	radius
ρ	density
V	volume

Table 1: Units and symbols that will be seen throughout this work.

Acronym	Description
ADC	Analog-to-Digital Converter
CLASP	Cloud-capable Low-cost Acoustic and Seismic sensor package
CSD	Cross-power Spectral Density
DAQ	Data Acquisition (device)
DFT	Discrete Fourier Transform
EFPL	Experimental Flow Physics Lab
FFT	Fast Fourier Transform
GLINDA	Ground-based Local Infrasound Data Acquisition unit
GPS	Global Positioning System
IMU	Inertial Measurement Unit
NAPD	Normal Acceleration Percent Difference
OSU	Oklahoma State University
PCB	Printed Circuit Board
PSD	Power Spectral Density
SBC	Single Board Computer
UAV	Unmanned Aerial Vehicle
USRI	Unmanned Systems Research Institute
VCR	Vibration Coupling Reduction

Table 2: Acronyms that will be seen throughout this work.

1.3 Literature Review

1.3.1 Infrasound

Acoustic pressure waves, or sound waves, influence many aspects of our lives. The music we listen to, the cars honking in the street, and the planes flying above, all emit sound waves in the audible range (sound that the typical human ear can detect). However, these waves are not confined to what humans can hear. Similar to electromagnetic waves, sound waves span a broad spectrum, and sound below that of the nominal audible spectrum of humans is referred to as "infrasound". Infrasound is typically classified as pressure waves with frequencies below 20 Hz, and is shown accordingly among various frequencies in Figure 1.

There are many sources of infrasound, both naturally occurring events and man-made byproducts, and many of these sources are analyzed and/or characterized by the infrasound they produce. For example, the intensity and style of spewing events like volcanoes and gey-

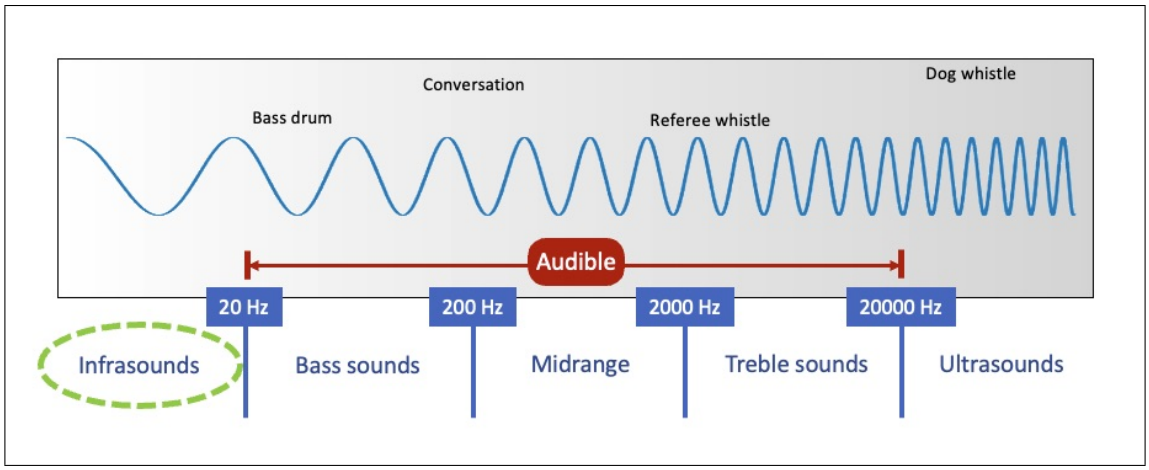

Figure 1: Acoustic Spectrum

sers can be determined via the infrasound they produce [4, 9, 3, 10]. Additionally, infrasound emitted from events related to seismic activity, like earthquakes and avalanches, can help determine the location, duration, and energy associated with such events [5, 11, 10]. Furthermore, events that closely interact with Earth's atmosphere such as storms, ocean wave interaction, atmospheric turbulence, meteors, and tornadoes, can also be analyzed by the infrasound they produce [12, 10, 13, 2, 14, 15, 16, 17]. Lastly, anthropomorphic events such as vehicle traffic, industrial processes, detonations, and fireworks provide useful information via the infrasound produced by these events [18, 19, 2, 6]. Table 3 is provided to summarize the information gathered throughout the literature review portion of infrasound sources.

Note, many of the sources in Table 3 also produce sound in the audible range. Most folks have heard the rumble of a thunderstorm, or the echo of a plane passing above. However, there is another useful aspect of infrasound analyses: attenuation. An advantage of analyzing the sources in Table 3 by the infrasound they produce, instead of the audible frequencies, is the low attenuation characteristic of infrasound waves. As infrasound propagates through the atmosphere, its long wavelengths preserve energy better than high-frequency constituents [20, 12]. Many of the sources in Table 3 are high-energy and potentially dangerous events to be near; thus, collecting data at a distance via the infrasound emitted is an advantage.

Source	**Utility of Using Infrasound Analyses**	**Nominal Dominant Frequencies**
Volcano	Estimate energy output and location, further understand the explosion dynamics and impulsivity involved	0.3-10 Hz
Tornado	Event detection and location estimation, potential warning mechanism, size estimation	5-10 Hz
Microbarom	Atmospheric model development, array testing	0.1-0.3 Hz
Lightning/ Thunderstorms	Approximate location and size of a storm, explore electrical activity present	0.1-20 Hz
Geyser	Estimate energy output, localization of source, investigate geological interactions	1-20 Hz
Avalanche	Determine duration, location, and areas of high occurrences	1-10 Hz
Earthquake	Detection, distinguish signals from epicenter and other radiation points	2-8 Hz
Fireworks/ Explosions	Determine frequency of occurrence and general location, determine energy output	1-20 Hz
Meteor Entry	Approximate size, impact region, and entry type	0.1-10 Hz
Train/Air/Road Traffic	Determine time and duration of high activity	0.1-20 Hz
Industrial Processes	Determine time and duration of high activity	0.1-20 Hz

Table 3: Infrasound sources.

1.3.2 Infrasound Sensing Devices

Throughout both the literature review portion and experimental portion of this thesis, exposure to several infrasound sensors[1] occurred; most of all, the Gem Infrasound Logger [21] and the Chaparral Physics Model 24 [22]. Other commonly used infrasound sensors can be seen in Table 4. While Table 4 by no means summarizes the complete selection of infrasound sensors available to researchers, it does provide a baseline for the reader to reference throughout this thesis; specifically, common prices and characteristics found in this class of sensors.

Model	**Minimum Price**	**Notable Characteristics**
Infiltec INFRA20 [23]	> \$400	Plug-and-play option using the free software AmaSeis (Windows only)
GEM Infrasound Logger [21]	> \$1600	Portable, low power draw and local storage for long deployments
Chaparral Model 24 [22]	> \$2700^{+}	Low noise floor, high resolution, low power draw
Chaparral Model 60 [24]	> \$2700^{+}	Low noise floor, high resolution, low power draw, small footprint
Hyperion 5313A/5113A [25]	> \$6000^{+}	High resolution, low noise floor, low power draw, vibration compensation, and thermal resilience
B&K 4193 [26]	> \$3700^{+}	Large frequency response range, thermal resilience, small footprint, impact resistant from 1m fall

Table 4: Various infrasound sensors, where "+" denotes mic-only minimum prices and require additional data acquisition equipment and wiring.

1.3.3 Seismo-Acoustic Coupling

Vibrations affect the behavior of a microphone's response, with the direction of the applied vibration being a primary contributor to this type of coupling [27]. Researchers have been

[1]The terms "microphone", "microbarometer", and "infrasound sensor" are used somewhat synonymously among infrasound researchers. Due to fine resolutions and intended applications, most of the sensors covered in this thesis are more so members of the "microbarometer" and "infrasound sensor" group than the "microphone" group; a small nuance the reader might find useful.

studying the effects of vibrations on microphones since the 1970s, and an ongoing endeavor in the time since has been developing methods to counteract the effects of vibrations on microphones operating in the audible range among small sensors, such as in hearing aids and cameras [28, 29]. While progress has been made in this area of research, there are still plenty of researchers and companies working on this issue. For example, the well-known adventure camera company, GoPro, applied for patents in 2021 for methods and hardware used to reduce the effects of vibrations on their cameras' microphones [30]. Thus, it is still an active research area and new solutions are desired.

Unfortunately, infrasound sensors, when compared to microphones dedicated to audible frequencies, face an additional complication: the span of frequencies considered. Audible microphones focus on the frequency range of 20-20000 Hz (or a smaller range if the microphone is low-fidelity). However, as discussed in Section 1.3.1, infrasound sensors are focused on frequencies between 0.1-20 Hz. Therefore, the signals acquired by an infrasound sensor caused by mechanical vibration have a greater chance of affecting a higher *percentage* of the frequencies of interest when compared to the larger audible range of frequencies; making the coupling of vibrations and an acoustic signal more likely to contaminate infrasound bands of interest.

Another challenge presented to infrasound analyses via influences from vibrations is simple: not many researchers are working on this issue. In fact, much of the community conducting infrasound research prefer to have vibrationally-coupled sensors, as this allows for the detection of the seismo-acoustically coupled "local" infrasound (as opposed to epicentral and secondary infrasound) emitted by seismic events [2]. There is, however, an infrasound sensor product line that is specified to be immune to vertical vibrations: the Hyperion 5000 series[2] [31]. How exactly the Hyperion 5000 series goes about this is unclear, as documentation is limited due to proprietary information and limited testing available to the public.

[2]Ambiguity exists in literature. Tests were performed with capped pressure inlets [31], suggesting the sensors are not completely vibrationally decoupled (i.e., still susceptible to static pressure oscillations via height changes from vibrations)

Additionally, one can speculate that this decoupled design requires expensive hardware and an elaborate internal layout based on the price-point of these sensors, seen in Table 4.

The various mechanisms by which vibrations can affect acoustic signals is an area of research with very few published papers; the majority, of which, focus on the audible range of acoustic frequencies. As previously mentioned, seismic events can be detected via static pressure changes due to a physical displacement of a sensor. However, there could be other mechanisms that produce similar coupling effects. For example, the diaphragm of the sensor could be affected by the change of momentum during shaking. Additionally, components of the sensor (inlet tubes, valves, etc.) could vibrate, affecting the acoustic signal acquired by the pressure transducer. Ultimately, exploring the various mechanisms at play in seismo-acoustic coupling is one of the primary focuses of this paper, and more information on this investigation will be expanded on in Chapter V.

1.4 Contextual Field Data

The information presented in this section will provide the reader with context and relevant results from prior projects/experiments, which helped refine the methods used and experiments performed in this thesis. Section 1.4.1 covers a high-fidelity infrasound array (fixed-location sensors) that has collected data emitted by a tornado-producing storm system, while section 1.4.2 informs the reader of a previously constructed mobile infrasound sensing package that collected data in close range of a tornado while on-board an automobile.

1.4.1 OSU1 Infrasound Array

The Experimental Flow Physics Lab (EFPL) [32] at Oklahoma State, of which the primary author of this thesis is a member, maintained an infrasound array, termed "OSU1", from 2016-2022. The array consisted of 3 fixed-location Chaparral 24 microbarometers which utilized porous hoses for wind-noise reduction, and was operational for the majority of the 6 years (other than occasional outages due to maintenance and damage). The three sensors

that made up OSU1 can be seen in be seen in Figure 2a, with more details of the sensors seen in the other panels of this figure. OSU1 captured data from many events; several of

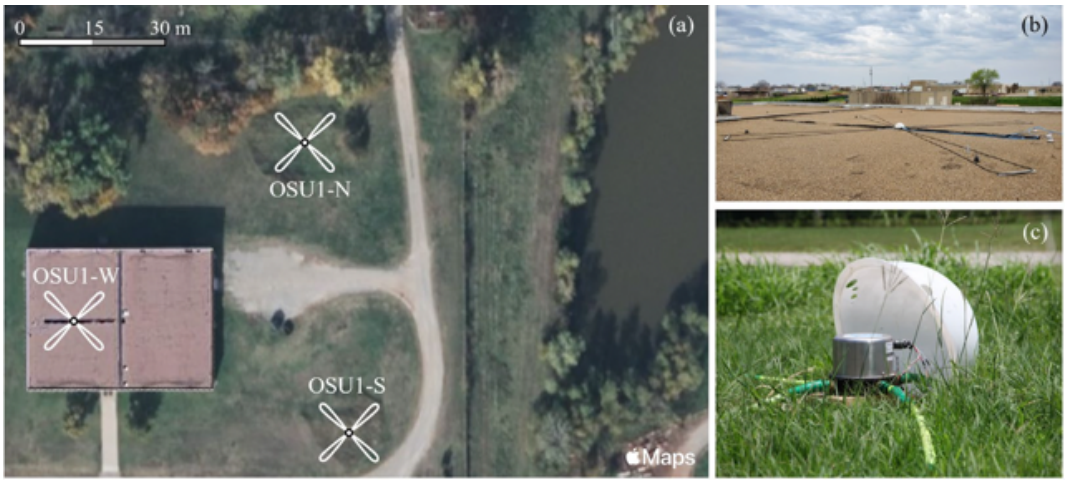

Figure 2: (a) Satellite view of the sensors in OSU1. (b) Image of OSU1-W in its nominal configuration. (c) Image of the exposed Chaparral 24 at the OSU1-S location. Figure reproduced from Wilson et al. [2].

which were analyzed via infrasound and low-audible production, such as tornadoes, several non-tornadic storm systems, fireworks, explosions, and earthquakes [18, 14, 2]. A particular event which is especially relevant to the work presented in this thesis is a tornado-formation event captured by OSU1 in 2017 [1]. The data collected during this event shows a swell of infrasound centered at 8.3 Hz with ≈18 dB increase in spectral power relative to the levels prior to the swell, summarized by Figure 3.

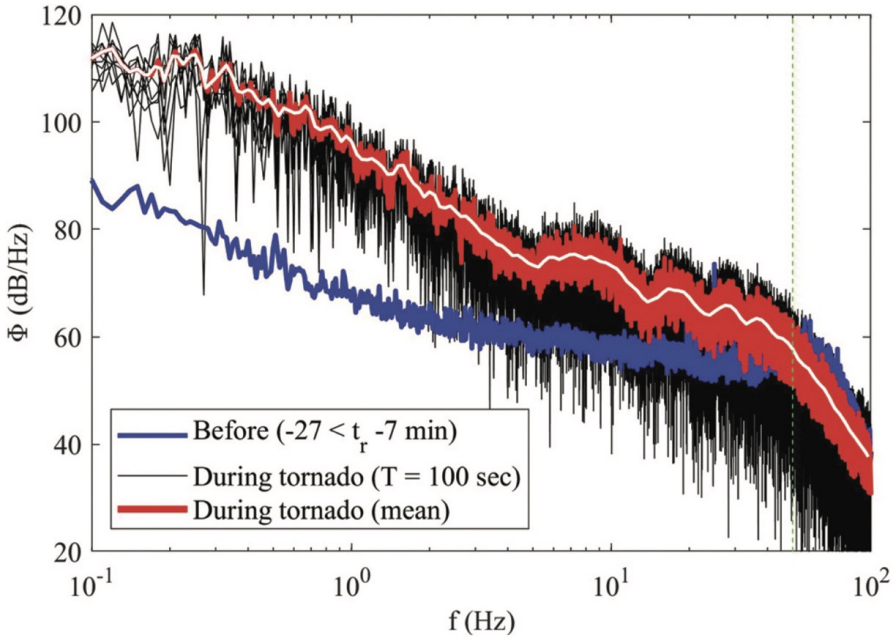

Figure 3: Tornado-related spectra prior to and during tornado formation recorded by OSU1. Figure reproduced from Elbing et al. [1].

In the interest of this thesis, the measurements taken by OSU1 are held in high regard. The high-fidelity instrumentation used, extensive verification in previously mentioned citations, fixed mounting methods for each sensor, and the vibration isolation pads used under each sensor, are all factors that make the data collected by OSU1 crucial references throughout the investigation of the mobile infrasound sensing and its challenges.

1.4.2 GLINDA1

Another system that has been utilized by the EFPL is the Ground-based Local Infrasound Data Acquisition system, or "GLINDA" for short. This section (adapted from White [8] and White et al. [7]) summarizes the implementation and data collected by the first iteration of the GLINDA sensor package, termed "GLINDA1". GLINDA1 was primarily constructed by Brandon White, a previous graduate student at Oklahoma State University, for his thesis [8]. GLINDA1 consisted of a Chaparral 24 sensor, and a Raspberry Pi 3B running the package, which was installed in the back of a storm-chasing vehicle (Val and Amy Castor's

News9-OKC storm-chasing truck), seen in Figure 4. GLINDA1 collected data on-board the storm-chasing vehicle for 4 months but required regular maintenance and interventions to debug issues. After 4 months, detrimental software complications rendered the package nonoperational; specifically, methods to push data to a remote GitHub repository failed, and methods to collect GPS and IMU data became unreliable.

Figure 4: GLINDA1 configured in the News9 storm-chasing vehicle. Figure reproduced from White [8].

Throughout its operational period in the field, GLINDA1 collected data on 2 primary events: a large hail event on 22 May 2020 and an EFU tornado in Lakin, Kansas on 21 May 2020; the latter, of which, will be focused on here. The data collected by GLINDA1 during the Lakin, Kansas tornado can be seen in Figure 5. The reader should note the differences between Figure 3 and Figure 5; specifically, the shift of peak spectral content to higher frequencies in the GLINDA1 data collected during the tornado event. The unexpected structure of the data collected by GLINDA1 was a cause for concern, and more discussion of these results will take place in Chapter II.

After witnessing the unexpected shift in frequencies in the Lakin tornado data, White performed an acoustic response experiment on the storm-chasing vehicle to ensure the truck was not altering the acoustics in the cab where GLINDA1 sat. The results of this experiment can be seen in Figure 6, which imply that the truck's acoustic response was not responsible for the abnormal behavior reported in Figure 5.

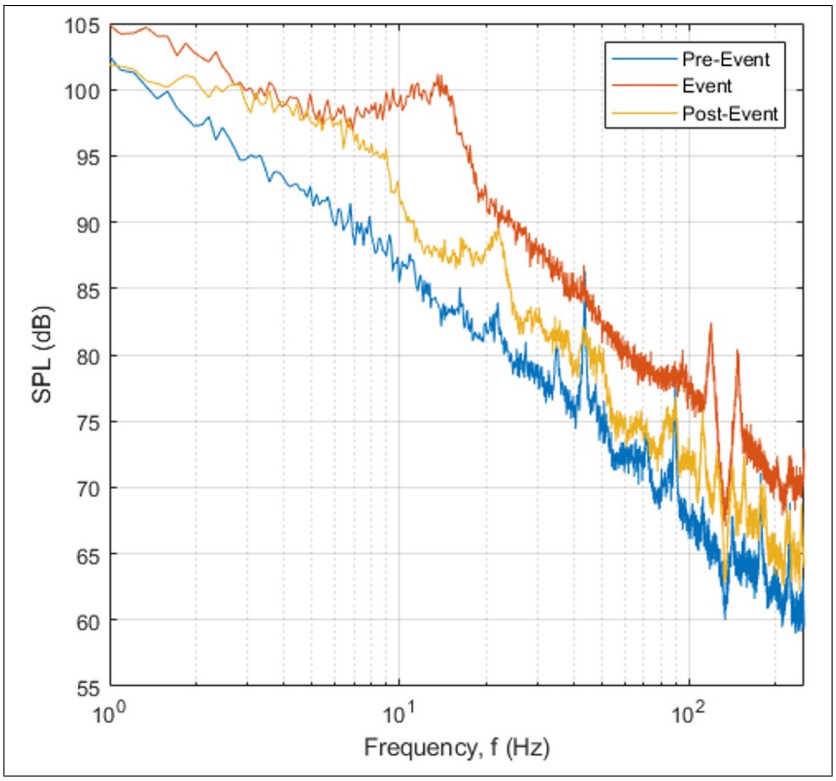

Figure 5: GLINDA1 data collected during 22 May 2020 Lakin, KS tornado. Pre-event = 6:45 pm CST; event = 8:30 pm CST; post-event = 4:30 am (22 May 2020) CST. Hanning windows: 15s, 60% overlap. Figure reproduced from White [33].

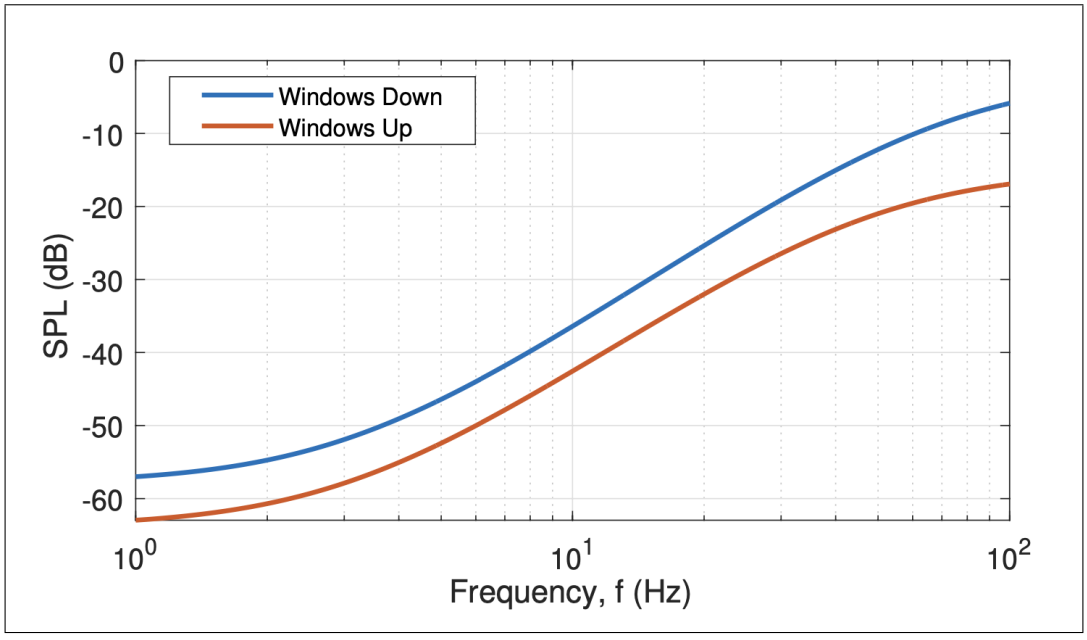

Figure 6: News9 storm-chasing truck acoustic response. Figure reproduced from White [8].

GLINDA1 and the work done by White and his collaborators [33, 7, 8] provided a source of momentum for mobile infrasound measurement endeavors pursued by subsequent members of the EFPL. Much of what this thesis presents, in Chapter IV particularly, was executed successfully thanks to White and his work covered here. However, due to the previously mentioned software issues that occurred during the GLINDA1 campaign, there is missing context for most events GLINDA1 was nearby (i.e., GPS and acceleration data during most events was not successfully collected). Ultimately, GLINDA1 was replaced by its successor, "GLINDA2".

CHAPTER II

GLINDA2

Following its short deployment (and the completion of White's graduate degree), GLINDA1 was replaced by the appropriately-named second iteration of the sensor package, "GLINDA2." The transition from GLINDA1 to GLINDA2 was accompanied by many changes to the system and it was at this time that the author of this thesis became the lead researcher in charge of GLINDA's operation and maintenance. Details of GLINDA2 and its components will be discussed in Section 2.1, and a comparison of data collected by both GLINDA packages can be found in Section 2.2.

2.1 GLINDA2 Details

This section covers the design changes moving from GLINDA1 to GLINDA2 and the insight gained from an additional deployment of a mobile infrasound data acquisition package. GLINDA2 was deployed to the field in March of 2022 and was configured in the News 9 storm-chasing vehicle in a similar manner as GLINDA1, seen in Figure 7.

GLINDA2 was somewhat of a "Frankenstein" sensor package, as it consisted of various components from different sensor packages. It utilized components from a Gem Infrasound Logger (covered in detail in Section 3.1) to replace the Chaparral 24 used in the GLINDA1 system, but continued to use most of the other hardware used in GLINDA1. However, major source-code adjustments were made and new methods to push data to a cloud-based storage repository were implemented. These modifications led to a successful deployment that lasted more than a year with very few issues recording acoustic and GPS data, and no issues pushing data to the remote server. It is worth noting that an inertial measurement

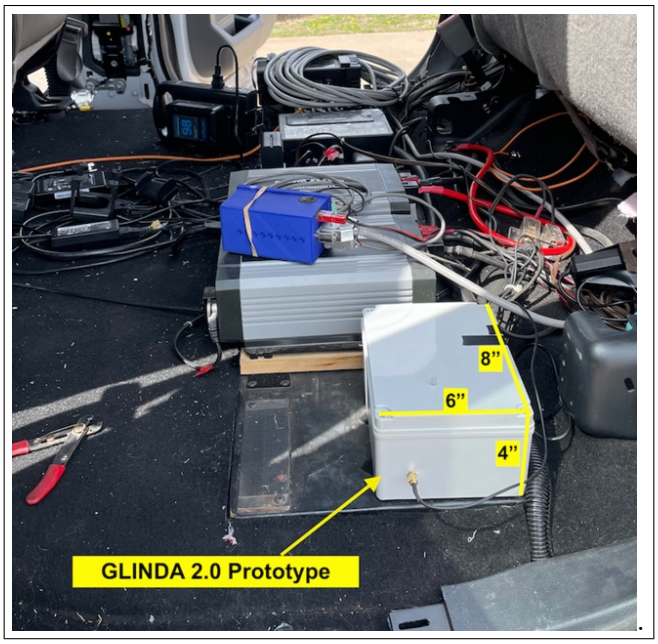

Figure 7: GLINDA2 configured in the storm-chasing vehicle.

unit (IMU) was not included in the GLINDA2 package, as the knowledge required to outfit this type of sensor onto the Gem microbarometer (which does not include an IMU) was not gained until after GLINDA2 had been deployed. Figure 8 provides the reader with an annotated view of the components that made up GLINDA2.

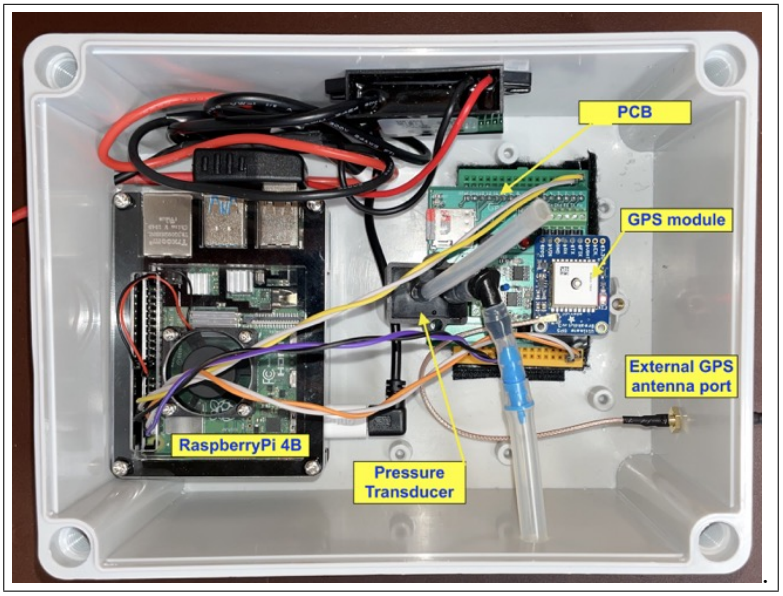

Figure 8: GLINDA2 components.

Like its predecessor, GLINDA2 collected data during many storm and tornado events

while in the field. The most severe event GLINDA2 was able to collect data on was an EF3 tornado in Andover, KS, on 29 April 2022. The 155 mph peak winds produced by this tornado destroyed dozens of residential buildings while it was on the ground for more than 12 miles [34], and Val and Amy Castor were able to get in close proximity to the tornado while GLINDA2 was recording. At 8:38 pm CDT, the Castors were sitting still, within a mile of the tornado, and the moment was captured on their Facebook live-stream video [35]. A screenshot from this video can be seen in Figure 9.

Figure 9: Andover, KS EF3 tornado. Figure adapted from Castor et al. [35].

Three sections of data that GLINDA2 acquired during the Andover, KS tornado were considered during the analysis of the event. The local time, storm state, and vehicle state during these sections of data can be seen in Table 5 and the resulting spectral content of each subset of data can be seen in Figure 10. Immediately, one can see the similar structure present in the data collected by both GLINDA systems (in Figures 5 and 10).

Tornado state	Time	Vehicle state
Active	8:38 pm CDT	≈1 mile from tornado, sitting still
Before storms	2:00 pm CDT	Driving on I-35 (≈75 mph)
After storms	11:50 pm CDT	Sitting still at gas station

Table 5: Times/states during the 29 April 2022 event used for GLINDA2 data analysis.

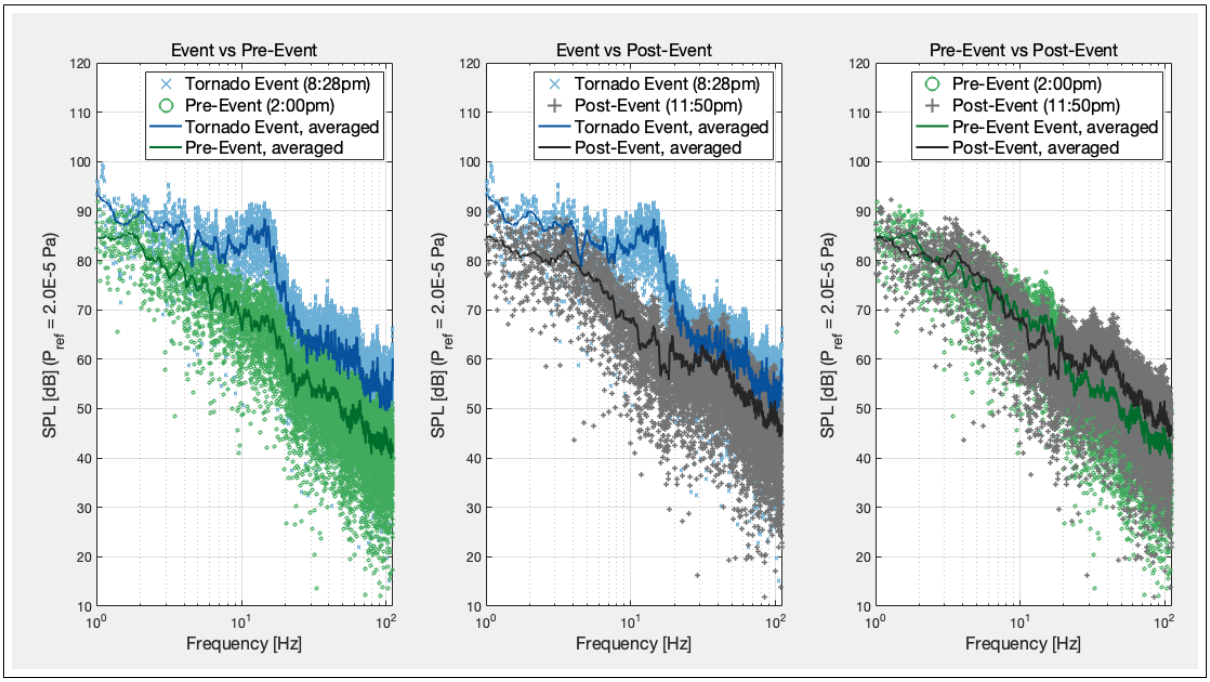

Figure 10: Data collected by GLINDA2 on 29 April 2022.

2.2 Contextual Data - Extended Analysis

Both major tornado events of which GLINDA1 and GLINDA2 collected data on show similar structure in the frequency domain. However, literature suggests that the fundamental frequencies emitted by tornadoes are likely a function of the tornado diameter [16]. Yet, the Lakin and Andover tornadoes were not thought to be the same size; though, it is difficult to say as the Lakin tornado was unclassified on the Enhanced Fujita Scale due to lack of tornado-related damage (its path was in a rural area). A comparison of the power spectral density (covered in Section 3.3) extracted from the data collected by both GLINDA systems during their respective tornado events can be seen in Figure 11. For clarity, the GLINDA2 data in this figure consists of 2.5 minutes of data and the GLINDA1 data in this figure consists of 3.25 minutes of data.

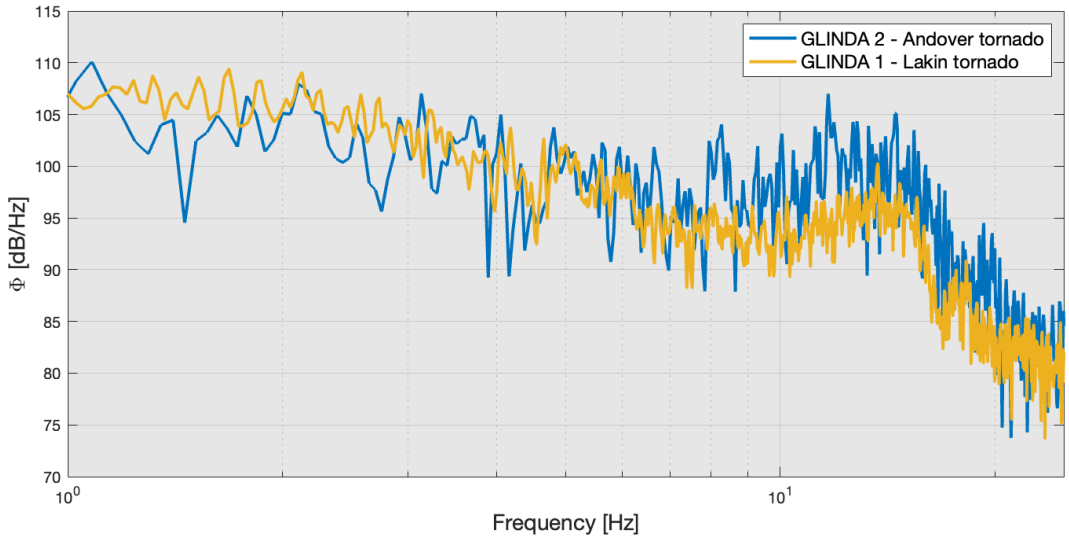

Figure 11: Comparison of infrasound collected by both GLINDA systems during separate tornado events. Hanning window: 30s, 50% overlap.

One can see the similarities among the data sets in Figure 11 which causes some concern considering how much the structure of each signal varies from data collected by OSU1. Unlike the spectral peak in OSU1 data, the signals in Figure 11 show a swell of infrasound centered around a higher frequency (≈13-15 Hz). The discrepancies between both GLINDA systems and OSU1 were a source of skepticism in the validity of the data collected by GLINDA1 and GLINDA2, and these discrepancies triggered a process of considering what other phenomena could cause this structure. Though, the vehicle response experiment performed by White, shown in Figure 6, suggests that the vehicle was not contributing some sort of acoustic resonance. However, persistent infrasound signals throughout hours in the field were observed in the data collected by GLINDA2. A spectrogram (a topic covered in Section 3.3) of the data collected on 29 April 2022 can be seen in Figure 12, and one can see persistent structure in the 15-20 Hz region that may be a function of road conditions. Figure 12 suggests that the driving conditions, or the vehicle state itself, affected GLINDA2 throughout the entire day during the Andover, KS tornado chase; and likely, GLINDA1 during its deployment as well. However, mobile infrasound measurements is an area of research that has few data points (most of which, come from the GLINDA systems). Ultimately, it is speculated that

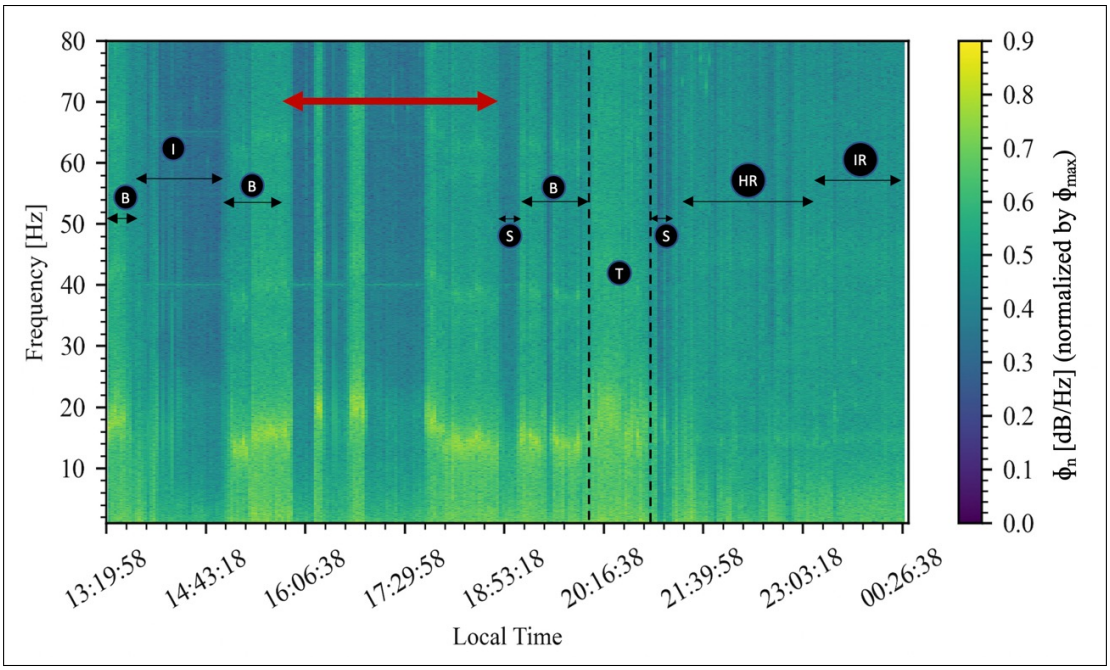

Figure 12: GLINDA2 data collected throughout entire day on 29 April 2022 (Andover tornado). I: Interstate driving; T: driving within 3 miles of tornado; B: county/dirt road driving; S: sitting still; HR: highway driving in rain; IR: interstate driving in rain; Red arrow: GPS error, cannot be certain of road conditions.

vibrations are the primary contributor to the shift in frequencies observed by the GLINDA sensor packages.

Determining how vibrations affected GLINDA1 cannot be done due to the software issues encountered during the GLINDA1 deployment. Additionally, the lack of an IMU present on the Gem components in the GLINDA2 system means context about vibrations affecting GLINDA2 are missing as well. Furthermore, the environment that each GLINDA system was deployed in is a chaotic one. Even if vibration data was gathered during each of the deployments, it would be challenging to precisely determine the mechanisms behind seismo-acoustic coupling; factors like road condition, wind gusts, debris hitting the truck, etc., would have introduced many variables (some of which would have been unknown) to the problem at hand. Thus, controlled lab tests were needed to investigate the effects of vibrations on systems like GLINDA1 and GLINDA2. This realization was the primary driver for the work completed and the results presented in this thesis.

CHAPTER III

METHODS

This chapter covers the equipment, processes, and algorithms used or referenced throughout the experimental portion of this thesis. There are two primary tasks to be covered in this chapter. First of all, the information covering the equipment presented in this chapter should be sufficient enough so that any individual could be able to reproduce the results of this thesis. Additionally, sections in this chapter should provide the reader with a sufficient amount of background information of the algorithms and post-processing techniques used in later portions of this paper; the reader should feel comfortable interpreting the results presented in later sections. Sections 3.1, 3.2 cover a reference sensor and supporting equipment used to execute the experiments performed throughout the work presented in thesis. Section 3.3, on the other hand, provides the reader with the algorithms and post-processing steps used to process the data acquired from the experiments.

3.1 Gem Infrasound Logger

This section (adapted from Anderson et al. [36]) provides a brief summary of the Gem Infrasound Logger, or "Gem" for short. The Gem was briefly mentioned in Chapter I, but further elaboration is required to provide proper context for this thesis as it was the primary reference used during the design of a custom sensor package, discussed in Chapter IV. While much of the scientific community relies on high-fidelity, high-cost equipment, the makers of the Gem say "that when needed, scientists can feasibly design and build their own specialized instruments, and that doing so can enable them to record more and better data at a lower cost" (Anderson et al., 2018); a heap of gratitude goes towards the researchers responsible

for the Gem for sharing their work to the community.

The Gem is unique in that it's an all-in-one solution for remote infrasound recording, as the unit does not require a separate computing platform and DAQ to collect data. To acquire infrasound, the Gem utilizes an affordable differential pressure transducer with a pneumatic filter so that one side of the transducer's diaphragm is exposed to all surrounding acoustic waves, while the other side is only exposed to the surrounding acoustic waves that pass through the pneumatic filter (details of this approach will be thoroughly discussed in Section 4.2.1). Additionally, the Gem consists of a printed circuit board (PCB) with various sensors, an SD card slot (for writing data), a thermistor, and an Arduino platform to run the device. A Gem unit can be seen in Figure 13.

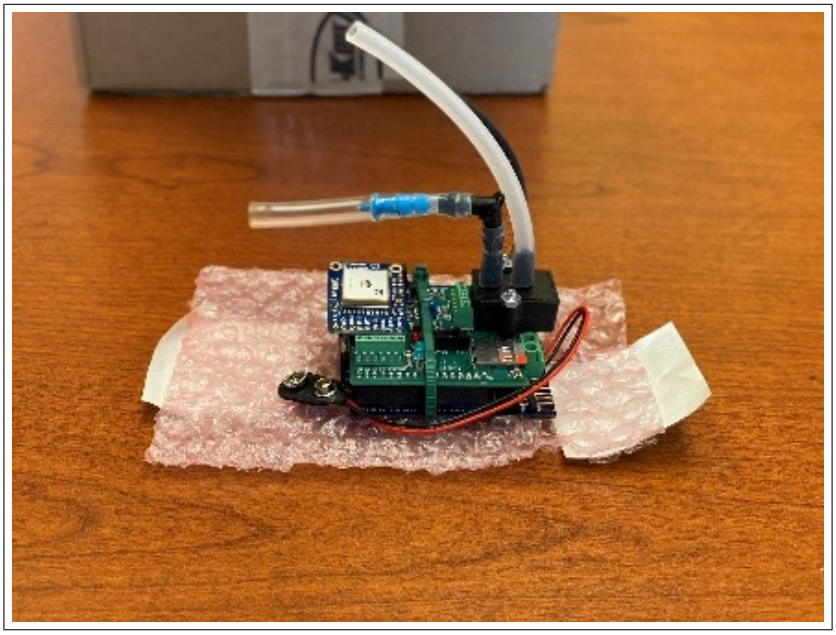

Figure 13: Gem Infrasound Logger.

Other than being an all-in-one infrasound sensor package, the Gem has other strong suits when compared to other infrasound sensing devices. For conciseness, Table 6 is provided and summarizes primary Gem specifications. Note, the reader is encouraged to review literature covering the Gem Infrasound Logger for additional details, as well as how user-configurable parameters will affect the values in Table 6 [36, 21]. The Gem has been utilized in many field campaigns (e.g., [21, 36, 37]) and those who designed the Gem continue to make improve-

ments to the sensor package. However, the Gem design was motivated by field applications that vary from those required by the work in this thesis (applications like those mentioned in Chapter II). Ultimately, the Gem was referenced extensively during the construction and design of another custom sensor package, thoroughly discussed in Chapter IV.

Parameter	**Value**	**Optional Comments**
Sampling Rate (pressure)	100 Hz	Sampled at 400 Hz, FIR-filtered and written to SD card at 100 Hz
Sampling Rate (GPS)	0.001 Hz	20 second sampling burst (at 1 Hz) occurs every 15 minutes
Sensitivity	517 μV/Pa	Adjustable via external resistor
Data Collected	Pressure (V), GPS, state-of-health	State-of-health include battery voltage, temperature, memory usage, processing time.
Resolution (pressure)	0.015 Pa	
Resolution (GPS)	1.8 m	Dependent on amount of satellite-lock signals
Power Draw	186 mW / 95 mW	GPS on/off
Power Supply	2.7-11.8 V	Achieved via USB power, 9V battery, etc.
Weight	78 g	Minimum weight of 1 sensor without power supply
Data Storage Medium	SD Card	Local storage only (i.e., not capable of an internet connection)
Price	> \$1600	Off-the-shelf purchase price for Gem variant used in Bowman et al. [37]
Open Source?	Yes	Hardware designs, firmware, and software

Table 6: Gem primary specifications.

3.2 Auxiliary Equipment

Various equipment was required to complete the experiments presented in later portions of this thesis. The sections below provide details of the supplemental equipment and corresponding specifications.

3.2.1 Infrasound Source

In the experiments presented in Chapter V, an infrasound source was occasionally required to provide a controlled input or reference. Considering infrasound is outside the nominal range of human hearing, devices that purposefully produce infrasound are not of much use

to most consumers; thus, the market of infrasound sources is small. However, some high-end subwoofers can perform in the low-audible and infrasonic regimes. The Arendal 1723-1S [38] is such a subwoofer and was used as an infrasonic source in the work presented. Shown in Figure 14, a signal generator (4040b, BK Precision) was paired with the subwoofer to create a controlled infrasonic tone during experiments. Important specifications of the infrasound source can be seen in Table 7.

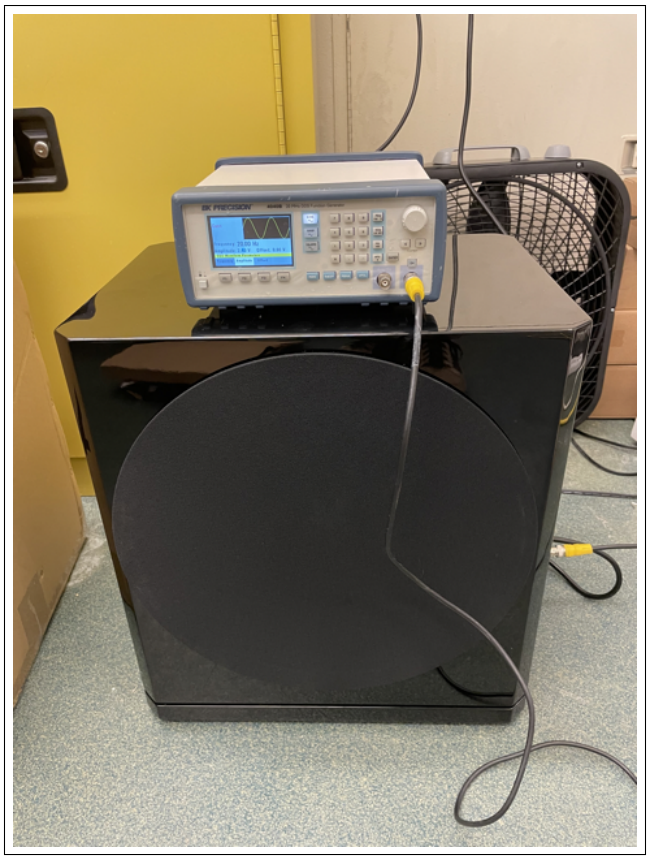

Figure 14: Infrasound source used in experiments (subwoofer and signal generator).

Power	800 W
Full power limit	$\geq$ 10 Hz
Woofer	13.8 in
Enclosure	Sealed
Amplifier	Avalanche 800 IQ
Dimensions	48 x 33.5 x 45 cm
Weight	24.5 kg
100 dB peak, 10 Hz	2m from subwoofer

Table 7: Infrasound source key specifications. Table adapted from Arendal Sound [38].

3.2.2 Shaker Table

Two of the experiments discussed in Chapter V required a shaker table (VT007, Vibration Therapeutic) [39] to evaluate seismic effects on microbarometer measurements in a controlled setting. This shaker table is a linear vibration shaker table typically used for therapeutics and muscle health. However, it's large platform and variable frequency output made it a qualified candidate for the tests performed in this thesis. Figure 15 shows the table as well as the device dimensions, and key specifications of the shaker table are presented in Table 8.

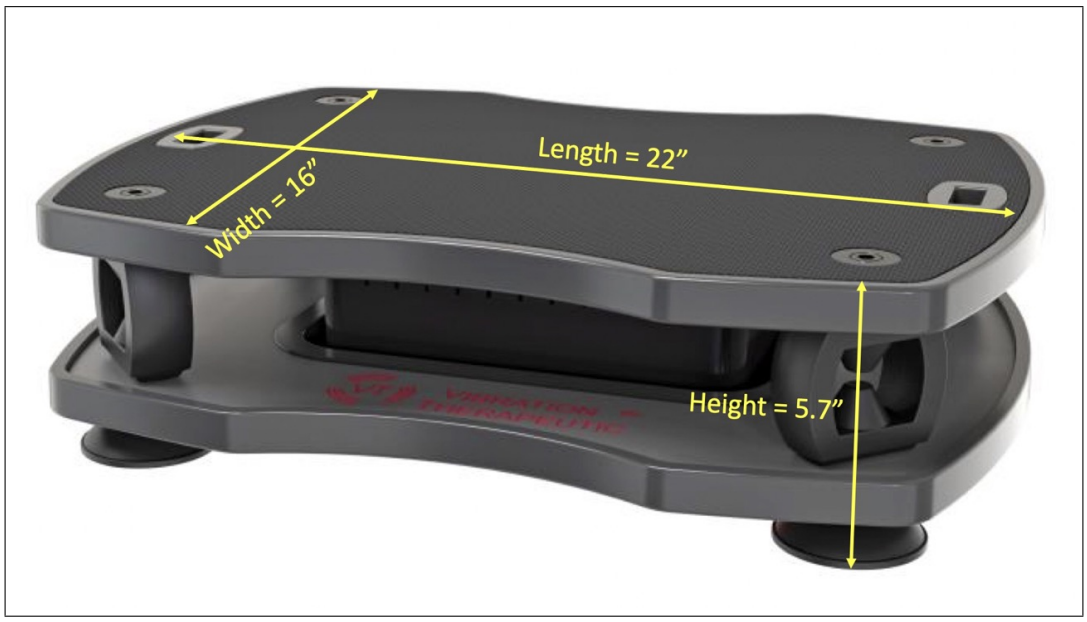

Figure 15: Shaker table with dimensions in inches, used during laboratory vibration experiments.

Vibration Pattern	Linear Vibration
Vibration Frequency	15 - 40 Hz Adjustable, 1 Hz incremental
Amplitude at Hi	1.5 - 3.00 mm without load
Amplitude at Lo	0.7 - 1.2 mm without load
Max G-force	3.8 without load, 3.3 at 180 lb load
Machine Size	560mm x 480mm x 150mm
Machine Net Weight	10.4 kg / 23 lb
Electric Motor	80W PMDC Motor, 900-2400RPM
Power Supply	AC 110V / 60 Hz
Max User Body Weight	140 kg / 308 lb

Table 8: Shaker table specifications. Table adapted from Vibration Therapeutics [39].

Throughout the time the shaker table was used for experiments, a few non-ideal qualities

were observed. First, the acceleration imposed by the table was not limited to the vertical direction (a quality seen in Figure 56). Additionally, some of the results presented in Section 5.1.2 suggest the amplitude of the tables surface displacement varies slightly as a function of the table vibration frequency. However, these non-ideal observations are to be expected with a shaker table in this price range; a high-end shaker table purchase was not appropriate for the scope of this thesis. Ultimately, the following adjustments were made to how experiments were executed, as well as the post-processing techniques used to process data, while using this shaker table:

1. Tests exploring strictly vibration-only impacts (Section 5.1.1) were performed using three different configurations of sensor layout on the table.
2. When applicable, parameters derived from non-vertical accelerations were given for context.
3. Data sets are grouped by respective input vibration frequencies as the table's behavior could not be confirmed as frequency independent.

3.2.3 Unmanned Aerial Vehicle

During the experimental portion of this thesis, a custom-built unmanned aerial vehicle (UAV), termed "SKB-1000", was utilized for a UAV-mounted infrasound measurement investigation. The UAV used was a quadcopter (used 4 propellers for lift) built by various members of the Unmanned Systems Research Institute (USRI) at Oklahoma State [40], and can be seen in Figure 16. Additionally, useful specifications of the UAV are available in Table 9. Note, this UAV is often referred to as the "skateboard" UAV based on the shape of the structure that holds a nominal payload (seen in Figure 57) and might be referred to as such in the source provided.

Figure 16: UAV used in experiments. Figure reproduced from Brenner [41].

Battery	6S 22,000 mah
Motors	320 kV
Propellers	20 in
Flight Time	$\approx$ 20 min
Payload Capacity	6 lb
ESCs	80 A

Table 9: Specifications for the UAV used in experiments. Table adapted from Brenner [41].

3.3 Common Analysis Procedures and Algorithms

This section is, perhaps, the most important section for the reader unfamiliar with spectral analysis. The primary algorithm used for processing data collected during the experimental portion of this thesis is the Welch method [42]; a method that approximates the power spectral density (PSD) of a discrete signal. Section 3.3.1 provides the fundamental equations used to calculate the PSD of a signal, while Section 3.3.2 elaborates on how Welch's method was used in this thesis to approximate the PSD and apply windowing functions to the discrete data collected during experiments. Lastly, Section 3.3.3 provides the reader with a practical example of performing a PSD on a simulated signal and presents the typical methods of visualizing data collected from pressure transducers and IMUs.

3.3.1 Fourier Transform and Power Spectral Density

The power spectral density, or PSD, manifests in domains such as mathematics, signal processing, systems analysis, and many others. It's a useful processing algorithm (or equation) to convert time-domain functions to their frequency-domain components. In signal processing endeavors, the PSD is commonly used to convert discrete time-domain signals from acoustic, vibration, and optical sources, to their frequency-domain counterparts. At its core, computing the PSD of a signal relies on the Fourier transform. A generalized continuous-time form of the Fourier transform is given in equation (3.3.1), where $x(t)$ is the time-domain signal of interest.

$$X(\omega) = \int_{-\infty}^{+\infty} x(t)e^{-j\omega t}dt \qquad \omega \in (-\infty, +\infty) \tag{3.3.1}$$

However, elaboration is required to be able to implement equation (3.3.1) on a discrete-time, finite signal; all experimental data presented in this thesis are such signals. After the Fourier transform in equation (3.3.1) is adapted to a discrete-time, finite signal, the Fourier transform takes the form of equation (3.3.2) which is often referred to as the Discrete Fourier Transform (DFT) where $X[k]$ is the k^{th} component in the frequency domain of the discrete signal of interest, N is the input signal length, and j is the imaginary unit [43]. A common method of executing a DFT in programming languages is to utilize what is known as the fast Fourier transform (FFT) algorithm. Utilizing the DFT in signal processing, via the FFT algorithm, is an exercise that has been extensively covered in literature over the past 60 years [44, 45, 46]; thus, the intricacies of the fast Fourier transform algorithm will not be covered here.

$$X[k] = \sum_{n=0}^{N-1} x[n]e^{-j2\pi kn/N} \qquad k = 0, 1, ..., N-1 \tag{3.3.2}$$

Consider a scenario in which an individual is processing a discrete signal of 100 data points (that is, N=100). In this case, each k^{th} component of the signal's frequency counterpart

will consist of 100 summations utilizing equation (3.3.2). Now, consider an individual is processing the same signal but was able to obtain 1000 samples of the signal (faster sampling rate, longer recording time, etc.). With more samples to sum over, each k^{th} component will have 10x more values to sum over; that is, the amplitude of each frequency component will be higher. Ultimately, the DFT produces frequency-domain amplitudes that are a function of the number of samples in the time-domain signal.

Now, taking the DFT output, $X[k]$, from equation (3.3.2) and computing the power of the frequency domain (via the magnitude squared) and normalizing the result by the length of an arbitrary window, W, produces equation (3.3.3).

$$P_k(v) = \frac{1}{W}|X_k(v)|^2 \tag{3.3.3}$$

Equation (3.3.3) is the basic form of the "periodogram" method, often used as an intermediate step in calculating the PSD of a discrete signal [47]. While more steps are often required to complete the analysis, equation (3.3.3) captures the primary utility of using power spectral density analyses when compared to the FFT. By squaring the magnitude of the FFT and normalizing by a window length, the total energy of an input time-domain signal is accounted for; thus, avoiding the aforementioned frequency-domain amplitude side-effect mentioned in the FFT discussion [48]. Computing the PSD of a signal can be a convoluted process, though, due to the various ways one can approximate[1] the power spectral density [49, 45, 42, 50]. However, one method stands out among others in the data science and engineering communities: the Welch method.

3.3.2 The Welch Method

Modern high-level programming languages used for data analysis (Python, MATLAB, Ruby, Julia, R, etc.) have packages available for engineers, data scientists, and hobbyists to use

[1] **Approximate** is often used to describe a PSD result using finite data, as it would require data of infinite length to calculate the **exact** PSD result [43].

for PSD computations. The most common method of approximating the PSD of a discrete, time-domain signal in these packages is the Welch method. Perhaps the best introductory statement about this method is from Welch himself [42] - "... a method for the application of the fast Fourier transform algorithm to the estimation of power spectra, which involves sectioning the record, taking modified periodograms of these sections, and averaging these modified periodograms". The Welch method approximates the power spectral density of a discrete signal with a few steps. First, the time-domain signal is partitioned into "windows", of which there can be overlap, and the DFT is executed upon each window. Note, there are many different kinds of windowing functions available in the literature [42]; but the "Hann" windowing function is used throughout analyses in this thesis [45, 51]. An example of the effects of a general windowing function is shown in Figure 17.

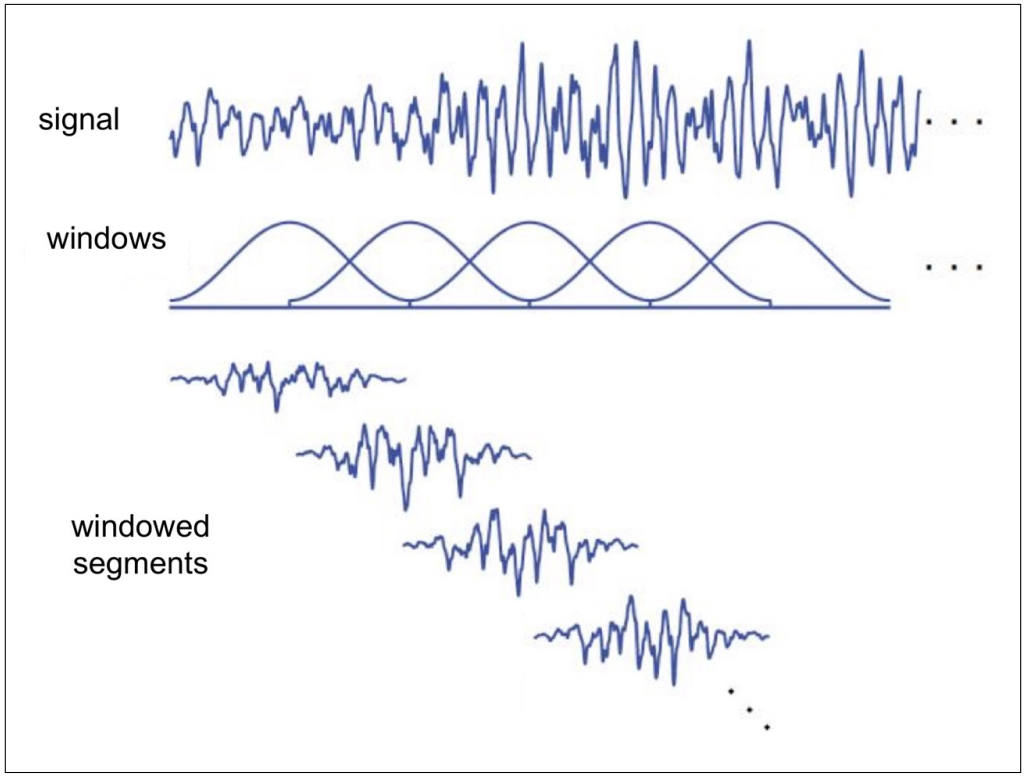

Figure 17: Effect of windowing a signal. Figure adapted from Gutierreze-Osuna [52].

Next, a modified periodogram value for each frequency component is formed for each DFT window using equation (3.3.3) and a windowing function of choice, where W in equation

(3.3.3) is defined in equation (3.3.4) where M is the amount of data points in each window section and $w[m]$ is the windowing function output. Lastly, the periodograms are averaged to approximate the power spectral density frequency components using equation (3.3.5), where K is the total number of windows used to partition the original input signal. The reader is encouraged to read Solomon [53] if additional details are desired, as that study provides a thorough and practical approach to executing the Welch method.

$$W = \sum_{m=0}^{M} w^2[m] \tag{3.3.4}$$

$$S_x(v) = \sum_{k=1}^{K} P_k(v) \tag{3.3.5}$$

Lastly, the reader should note that power spectral density data is often conveyed in decibels (dB), as is the case for applicable plots seen in later sections of this paper. The common convention of converting a PSD output (if executed on pressure data, units are Pa^2/Hz) to log scale is $\Phi_x = 10log_{10}(S_x(v)/P_{ref}^2)$, where P_{ref} is a reference pressure and is squared due to the PSD output from equation (3.3.5) being a squared energy quantity [49, 54]. A P_{ref} value of 20 μPa is used in the analyses presented in this thesis, and the units of Φ_x are dB/Hz.

3.3.3 Common Plots via Simulated Data

The majority of the data throughout this thesis is presented by the power spectral density of a time-domain pressure or acceleration signal. Furthermore, the few exceptions are often data deduced from an existing power spectral density. Thus, an example will help develop intuition for readers who may not have performed these analyses prior to reading the work presented in this paper. First consider the following 4 pressure signals:

1. 8 Hz tone with an amplitude of 0.8 Pa

2. 20 Hz tone with an amplitude of 0.4 Pa

3. 40 Hz tone with an amplitude of 1.5 Pa

4. Random noise ranging between -0.3 and 0.3 Pa.

Each of the signals above, excluding the random noise signal, can be represented with the equation $A_n \sin(f_n 2\pi t)$ where A_n and f_n are a signal amplitude and frequency, respectively, and t is an arbitrary time vector. When each of the 3 signals above are added together, along with the random noise signal, the output is similar to a microbarometer's output signal. Figure 18(top) shows each of these simulated signals, and Figure 18(middle) shows the total signal after summing all four inputs. Following the construction of this simulated

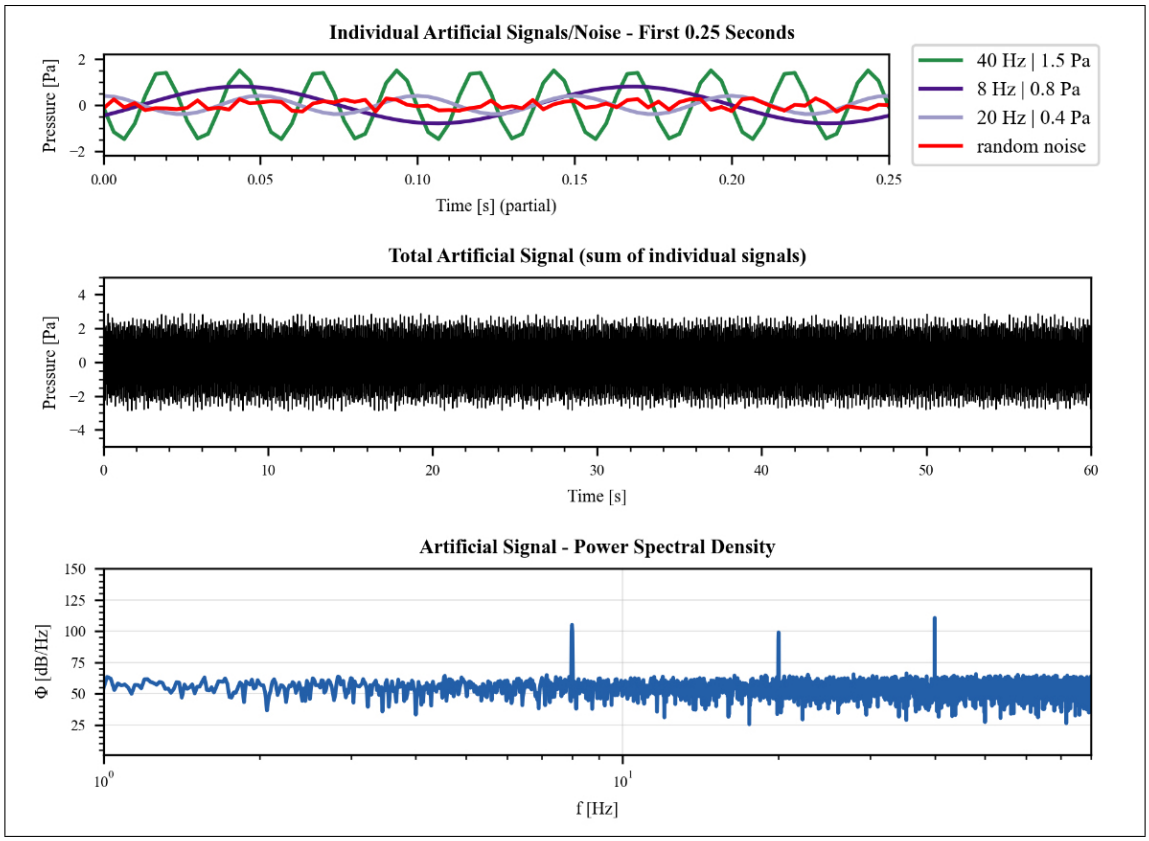

Figure 18: (top) Artificial signals and noise. (middle) Artificial total signal. (bottom) Resulting power spectral density approximation.

signal, the power spectral density was computed and is presented in Figure 18(bottom). It can be seen in this figure that the three signals have tonal "spikes" in the PSD plot, and the random noise present in the simulated signal manifests as a broadband noise floor in this

plot.

Another visualization tool that is used throughout this paper are spectrograms. Spectrograms are very similar to PSD plots except that a transient component is also present. Essentially, a spectrogram utilizes the windows mentioned in the previous section, and displays the individual periodograms throughout the time of the recording. A good way to visualize this is to "deactivate" the simulated signal mentioned previously at an arbitrary time, and plot the spectrogram throughout the entire simulated time vector. Figure 19(top) shows the simulated signal (signals other than noise are deactivated after 30 seconds) and the spectrogram of this signal can be seen in Figure 19(bottom).

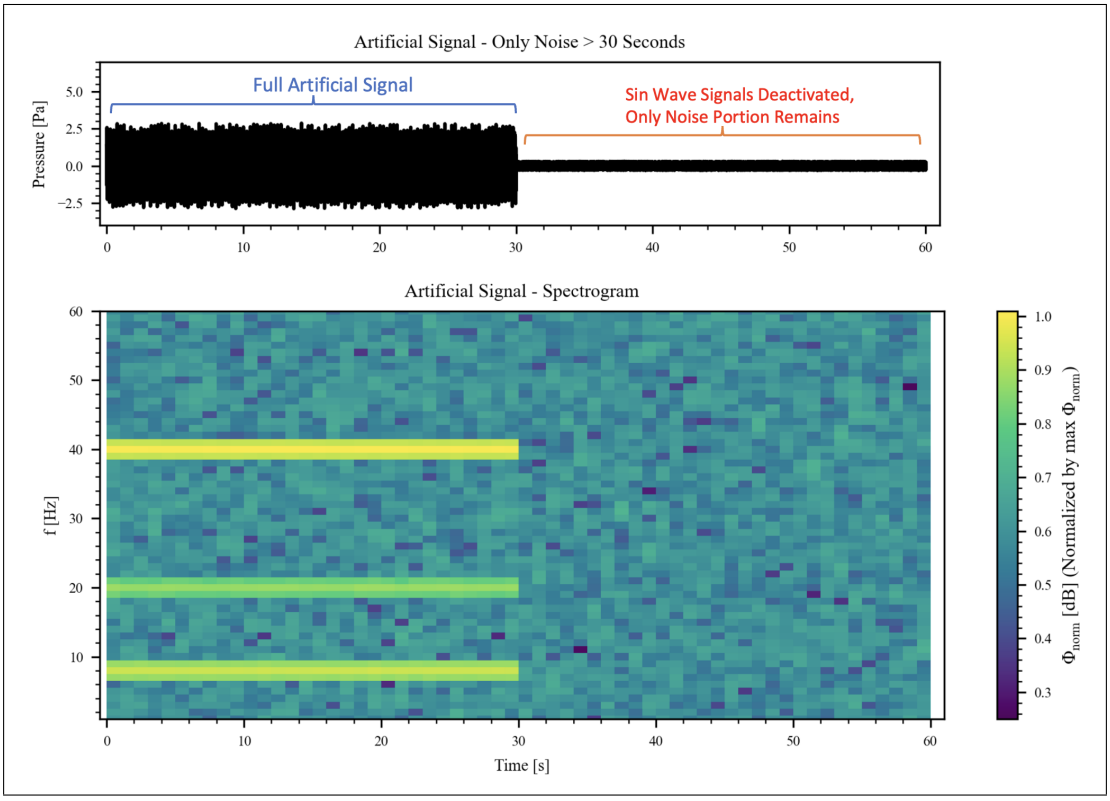

Figure 19: (top) Total artificial signal, deactivated at 30 seconds. (bottom) Spectrogram of total artificial signal.

As a final note (if the reader is interested), the vast majority of PSD and spectrogram visualizations presented in this paper were produced using the Python 3.10 language/interpreter paired with the well-known scientific computation library "SciPy" [55, 56].

CHAPTER IV

THE DESIGN AND CONSTRUCTION OF CLASP

4.1 Overview

Many crucial lessons were learned from the GLINDA2 deployment, and the next iteration of a custom mobile infrasound detection package was ready to take place. Much inspiration was taken from the Gem infrasound logger, as well as the GLINDA2 campaign. This chapter walks the reader through the design and construction of a new infrasound sensor, the **C**loud-capable **L**ow-cost **A**coustic and **S**eismic sensor **P**ackage, or CLASP for short. CLASP was created by the author of this thesis for 2 reasons:

1. To have a low-cost sensor package with similar specifications and capabilities as GLINDA2, while extending its capabilities by reliably recording seismic data via an embedded accelerometer. Moving manufacturing tasks "in-house" (relying on EFPL members to make the components) significantly reduces the price per sensor as well.

2. To construct a customizable platform to be used for controlled vibration experiments. Many of the aspects of the CLASP design could not have been executed on the sensors in Table 4, and the work presented in Chapter V would not have been possible without CLASP's unique configuration and do-it-yourself nature.

CLASP consists of five main components: a differential pressure transducer, primary printed circuit board, GPS module, inertial measurement unit (IMU) breakout board, and a Raspberry Pi 4. First, the differential pressure transducer, paired with a capillary tube on one of the two inlets, converts pressure signal to an analog voltage. Next, the analog signal

from the pressure transducer is conditioned, filtered, and digitized via a custom printed circuit board (PCB). However, two of the five main components have their own breakout circuit boards: the GPS chip and the IMU. The GPS module was isolated from the primary PCB so that the PCB could be covered in foil (to mitigate electromagnetic-related noise) while not inhibiting the GPS's ability to acquire data from satellites. The IMU was isolated from the primary PCB so that it could be mounted directly on the pressure transducer (reasons which will be elaborated on in Chapter V). The last of the five main components is the Raspberry Pi which performs the following tasks:

1. Executes source code to collect data from the primary PCB, GPS module, and accelerometer (on the IMU board).

2. Provides all sensors with an appropriate supply voltage.

3. Stores pressure, acceleration, and GPS data locally or sends the data to a remote server (a decision that is up to the user).

Section 4.2 provides details about CLASP's primary components, software and source code, geometry, specifications, and price per unit. Section 4.3 goes over the procedures required to setup a CLASP unit; primarily, the steps required to configure the Raspberry Pi properly. Section 4.4 compares CLASP data with a Gem Infrasound Logger in both ambient conditions and near an infrasound source for validation. Section 4.5 provides some closing comments about CLASP and its utility among the space of existing infrasound sensors.

4.2 Attributes

4.2.1 Microphone/Capillary Tube

The pressure transducer chosen for CLASP is the 0.5 INCH-D-MV transducer made by All Sensors (All Sensor, Inc. 2011) [57]. The 0.5 INCH-D-MV acquires differential pressure via two inlets, which requires that one side of the diaphragm (one of the two inlets) needs to

have a low-pass pneumatic filter to record acoustic pressure data. This effectively filters out the acoustic pressure waves on one side of the diaphragm, which allows the diaphragm to "see" a net pressure equal to that of the pressure waves while also allowing the diaphragm to adjust for static pressure changes when changing location or altitudes. CLASP's pneumatic filter was constructed using a small capillary tube and a cylindrical backing volume which, if constructed properly, attenuates frequencies above about 0.01 Hz on one side of the pressure transducer's diaphragm. These types of filters have been applied to differential pressure sensors in other disciplines, and a generalized depiction of the filter implemented on CLASP can be seen in Figure 20.

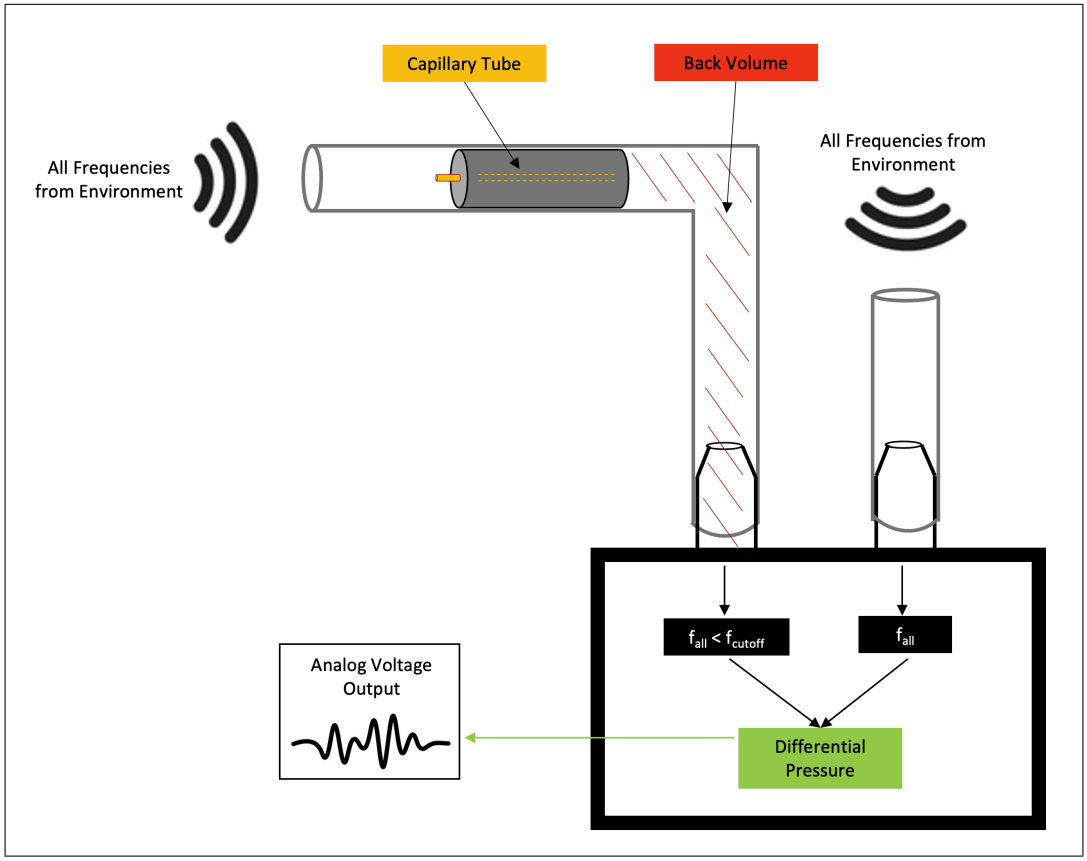

Figure 20: Simplified schematic of CLASP's pressure transducer and capillary tube/back volume.

Pneumatic filters, like the one used in CLASP, can be modeled with electrical analogies; along with most components in common acoustic pressure sensors [58]. For example, the capillary tube used in a CLASP unit has a very small diameter-to-length ratio, and its

acoustic resistance (R) is defined by equation (4.2.1), below, where η is shear viscosity, and both the length (l) and radius (r) define the geometry of the capillary tube [59].

$$R = \frac{8\eta}{\pi r^4} l \tag{4.2.1}$$

Another useful acoustic parameter used in modelling the pneumatic filter is capacitance. Using, again, electrical counterparts (electronic capacitor), the acoustic capacitance of the accompanying back-volume is defined by equation (4.2.2), where ρ is air density, c is the local speed of sound, and V is the back volume [58].

$$C = \frac{V}{\rho c^2} \tag{4.2.2}$$

Lastly, the resistance and capacitance models are used in series to create a simplified representation of the low-pass pneumatic filter used in the CLASP system. This relationship is described by equation (4.2.3), and was utilized to size CLASP's back volume and capillary tube to target a cutoff frequency of about 0.01 Hz[1]. A few assumptions have to be made to apply this simplified model (isothermal, lumped model) but recent work has shown that this simplified model is sufficient for pneumatic filters with cutoff frequencies below 1 Hz [60], such as the capillary tube assembly made for CLASP.

$$f_{cutoff} = \frac{1}{2\pi RC} = \frac{\rho c^2}{16\eta} \frac{r^4}{Vl} \tag{4.2.3}$$

4.2.2 PCB

Beyond a reliable response to pressure fluctuations, a well-designed microbarometer also requires proper signal conditioning, filtering, and digitization. Additionally, the sensitivity of the 0.5 INCH-D-MV pressure transducer is a function of the voltage supplied to the sensor.

[1]Cutoff frequency will vary +/- .01 Hz depending inlet tube placement on its nipple, preciseness of capillary tube cutting, etc.

Thus, a stable voltage is needed to properly utilize the pressure transducer. Ultimately, a custom PCB design was required to incorporate the 0.5 INCH-D-MV pressure transducer into the CLASP system. However, the individuals who developed the Gem Infrasound Logger designed the Gem's PCB for similar conditions, when compared to CLASP. Thus, their work was referenced many times throughout the design of the CLASP PCB. Using the Gem's PCB as a framework significantly expedited the time taken to design CLASP's PCB, and the nuances between each system's PCB is primarily due to different deployment methods and optimization for those methods.

A detailed layout of CLASP's custom PCB can be seen in Figure 21. The critical components of the board are numbered on this figure, and each are summarized in the list below. Additionally, the complete schematic of the board is presented in Figure 58, found in the appendix.

1. Pressure transducer breakout: accepts the pins of the 0.5 INCH-D-MV pressure transducer [57]. This breakout supplies the transducer with power and provides a connection for the analog-out signal pins on the transducer to integrate into the board.

2. INA118UB Instrument Amplifier [61]: Applies a user-specified gain (utilizing an external resistor on the board) to the analog signal received from the pressure transducer.

3. AD8538 Operational Amplifier [62]: Provides a low-impedance reference voltage to the INA118UB amplifier. The voltage provided by this op-amp is critical to ensure a constant pressure/voltage sensitivity is achieved throughout recording.

4. ADS1115 Analog-to-Digital Converter [63]: Converts the analog signal from the pressure transducer to a digital signal for the computer to process. A programmable gain of 16 is applied within the ADC (which can be changed in the source code) to optimize dynamic range.

5. Voltage regulator: Mitigates adverse effects of voltage slumps/spikes from the 3V pin on the Raspberry Pi [64].

6. GPIO Pin breakout: Aligns with the pins on the Raspberry Pi to create a connection between the computer and the PCB.

7. GPS Breakout: accepts the pins of the Adafruit Ultimate GPS Breakout [65] which provides GPS data (location, speed, GPS time) to the computer.

8. RC filter: low-pass filter (<372 Hz) that helps eliminate high frequency electrical noise.

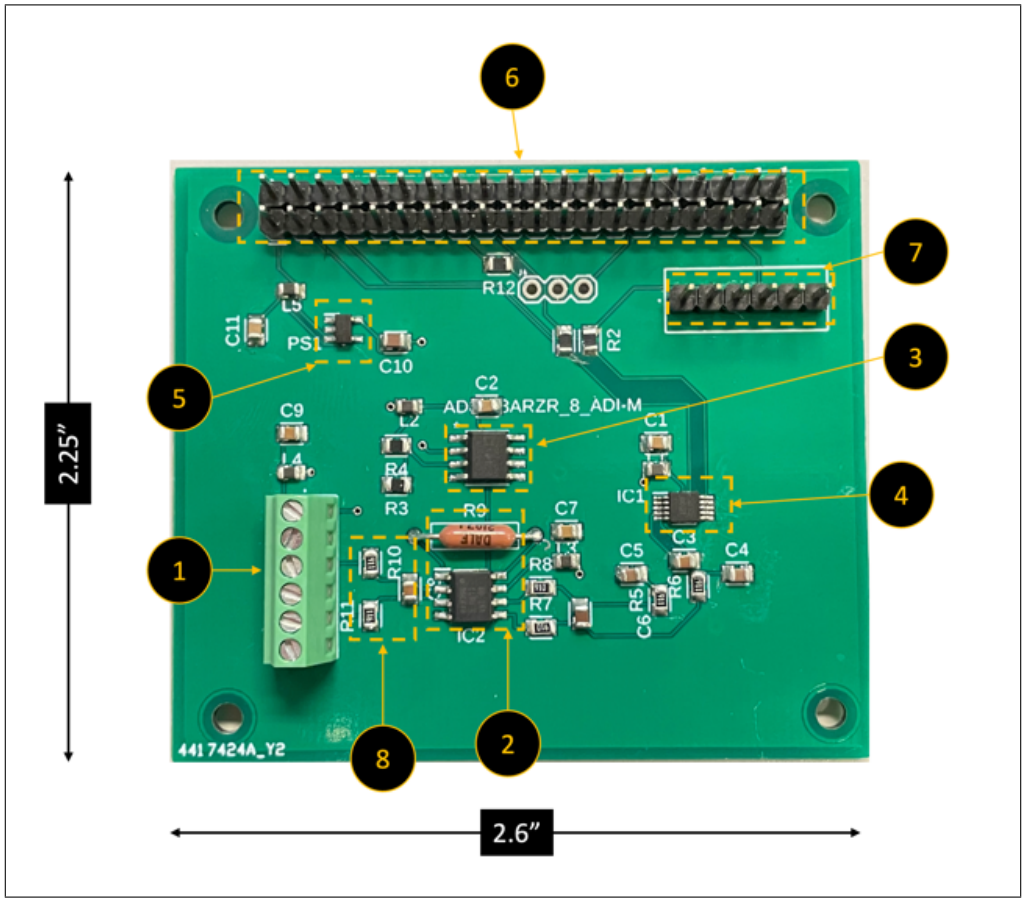

Figure 21: Signal conditioning, filtering, and digitization PCB created for CLASP.

4.2.3 Computational Details and Software

GLINDA2 remained in the field for much longer than GLINDA1, and a large part of that success is due to the software changes made after experiencing the challenges of deploying GLINDA1. CLASP further builds on the momentum of GLINDA2 and implements its source-code in similar ways. The subsections below provide details of the custom software, autonomous programs, and remote data storage options implemented on CLASP.

Git Operations

Before 2021, in-line identity verification during Git operations were acceptable to use. Recently, security risks have made that method unsafe and repositories, like GitHub, are slowly deprecating this option. Thus, CLASP utilizes SSH keys to verify identity. SSH keys are more secure due to password information not existing in the source code. Additionally, SSH key verification is more robust and will likely not see deprecation for several years. Furthermore, the SSH key verification method also allows for use of "deploy keys" within the GitHub server. Deploy keys serve as a highly optimized solution for source code distribution and control across several systems - i.e., several CLASP units deployed in the field.

Systemd Services

There are several options to choose from when deciding how to execute code on a Raspberry Pi autonomously. A very common method, and the method used during the GLINDA1 campaign, is executing code via the Linux system administrator script "rc.local". However, this method is outdated and can cause stability issues due to administrator permissions. With only one unit in the field (the case for GLINDA1), accessing/executing administrator-level processes is possible. But, ideally, many CLASP units would be deployed at once in large arrays or among several storm-chasers. Thus, modifications have been made so that CLASP does not rely on administrator-level processes. All automated programs on CLASP are initiated using the "Systemd" software suite (a standard suite in most Linux distributions). A thorough discussion of the differences between the "Systemd" approach and "rc.local" approach is not critical for this thesis, but it is worth noting the "Systemd" approach is considered more involved and convoluted than the "rc.local" approach. The added work on the front end was accompanied by more stability and customization in the long run, though; which is very important if multiple CLASP units are deployed simultaneously. Figure 22 shows all Systemd service files running on CLASP, with the two custom services isolated by arrows. The contents of both custom services can be seen in the appendix.

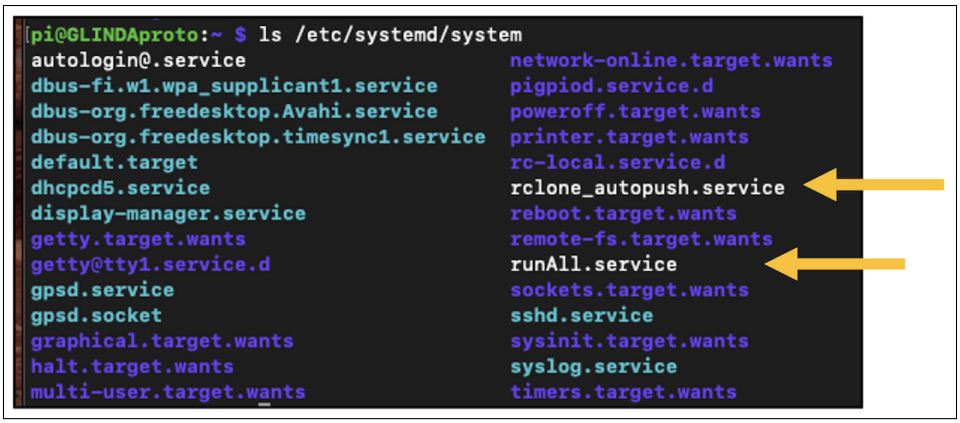

Figure 22: Primary Systemd service files executed when CLASP boots up.

Data Storage: rclone

GLINDA2 has been pushing raw data to a remote server for more than a year, and this method was also implemented on CLASP. Instead of pushing raw data to GitHub via Git operations, like GLINDA1, CLASP uses a command-line program called "rclone" for cloud storage. This method can interface with most cloud-based storage options (Google Drive, OneDrive, DropBox, etc.) and eliminates the administrator-level issues experienced while using GitHub for data storage across multiple automated devices. Additionally, using cloud-based storage allows those who adopt this project to extend this protocol to Internet-of-Things (IoT) operations. IoT operations are commonly used for real-time interfaces and autonomous data processing, which if implemented on CLASP, would be a powerful tool.

Source Code Overview

Figure 23 is provided to summarize the programs and boot operations performed by CLASP, and the generalized list below provides additional context. All operations listed below, as well as those on the flowchart, have been simplified for this report, but the high-level perspective provided here should give insight on the "brains" of CLASP. An additional aspect to note is all programs used to automate CLASP are organized via hostname-referenced directories; thus, each CLASP unit operates independently based on unique hostnames.

- runAll.service - Systemd service initialized on boot (after critical system operations have completed)

and attempts to wait for a target network. If a connection to the target network is achieved, a "Git Pull" script is performed and is followed by the "runAll_g2.py" script. If a connection is not established, the service executes "runAll_g2.py".

- rclone_autopush.service - Systemd service initialized on boot (after critical system operations have completed) and requires a target network. Attempts to initiate the rclone data-pushing process. The service will continue to restart upon failure. If succeeded, the "rclone_autopush.py" script continuously loops until the system shuts down.

- autopull.py - Python script that pulls source code updates from CLASP remote GitHub server: `https://github.com/brylind/clasp_src`.

- runAll_g2.py - Python script that utilizes the "multiprocessing" module to establish multiple processes (simultaneously starts the runMIC.py, runACC.py, and runGPS.py scripts)

- rclone_autopush.py - Python script that utilizes rclone to move pressure, acceleration, and GPS data to a remote server (Google Drive). Minimum-age filters are applied during this continuously-looping script to provide a small buffer between data being written and data being pushed to the cloud.

4.2.4 Price

By substituting a simple pressure transducer and custom PCB in place of the Chaparral 24, CLASP has a drastically lowered price per unit than both GLINDA units (as well as the options in Table 4). Prices are a function of several parameters (bulk orders, existing components in the lab, etc.), but the first CLASP prototype was made for under $350. This corresponds to a, roughly, 90% decrease in costs compared to GLINDA1 and a 80% decrease compared to GLINDA2. Furthermore, the CLASP price per unit will likely further decrease as system reliability matures and bulk orders become a regular occurrence. Ultimately, this cost decrease could result in more CLASP units in the field.

4.2.5 Dimensions and Internal Layout

The components of CLASP aren't constrained by a particular internal layout. The CLASP unit constructed for this thesis fits inside of a 6"x6"x3.5" box with a considerable amount of

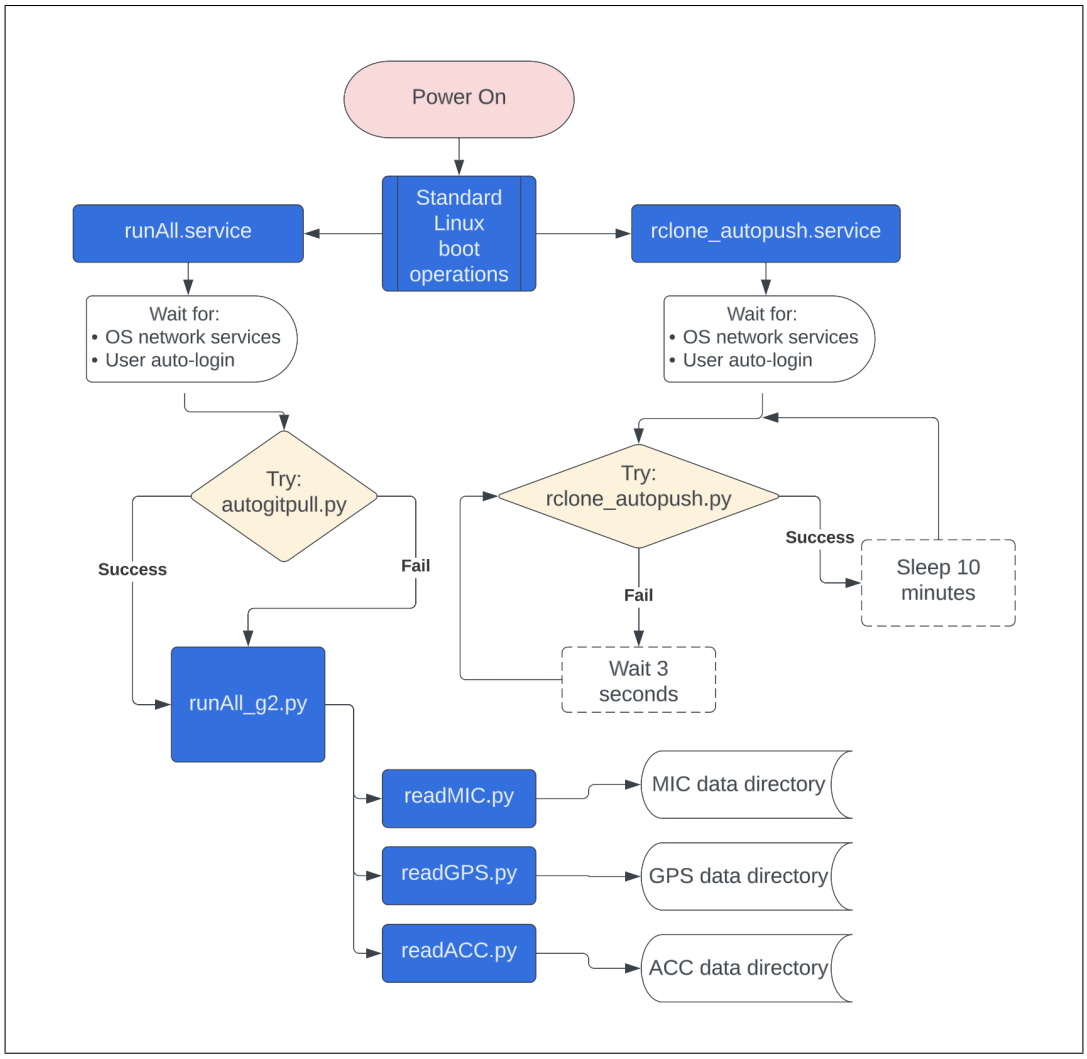

Figure 23: Generalized CLASP data/software flowchart.

foam and foil, but a reduction of footprint is possible if a researcher requires it. The internal configuration of the primary CLASP unit used for this thesis can be seen in Figure 24a, and the dimensions of the unit with the enclosure sealed can be seen in Figure 24b. One can see a few unique decisions made in these figures. First of all, the pressure transducer has been rotated so the diaphragm is orthogonal to the surface that the box sits on (i.e., orthogonal to the gravity vector, $\hat{g}$, unless specified otherwise in this thesis). Additionally, as previously mentioned in this section, the IMU has been placed directly on the pressure transducer body. The IMU could have been embedded in the primary PCB, but this could have provided false signals due to board dynamics; having the IMU on the pressure transducer ensures the

acceleration signals recorded are those experienced by the diaphragm.

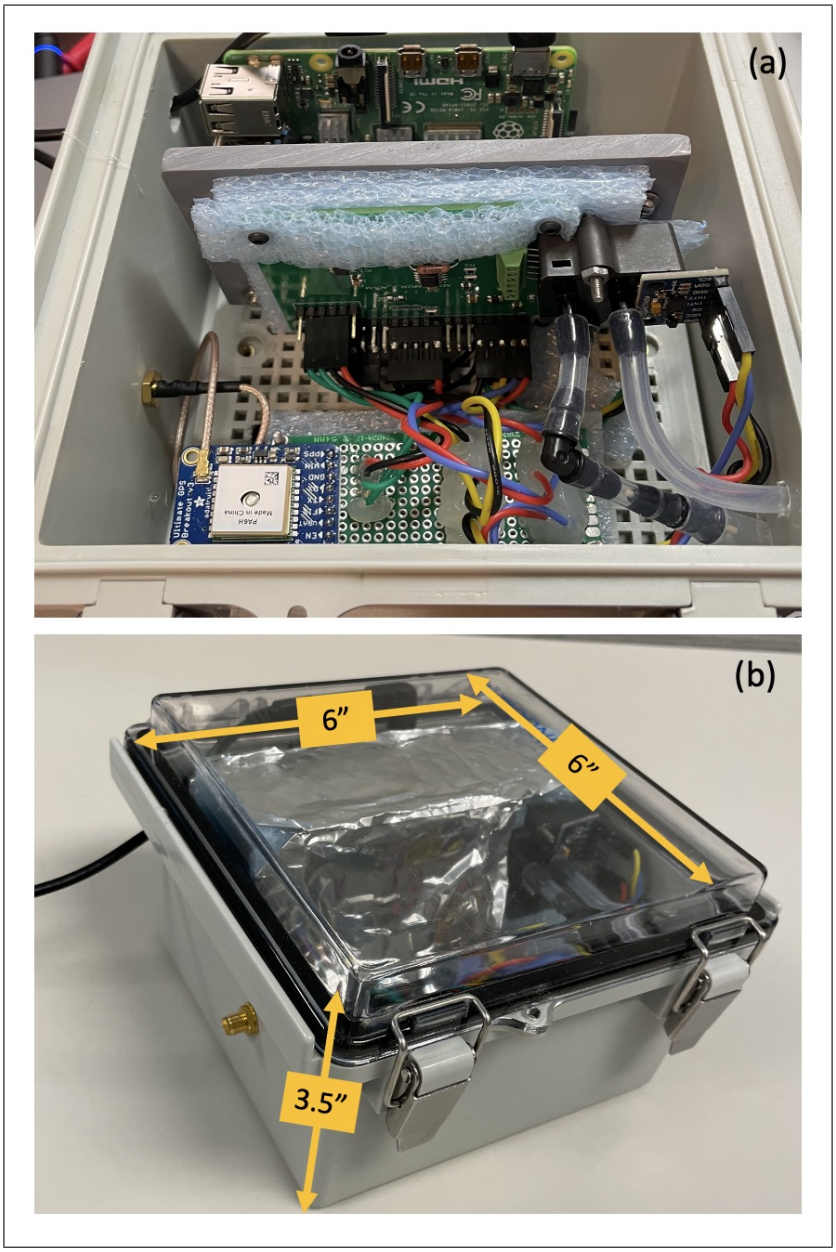

Figure 24: (a) Current CLASP unit internal layout. (b) Dimensions of current CLASP unit.

4.2.6 CLASP Specifications

The primary specifications of CLASP can be broken into 4 categories: system, pressure transducer, GPS, and IMU. Table 10 provides a summary of these specifications, but the

reader should note that many of these parameters are user-configurable. For example, sampling rates can be changed in the source code. Additionally, the total gain can be adjusted in the source code and/or external resistor. Furthermore, the weight of the sensor package could be reduced. However, Table 10 represents CLASP in how it was used throughout all applicable portions of this thesis.

Parameter	**Value**	**Optional Comments**
System Specifications		
Data Collected	Pressure (V), GPS, microphone acceleration (x,y,z), network status	network status is a yes/no if connection to the remote repository exists
Power Draw	2.2 W	Nominal
Power Supply	5V, 9V, 15V, 20V	Achieved via USB-C input on Raspberry Pi 4
Weight	669 g	1 sensor package in case, without power supply
Data Storage Medium	SD Card or cloud-based storage	Via rclone it supports OneDrive, Google Drive, Amazon Drive, Dropbox, and many others. See Craig-Wood [66]
Price	$\approx$ \$450	Price/unit as of 1 Jan 2023 if self assembled (heavily dependent on supply of components for PCB)
Open Source?	Yes	Hardware designs, firmware, and software
Pressure Specifications		
Sampling Rate	250 Hz	No real-time FIR filter. Left for post-processing
Sensitivity	2.371 mV/Pa	Total sensitivity (pre-gain sensitivity is 22μV/Pa)
Resolution	0.0078 Pa	With ADC Programmable Gain Amplifier set to 16
GPS Specifications		
Sampling Rate	0.1 Hz	Requests location, speed, GPS time, fix (yes/no), and number of satellites fixed
Resolution	>1.8 m	Dependent on amount of satellite-lock signals
IMU Specifications		
Sampling Rate	400 Hz	Maximum capable sampling rate is dependent on user-configurable parameters
Resolution	$0.0383 \frac{m}{s^2}$	With 13-bit dynamic range and $\pm$8g limiting range

Table 10: CLASP primary specifications.

4.3 System Setup Procedures

One of the primary challenges during the design and implementation of CLASP (as well as GLINDA 2) was the setup procedures required to successfully execute software packages. Sensors that utilize proprietary software/firmware often have a streamlined setup procedure. However, executing custom source code on open-source operating systems presents specific challenges due to limited or imprecise documentation. Thus, this section aims to provide insight on setting up a sensor package like CLASP.

While CLASP is focused on collecting seismic, acoustic, and GPS data, the setup procedures can be applied to any sensor package that uses a Single Board Computer (SBC), has GPIO pins, and is capable of running a Linux-distribution operating system (OS). However, CLASP relies on cloud-storage capabilities[2] and high i^2c speeds, so a Raspberry Pi 4 running on the default operating system, Raspberry Pi OS (previously called Raspian), is recommended if the one would like to build a package of similar nature to CLASP. Additionally, CLASP uses a GitHub repository for remote source-code modifications and control. Other options for source-code control include GitLab, Bitbucket, and SourceForge, among many others. If a researcher does not find a need for this functionality (i.e., wants to make changes to source code locally), some of the CLASP setup procedures are not necessary.

Lastly, a monitor is not required to set up CLASP (or a sensor package similar to it) as CLASP was fully configured as a "headless" unit. Using an SSH connection, one can fully configure SBC-based or microcontroller-based sensor packages with an affordable laptop or separate SBC. Ultimately, the steps required to set up CLASP are best delivered in chronological order. Thus, Table 11 provides all crucial steps used to implement CLASP's acquisition and cloud-storage software properly.

[2]If cloud-storage is desired, it is recommended to use Raspberry Pi with on-board WiFi; otherwise, adapters are required.

#	**Action Required**	**Comments**
1	Setup Raspberry Pi - install operating system, establish unique hostname and password, etc.	CLASP utilizes the default Raspian OS
2	Make Source-code GitHub Repository	Only required if remote source-code control is desired
3	Setup GitHub deploy key	SSH keys work as well, deploy keys preferred
4	Dowload/pull source-code and packages to Raspberry Pi	CLASP source-code and package requirements available in Lindsey, 2021 [67], packages also seen in Table 16
5	Activate i^2c interface	Achieved through the raspi-config tool
6	Increase i^2c to 400 kB/s	Achieved by editing /boot/config.txt, example in appendix
7	Disable on-board Bluetooth	Required to prioritize GPS UART connection, achieved by editing /boot/config.txt, example in appendix
8	Disable serial login	Achieved through raspi-config tool
9	Enable serial port	Achieved through raspi-config tool
10	Add user to tty and dialout groups	Achieved with the "usermod" command, example in appendix
11	Make service files	Place services in /etc/systemd/system directory, examples in appendix
12	Activate service files	Achieved with "systemctl" command, example in appendix
13	Reload systemd	Achieved with "systemctl" command, example in appendix
14	Establish wifi network and password	Achieved through editing etc/wpa_supplicant/wpa_supplicant.conf
15	Set up rclone	Instructions seen in Craig-Wood, 2014 [66]

Table 11: Setup procedures for CLASP and similar sensor packages.

4.4 Validation

This section provides validation of CLASP's acoustic capabilities via two tests: an 80-minute ambient recording outdoors, covered in section 4.4.1, and a 2-minute recording of an infrasound source (forced door oscillation), covered in 4.4.2. Visual comparisons of the power spectral densities of each validation case will be discussed, as well as the calculated variance of each data set via the spectral integration method [68], given in equation 4.4.1.

$$\sigma_x^2\Big|_{f_1}^{f_2} = \sum_{k=f_1}^{f_2} \Phi_x(k)\Delta k \tag{4.4.1}$$

4.4.1 Ambient Input Validation

To validate CLASP's acoustic response to ambient noise, a CLASP unit was left outside for about 80 minutes with a Gem unit placed next to CLASP. The environment surrounding both sensors consisted of sound sources like wind, moving cars, and the general rumble of a residential area. The PSD of each sensor's acoustic data collected during this period can be seen in Figure 25, and these results show much agreement upon inspection. Note, the Gem applies an additional low-pass filter (<40 Hz) to raw data before its written to an SD card, which is why the two sensors begin to diverge above 20 Hz (CLASP leaves the task of additional filtering up to the user in post-processing). The approximate self-noise floor of CLASP (acquired during the work presented in Section 5.1.1) is included as a gray line in the figure for reference.

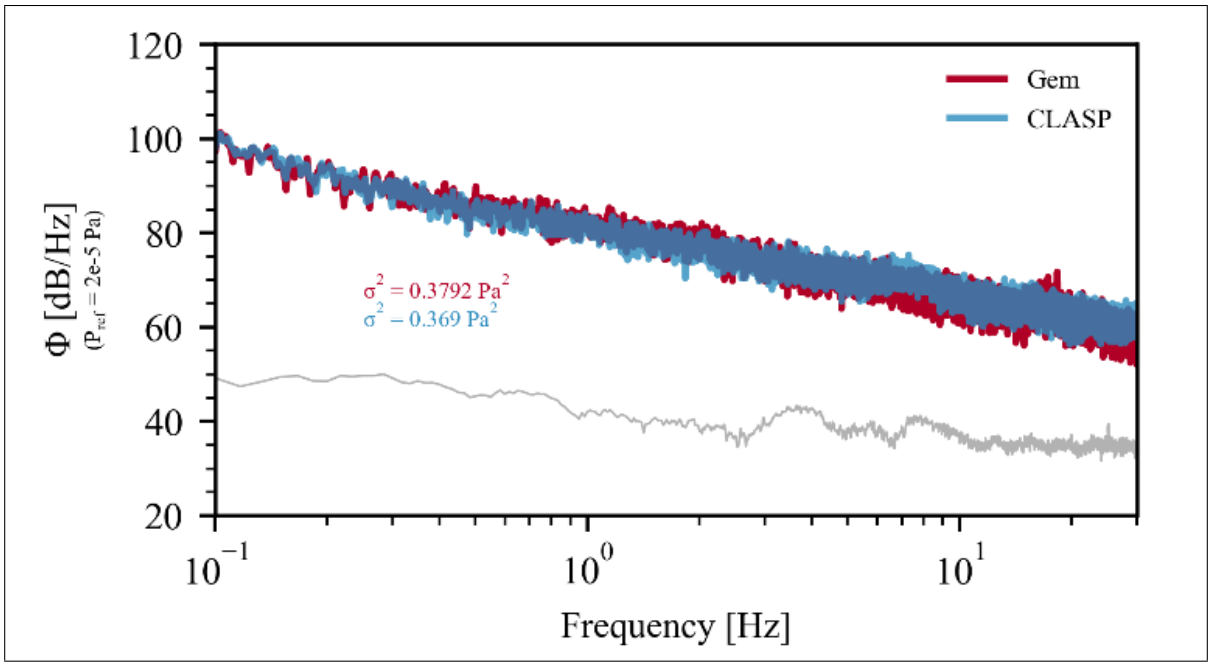

Figure 25: Ambient data of Gem Infrasound Logger and CLASP. Total recording time = 78 minutes. Windowing parameters = 'Hann', 600 seconds, 50% overlap. Gray line: approximate CLASP self-noise floor.

Using equation 4.4.1 to quantitatively compare the spectral content of both sensors, and using a frequency band of 0.1 Hz to 10 Hz (i.e., $[\,]\big|_{fb} = [\,]\big|_{0.1Hz}^{10Hz}$), gives the following variance discrepancy:

$$\sigma^2_{Gem}\Big|_{fb} - \sigma^2_{CLASP}\Big|_{fb} = 0.379Pa^2 - 0.369Pa^2 = 0.01Pa^2$$

The resulting percent difference of variance in this case is 2.67% difference. Ultimately, the ambient data from both CLASP and the Gem Infrasound Logger are quantitatively and qualitatively extremely similar; furthering the confidence in CLASP's abilities.

4.4.2 Source Input Validation

To validate CLASP's acoustic response to a low-infrasound source, CLASP and Gem units were left in a small room while the door was oscillated at a target frequency of about 3 Hz. This method of producing infrasound may seem informal, but is indeed a reliable way to produce an infrasound signal. The PSD of each sensor's acoustic data collected from this test can be seen in Figure 26, which show a similar degree of agreement as the ambient validation

test. The approximate self-noise floor of CLASP (acquired during the work presented in Section 5.1.1) is included as a gray line in the figure for reference.

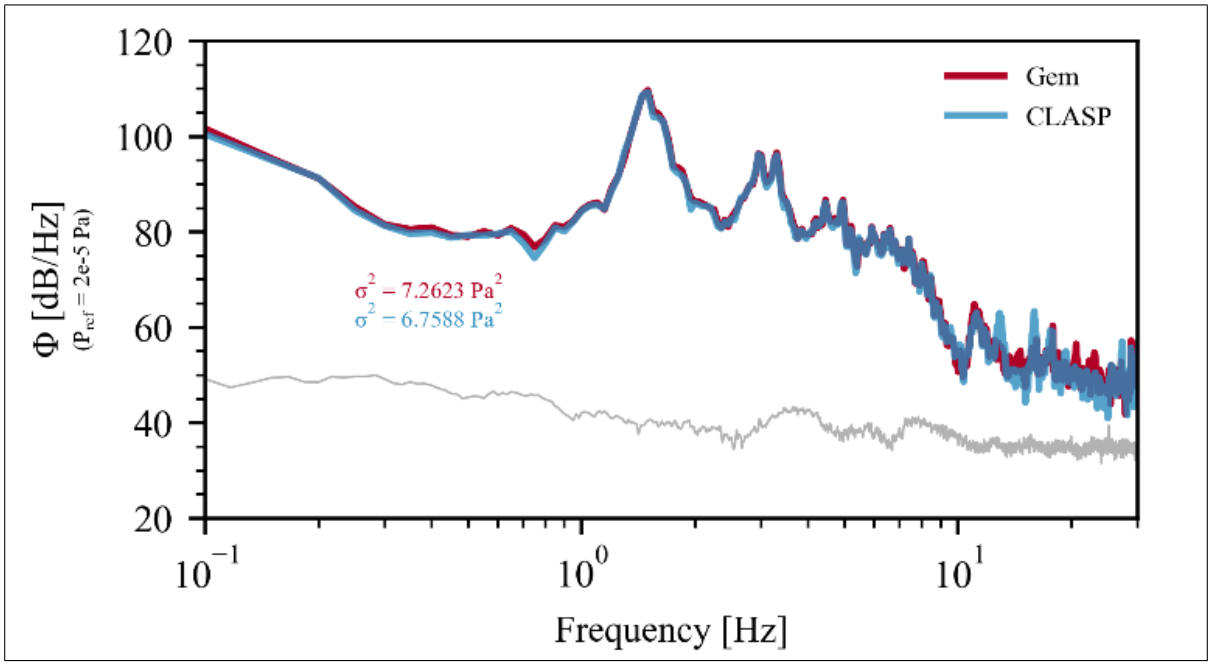

Figure 26: Infrasound source input data of Gem Infrasound Logger and CLASP. Total recording time = 2 minutes. Windowing parameters = 'Hann', 20 seconds, 50% overlap. Gray line: approximate CLASP self-noise floor.

Using equation 4.4.1 in the same manner as Section 4.4.1, over the same frequency range of 0.1 Hz to 10 Hz, gives the following change in variance during the infrasound source validation test:

$$\sigma^2_{Gem}\Big|_{fb} - \sigma^2_{CLASP}\Big|_{fb} = 7.264Pa^2 - 6.760Pa^2 = 0.504Pa^2$$

The resulting variance difference of 0.504 Pa^2 corresponds to a 7.13% difference. The slightly higher $\Delta\sigma^2$ for this test is likely due to pressure wave reflections in the environment and the short duration of the test. However, both validation cases resulted in an acceptable $\Delta\sigma^2$ for the purposes of this thesis. Ultimately, the validation tests shown in this section provide sufficient confidence in the data collected from CLASP throughout the experiments presented in this thesis.

4.5 Closing Comments on CLASP

To conclude this chapter, it's worth noting the impact of CLASP. In the relatively scarce market of infrasound sensing devices, CLASP presents several advantages over the options in Table 3; such as beginner-friendly source code languages (Python, bash), price, being an all-in-one seismo-acoustic package, and offering a cloud-storage framework that is user-configurable for various cloud-based storage options. Additionally, the cloud-storage framework utilized by CLASP has proven to be robust throughout a year-long deployment of other packages that use the same framework. Furthermore, while CLASP was designed and constructed for the purposes of investigating the effects of mobile platforms on infrasound measurements, its usefulness to the scientific community is not limited to the experimental endeavors in this thesis. Similar to the Gem, CLASP serves as a valuable resource for those in the space of infrasound acquisition and analysis, as the publishing of its geometry, source code, and hardware (CAD/GERBER files) may encourage other researchers to create their own derivatives of CLASP to better suit their mission.

CHAPTER V

VIBRATION EXPERIMENTS

This chapter summarizes the experiments performed to investigate the effects of vibrations on sensor packages like CLASP, as well as determines if the CLASP design mitigates any of these effects. Due to lack of prior work in this particular area of research and processing data from the GLINDA deployments, it is suspected that multiple factors are at play between vibration input and microbarometer response. Thus, both lab-based and field-based experiments were constructed to provide intermediate conclusions about the driving factors behind the coupling between vibrations and the output pressure signal from a microbarometer. Additionally, the experiments aim to determine whether or not data collected from CLASP-like sensors in seismic environments should be supplemented by additional data to be considered valid. The following four experiments were performed:

1. Shaker table testing with closed acoustic inlets (sensors are acoustically isolated via ball valve)
2. Shaker table testing with open acoustic inlets
3. Data acquisition inside a vehicle driving on various road conditions and at various speeds
4. Flight on-board a UAV with infrasound source nearby

The acoustically isolated and nominal configuration shaker table tests, seen in Section 5.1, were performed to reduce the size of the parameter space that dictates the relationship between vibrations and microbarometer signals (briefly mentioned in Section 2.2). The vehicle-based experiments, seen in Section 5.2, directly compared the GLINDA2 and CLASP configurations in the environment with the most background data available (both GLINDA

systems' field deployments), while providing the additional asset of IMU data to characterize the vibrations present in this environment. Lastly, the UAV-based experiment, seen in Section 5.3, helps to provide a data set and insight to the challenges of performing infrasound measurements on-board a UAV; an ability that has been of interest to the research community for several years (e.g., [69]).

5.1 Shaker Table Experiments

Throughout both the acoustically-isolated and open-inlet vibration tests, the shaker table seen in Section 3.2.2 was used and certain parameters were held constant. The amplitude (displacement) setting on the shaker table did not change and was held at the "low" setting which, according to the table specifications, is $\approx$ 1.2mm. Additionally, while the inlet tube configuration changed from one experiment to the other, the internal layout of GLINDA2 and CLASP units did not change. The internal layouts of each sensor used during experiments can be seen in Figure 27.

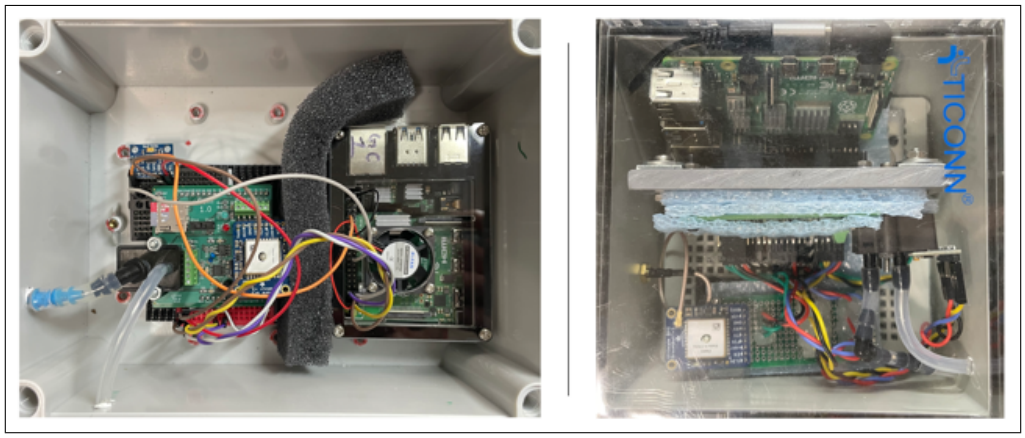

Figure 27: GLINDA2 unit (left) and CLASP unit (right) used during shaker table testing.

5.1.1 Closed Acoustic Inlets

Three different configurations of sensor layouts were used during the acoustically-isolated shaker table test. This ensures any non-uniform acceleration effects across the table could

be seen in the data, as well as further characterized the effects of changing the orientation CLASP. Figure 28 shows a top view schematic of the three configurations used throughout the tests, as well as the mic-normal (normal with respect to pressure transducers) directions of both sensors relative to the shaker table's surface-normal direction. Gravity was acting in the $-z$ direction according to this schematic. For clarity, an annotated image of the experi-

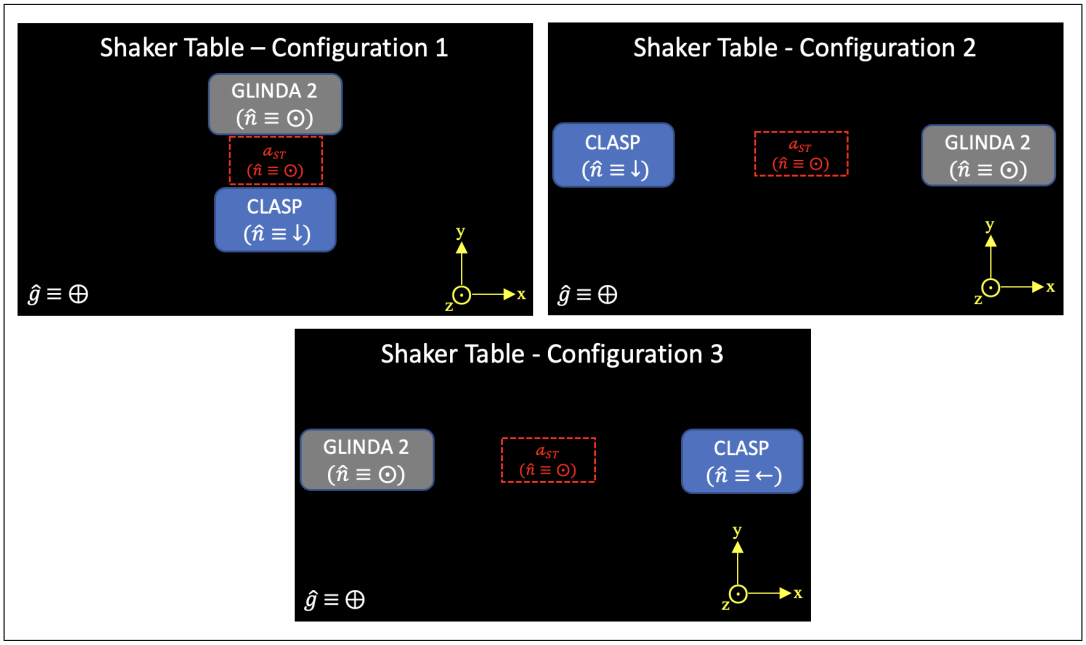

Figure 28: Top-view schematic of closed acoustic inlets shaker table test.

mental setup during configuration "3" can be seen in Figure 29. Images of the remaining 2 configurations are included in the appendix.

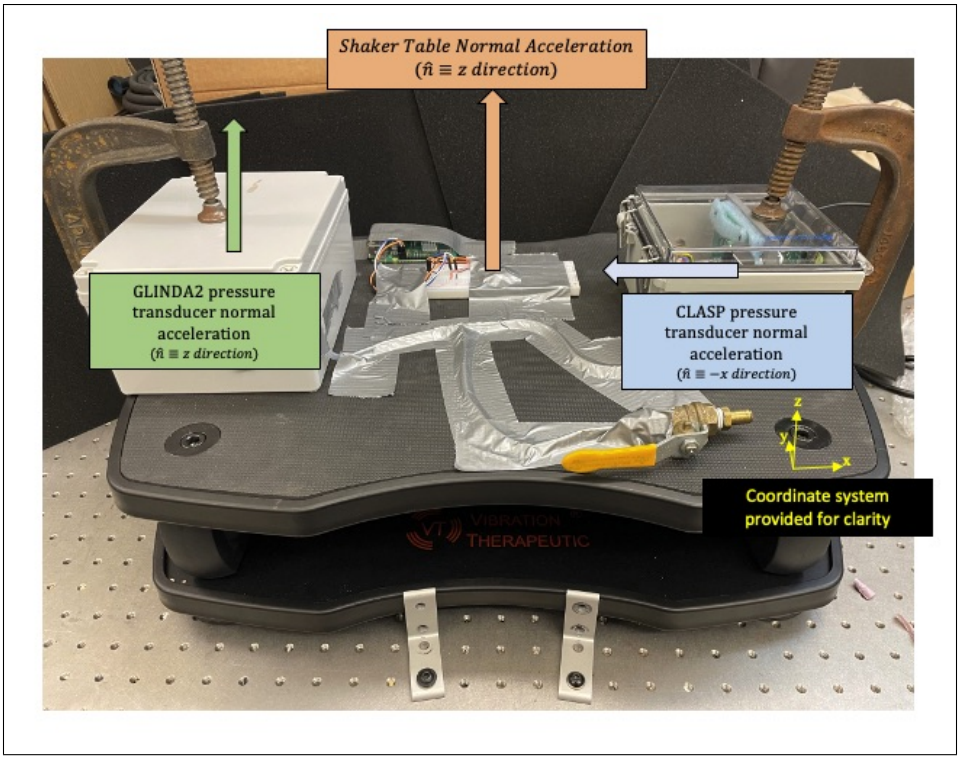

Figure 29: Configuration 3 of closed acoustic inlets shaker table test.

The three configurations were also tested at three different vibration frequencies: 15, 18, and 21 Hz. The layout of the internal components in each sensor's box did not change between each test. A summary of the acoustically-isolated shaker table tests performed can be seen in Table 12.

Test #	**Test Configuration**	**Shaker Table Frequency (Hz)**	**Test Duration**
1	Configuration 1	15	3 minutes
2	Configuration 1	18	3 minutes
3	Configuration 1	21	3 minutes
4	Configuration 2	15	3 minutes
5	Configuration 2	18	3 minutes
6	Configuration 2	21	3 minutes
7	Configuration 3	15	3 minutes
8	Configuration 3	18	3 minutes
9	Configuration 3	21	3 minutes

Table 12: Shaker table (acoustic ports closed) test matrix.

A crucial aspect of this experiment was to isolate each sensor from the acoustic pressures of the surrounding environment in order to investigate diaphragm orientation effects only.

To do this, both the main inlet and the pneumatic filter inlet of both sensors were connected to the same tubing via tee connections. Then, the tubing was connected to a ball valve; the other end open to the surrounding ambient pressure. After the tubing/valve assembly was connected to the sensors, the tubing was taped down and the entire assembly was left alone for 5 minutes. Thus, both sides of the diaphragms in each sensor were allowed to equilibrate at a value equal to the surrounding ambient pressure. Then, before tests were executed, the ball valve was closed to disable pressure fluctuations (acoustic signals) from affecting each of the sensors. The ball valve is required to ensure the differential pressure across each sensors' diaphragm is zero (or negligible) before acoustically isolating the sensors, as plugging the inlets without the use of a valve will not guarantee zero differential pressure and may saturate the ADC (which occurred during preliminary experiments before learning a valve was required). A simplified schematic of the setup can be seen in Figure 30.

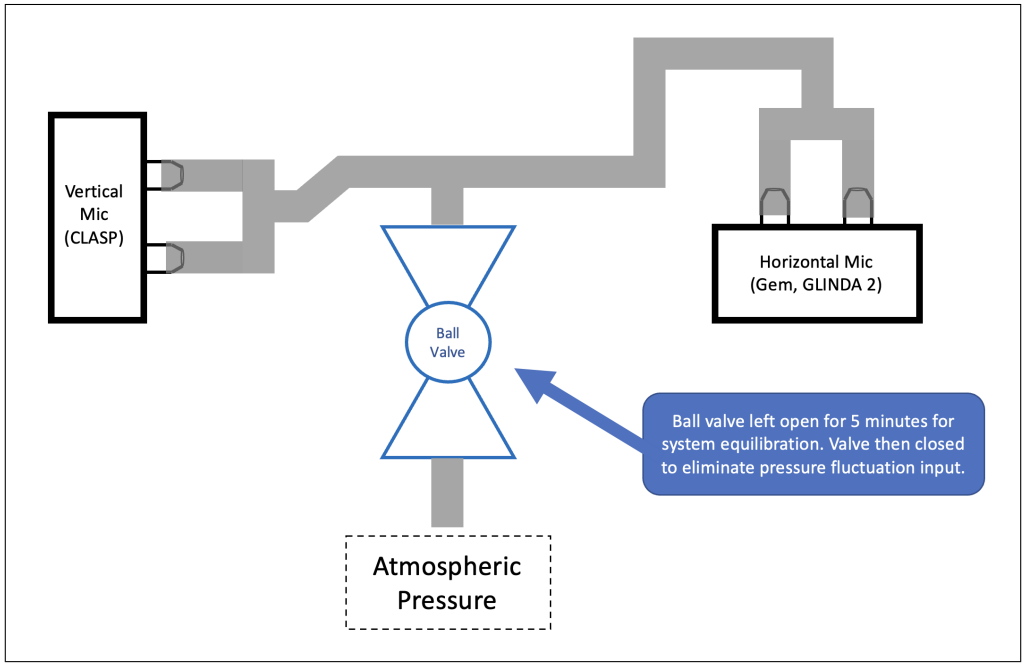

Figure 30: Schematic of valve used during closed acoustic inlets shaker table test.

All tests in Table 12 were completed, resulting in 18 sets of power spectral density data (9 acoustic, 9 acceleration). Figure 31, Figure 32, and Figure 33 show details of the data collected during the tests using configuration 1, 2, and 3, respectively. Note, in these figures,

the subplots titled "Table ⊥ Acc. PSD" signify the power spectral density of the acceleration normal to the shaker table while the subplots title "Mic. PSD" signify the power spectral density of the acoustic pressure signal captured by the pressure transducer of each sensor.

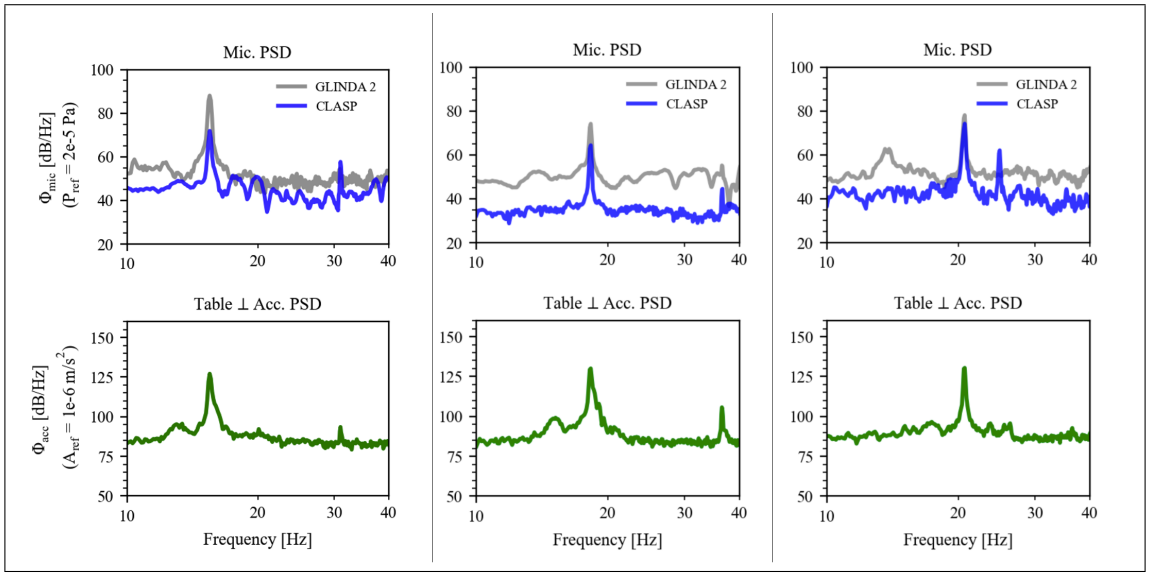

Figure 31: Closed acoustic inlet, shaker table test PSD - test 1 configuration.

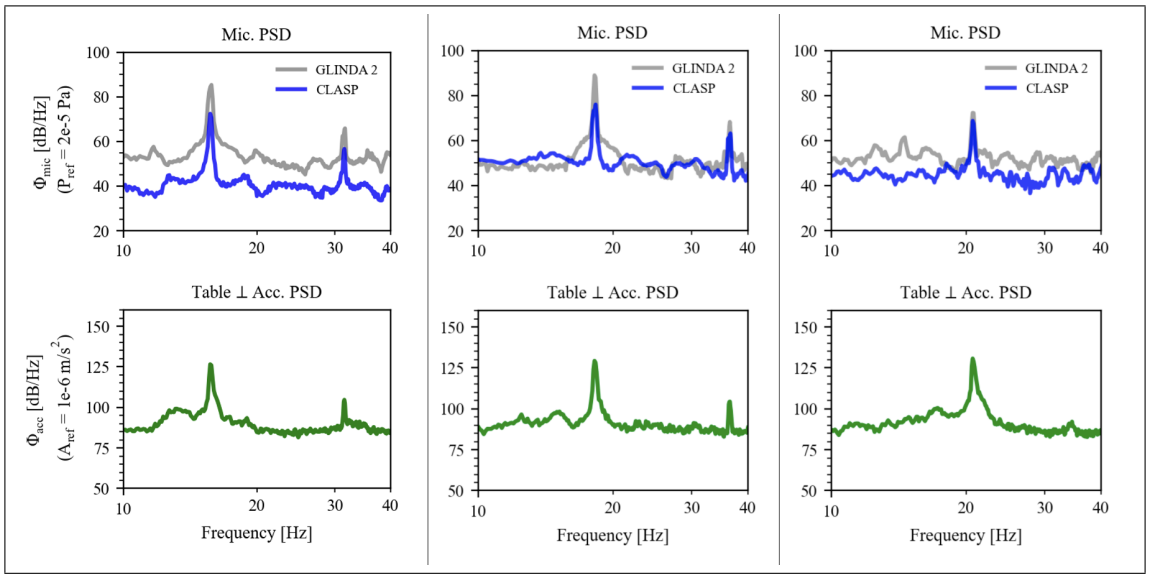

Figure 32: Closed acoustic inlet, shaker table test PSD - test 2 configuration.

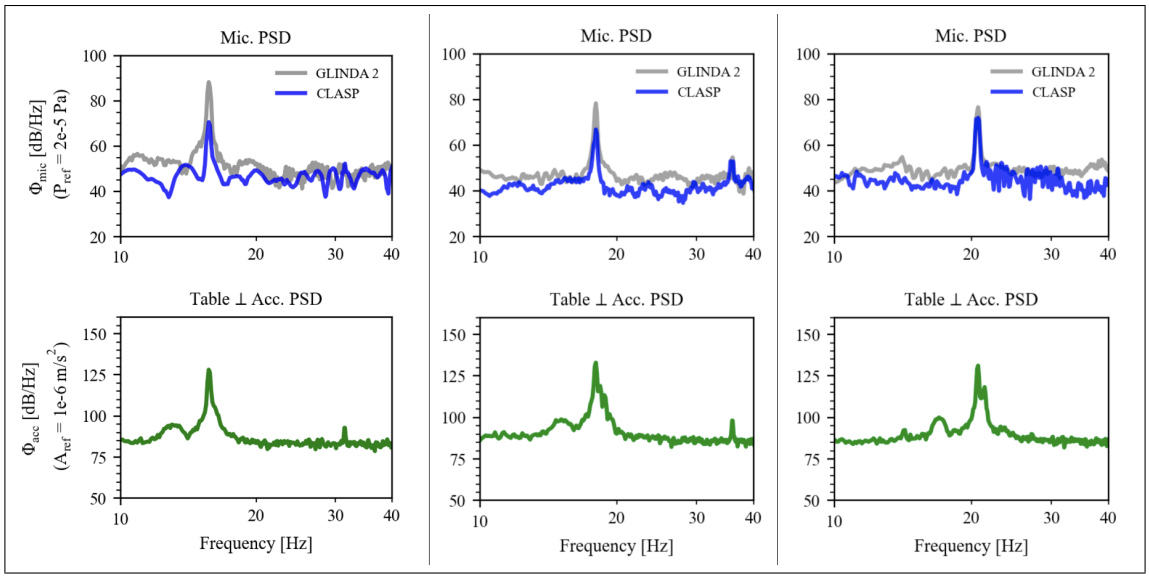

Figure 33: Closed acoustic inlet, shaker table test PSD - test 3 configuration.

Before the data in all 18 PSDs is condensed into something more digestible, there are a few trends to acknowledge in Figures 31, 32, and 33. First, the acoustic data collected by CLASP looks to be less affected by the input vibration. At each vibrational tone, there exists an acoustic tone that is higher in the GLINDA2 data for each configuration. However, CLASP was still substantially affected by the table's vibration. This is especially apparent as the input vibration frequency increases, as the 21 Hz vibration consistently shows less of a difference between the GLINDA2 acoustic tone and the CLASP acoustic tone.

To condense results down to a concise plot, a few parameters will be established. First, a metric to compare the acoustic signals from the horizontal diaphragm unit (GLINDA2) and the vertical diaphragm unit (CLASP) will be referred to as the "vibration coupling reduction" (VCR). First, consider the acoustic PSD magnitude at a particular frequency during the vibration test given by the term "$\Phi_{dB,vib}(f)$". Another term "$\Phi_{dB,o}(f)$" was defined similarly, except that the subscript "o" signifies the acoustic PSD magnitude of the self-noise floor. "$\Phi_{dB,o}(f)$" was captured by a plugged inlet test without any input vibration (Figure 65 shows this reference data in the appendix).

$$\Delta\Phi(f) = \Phi_{dB,vib}(f) - \Phi_{dB,o}(f) \tag{5.1.1}$$

$$VCR(f) = \frac{\Delta\Phi_{G2}(f) - \Delta\Phi_{C}(f)}{\Delta\Phi_{G2}(f)} \times 100 \tag{5.1.2}$$

Thus, at each vibration frequency, both GLINDA2 and CLASP will have a unique $\Delta\Phi(f)$ that depends on the sensor's response to the shaker table, as well as the sensor's reference noise floor. The primary parameter used, VCR, is simply the percent change (from GLINDA2 to CLASP) of the $\Delta\Phi(f)$ values at each vibration frequency. VCR is given in equation (5.1.2) where the subscripts "G2" and "C" signify GLINDA2 and CLASP, respectively.

Another parameter of interest is a value that quantifies the degree to which the normal acceleration, from the perspective of the vertically mounted pressure transducer on CLASP, varies from the normal acceleration of the table. Previously mentioned in Section 3.2.2, the shaker table used in this experiment does not vibrate purely in a vertical direction. Quantifying how much of the vibration energy of the shaker table was directed in the normal direction of CLASP's pressure transducer is a critical measure. Thus, the normal acceleration percent difference (NAPD) is defined here to provide a relevant metric of this acceleration. Additionally, a surface-normal acceleration term, $\psi_{s,dB}(f)$, was defined as the PSD magnitude of the acceleration normal to surface "s" at a shaker table vibration frequency (f).

$$NAPD(f) = \frac{|\psi_{T,dB}(f) - \psi_{C,dB}(f)|}{\frac{\psi_{T,dB}(f) + \psi_{C,dB}(f)}{2}} \tag{5.1.3}$$

Ultimately, NAPD is percent difference between the acceleration normal to the shaker table and the acceleration normal to CLASP's pressure transducer, given by equation (5.1.3). To clarify, "$\psi_{C,dB}(f)$" in equation (5.1.3) is the acceleration PSD magnitude (measured by CLASP's IMU) in the direction normal to CLASP's pressure transducer, while "$\psi_{T,dB}(f)$" is the acceleration PSD magnitude (measured by the accelerometer on the table) in the $+z$ direction according to the coordinate axis in Figure 28.

A summary of the results gathered from this experiment can be seen in Figure 34. Figure 34(top) displays the VCR computed from each test configuration and Figure 34(bottom)

shows the NAPD of each test configuration as well as the average NAPD over each input vibration frequency. Note, the plots in Figure 34 share an independent variable, frequency, along the abscissa. Additionally, the reader should be aware of some aspects of the NAPD parameter. First, the NAPD data seen in Figure 34 shows that CLASP's pressure transducer did not experience acceleration strictly in the vertical direction (z-direction in Figure 28). Additionally, the reader should be informed that NAPD was calculated with the maximum accelerations within a $\pm$ .25 Hz band centered around the shaker table frequency; NAPD would vary slightly if a different approach was used (i.e., using an average acceleration instead of a maximum, or changing the size of the frequency band used around the shaker table frequency).

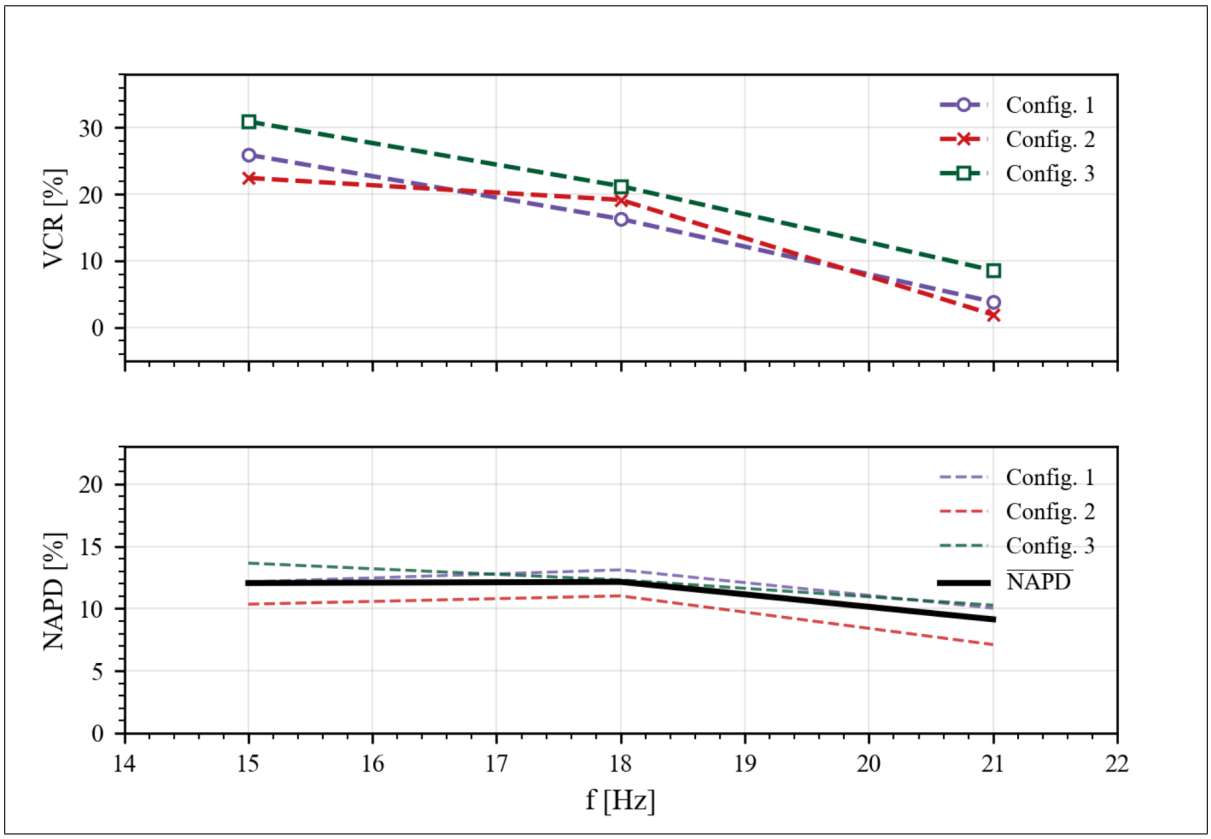

Figure 34: (top) VCR vs shaker table frequency. (bottom) NAPD vs shaker table frequency. Shaker table normal-direct was the $+z$ direction for all configurations. CLASP's pressure transducer normal direction was $-y$ for configurations 1 and 2, and $-x$ during configuration 3.

Figure 34 suggests that CLASP's vertically mounted pressure transducer provides some

effectiveness at reducing seismo-acoustic coupling in an acoustically-isolated environment. The effectiveness is greater at lower vibration frequencies in the range of frequencies tested, and quickly decreases as the vibration frequency increases. While deploying a microbarometer in an acoustically-isolated environment is unproductive, this experiment does provide insight to an aspect of sensor design. Ultimately, the results of this experiment suggest that the orientation of an infrasound sensor's diaphragm can have an effect on the degree of vibrationally-induced signal.

5.1.2 Open Acoustic Inlets

To further the understanding of seismo-acoustic coupling, the shaker table was used to investigate another suspected parameter of mobile infrasound sensing: coupling effects via inlet tubing. Both GLINDA2 and CLASP were placed in the center of the shaker table and vibration tests (similar to the previous section) were performed. However, the inlets of the sensors were not plugged and were open to the surrounding environment. Additionally, a third configuration was used that consisted of a CLASP unit with about 18 inches of inlet tubing connected to its primary acoustic inlet. A top-view schematic of the configurations used in this experiment can be seen in Figure 35, and pictures from the test can be seen in the appendix. Lastly, the test matrix can be seen in Table 13.

Test #	**Sensor Used**	**Sensor Configuration**	**Shaker Table Frequency (Hz)**	**Test Duration**
1	CLASP	Nominal	0	3 min
2	CLASP	Nominal	15	3 min
3	CLASP	Nominal	18	3 min
4	CLASP	Nominal	21	3 min
5	CLASP	LH	0	3 min
6	CLASP	LH	15	3 min
7	CLASP	LH	18	3 min
8	CLASP	LH	21	3 min
9	GLINDA 2	Nominal	0	3 min
10	GLINDA 2	Nominal	15	3 min
11	GLINDA 2	Nominal	18	3 min
12	GLINDA 2	Nominal	21	3 min

Table 13: Shaker table test matrix with acoustic ports open. LH: "long hose" CLASP unit.

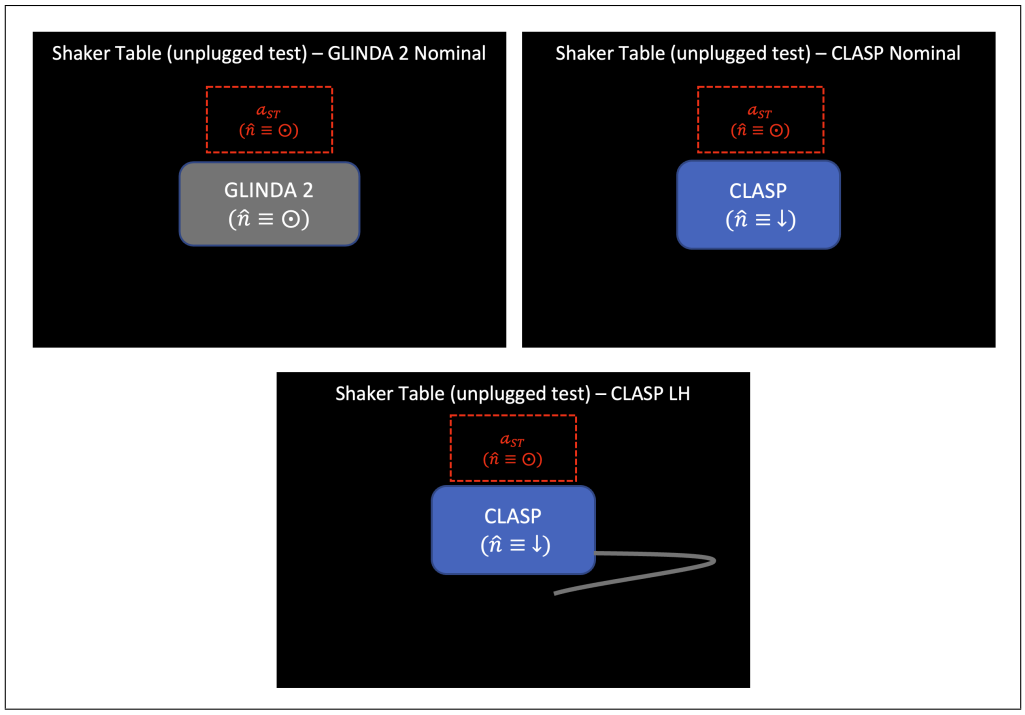

Figure 35: Schematic of the shaker table tests with the acoustic ports open.

Figure 36, Figure 37, and Figure 38 display the results from this experiment for the 15 Hz, 18 Hz, and 21 Hz vibration input, respectively. In each of these figures, the acoustic data collected from the three sensors is colored according to the legend of each "Mic. PSD" plot while the "Acc. PSD" plot displays the acceleration PSD collected from the accelerometer on the shaker table. Additionally, the reader will notice the thin black lines in each plot; which are the acoustic and acceleration PSDs collected during a 0 Hz vibration test (i.e., ambient acoustic and vibration data measured by CLASP before beginning the experiment).

There are a few notable characteristics in the acoustic PSD data for each sensor. First, the reduction of seismo-acoustic coupling is less apparent in the results when compared to the experiment presented in the last section (Section 5.1.1). While there seems to be some reduction, it is clear that the vertical pressure transducer in CLASP is affected by the vibrations; along with the long hose CLASP configuration and GLINDA2. However, Figures 36, 37, and 38 do seem to show an increase in the coupling experienced by the long hose version of CLASP, perhaps even more so than GLINDA2.

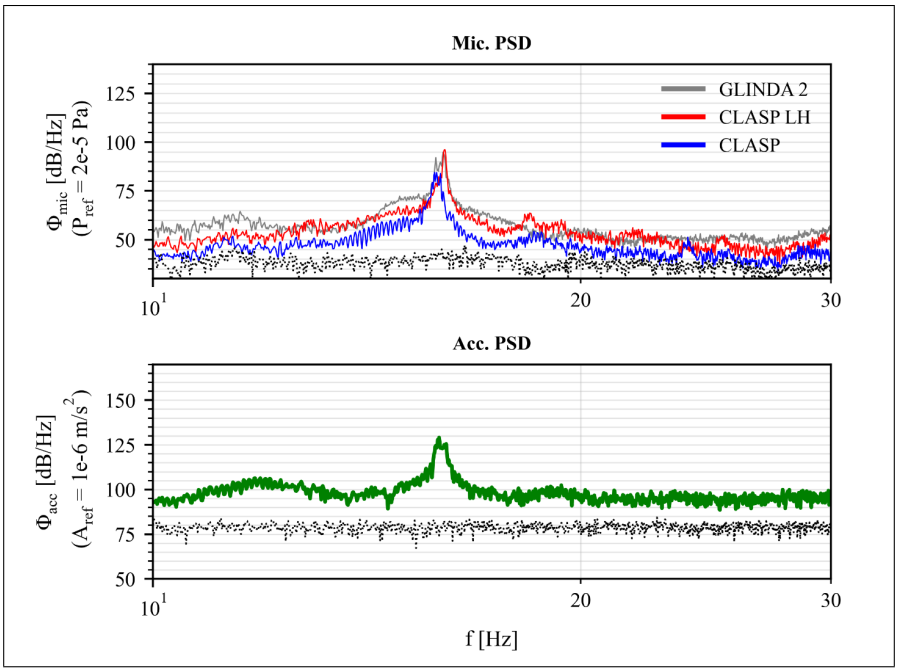

Figure 36: (top) Acoustic PSD and (bottom) acceleration PSD with 15 Hz vibration and open acoustic inlets. Thin black lines are acoustic and acceleration PSDs at 0 Hz vibration (ambient data).

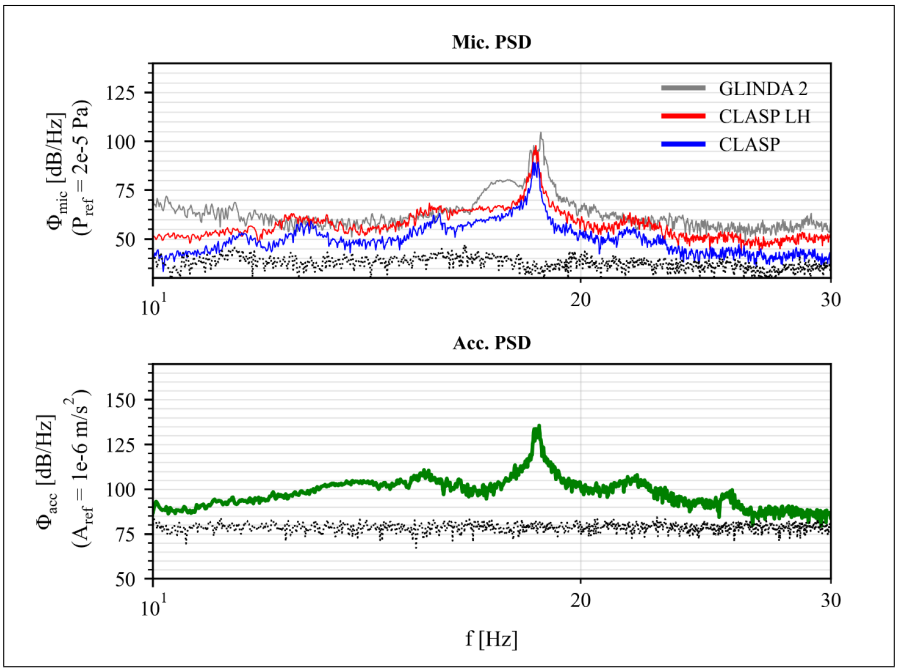

Figure 37: (top) Acoustic PSD and (bottom) acceleration PSD with 18 Hz vibration and open acoustic inlets. Thin black lines are acoustic and acceleration PSDs at 0 Hz vibration (ambient data).

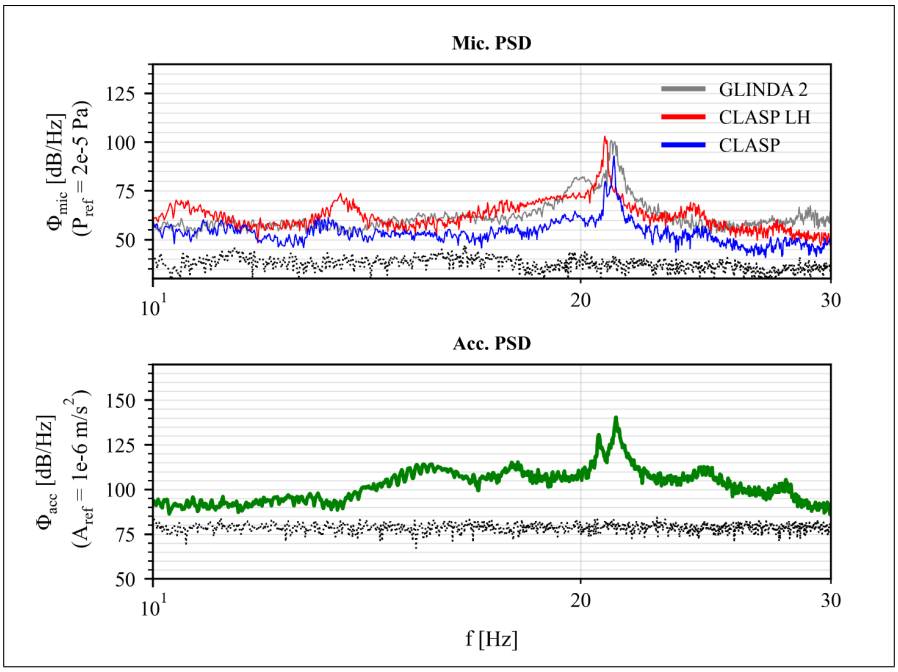

Figure 38: (top) Acoustic PSD and (bottom) acceleration PSD with 21 Hz vibration and open acoustic inlets. Thin black lines are acoustic and acceleration PSDs at 0 Hz vibration (ambient data).

To summarize the PSD of both the acceleration and acoustic pressure data, for the CLASP and GLINDA2 units, the peak amplitude was determined for each data and each sensor. Ultimately, the "long hose" inlet tube CLASP configuration was impacted substantially more by the vibrations of the table when compared to the nominal CLASP configuration. Additionally, it is suspected that the horizontal diaphragm present in the GLINDA2 unit impacted its acoustic response to a similar degree. These outcomes can be seen in Figure 39, where each line represents a sensor configuration and it's acoustic PSD peak at each respective acceleration PSD peak (plotted with green arrows).

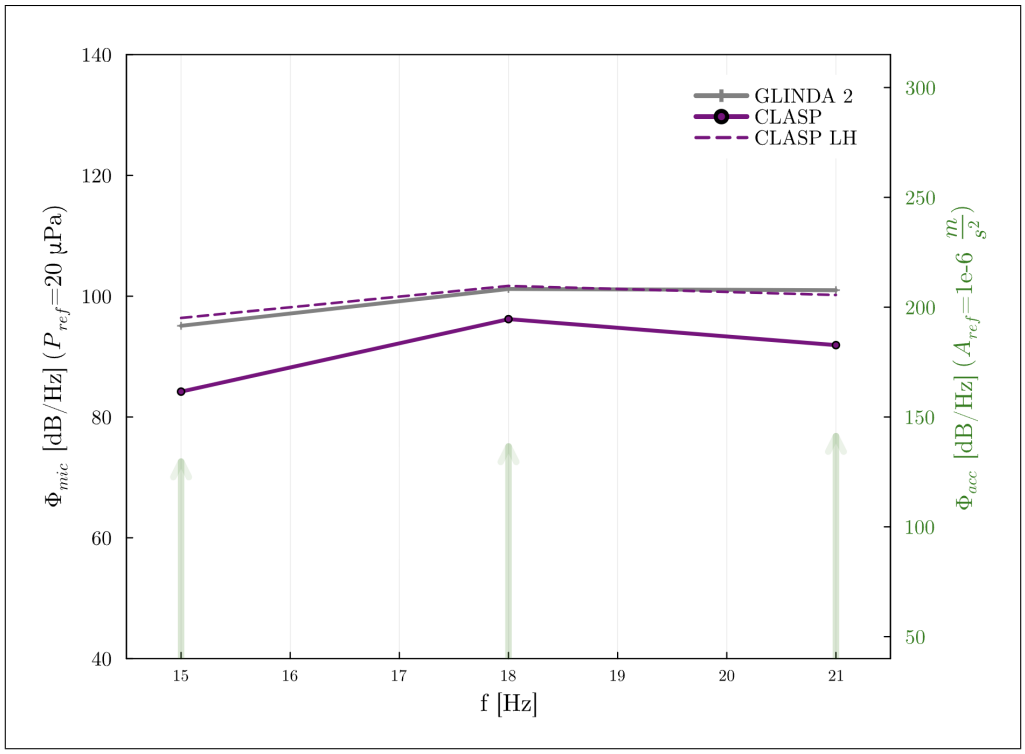

Figure 39: Acoustic signal PSD (left axis) and acceleration signal PSD (right axis) vs vibration frequency during open acoustic inlet shaker table test.

Figure 39 suggests that the benefits of a vertically mounted diaphragm (results previously mentioned earlier in this section) are, essentially, offset by the impact of excessive inlet tubing length. Ultimately, the results gathered from this experiment imply the length of inlet tubing used in infrasound sensors can drastically affect the coupling between vibrations and the pressure signal acquired by sensors like the ones used here. While the tubing length used in this experiment is excessive, researchers should keep this effect in mind and ensure minimum tubing is used and all tubing is secure when deploying infrasound sensors in seismic environments.

5.2 Vehicle Field Testing

Both GLINDA systems were deployed among storm chasers in a storm-chasing vehicle and, as previously discussed, collected acoustic data with unexpected spectral structure. Thus, a more controlled vehicle-based experiment is required to further understand the data collected

by both GLINDA systems. The most common types of roads driven on by the vehicle that housed both GLINDA packages were state highways, city streets, and dirt/gravel roads in remote locations. This experiment will expose both a CLASP unit and a GLINDA2 unit to similar road conditions and will compare the acoustic and seismic data from each sensor. GLINDA2 was outfitted with an accelerometer for this test, while CLASP was in its nominal configuration (with an embedded IMU, vertically mounted pressure transducer, etc.).

Both sensors were configured in the rear-seat floor of an SUV (similar to Figure 7) and secured to 20 lb flat stones, seen in Figure 40, to mitigate a potentially weak connection between the vehicle's floorboard and the sensors using alternative methods like Velcro or temporary adhesives. The SUV was then exposed to each of the three road conditions for more than 10 minutes, and the test matrix outlining this experiment can be seen below in Table 14. A map of the route driven during this experiment can be seen in Figure 69 in the appendix.

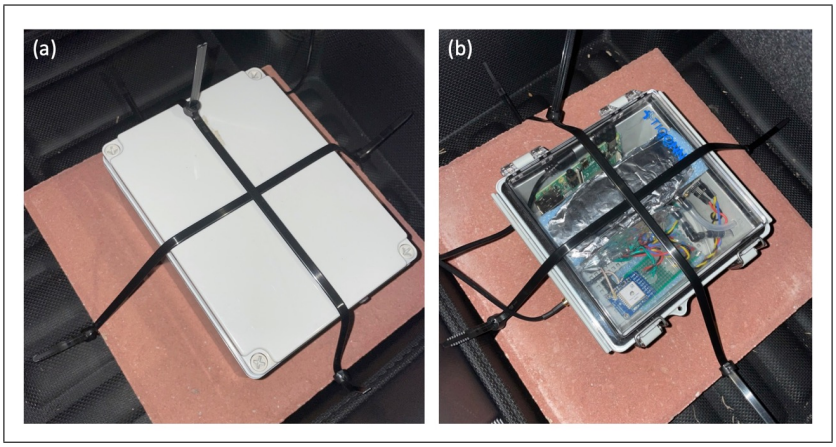

Figure 40: (a) GLINDA2 unit and (b) CLASP unit during vehicle-based field test.

Test #	**Road Type**	**Nominal Speed**	**Test Duration**
1	City Road	40 mph	>10 min
2	Highway	65 mph	>10 min
3	Dirt Road	30 mph	>10 min

Table 14: Vehicle field testing - test matrix.

Considering each sensor was collecting pressure data and 3 components of acceleration

data during all three road conditions, there is quite a bit of data to present in this section. A good start is to inspect a spectrogram (see Section 3.3 for spectrogram definition) of the data throughout the entire experiment. Figure 41 shows the annotated spectrogram of CLASP'S acoustic data collected throughout the entire experiment. The data in Figure 41 displays

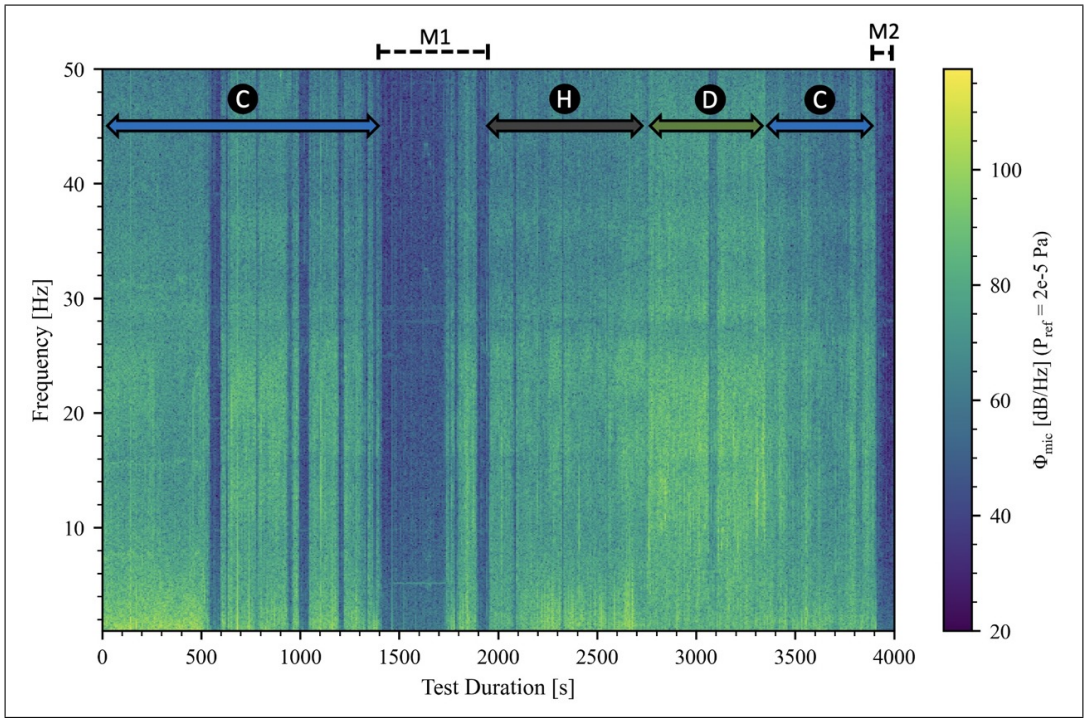

Figure 41: Spectrogram of CLASP acoustic data throughout vehicle-based field test. C: city roads; H: state highway; D: dirt road; M1/M2: stationary.

some expected behavior; less acoustic energy seen during times when the vehicle is stopped, and similar signatures for highway and city road conditions. Additionally, the spectrogram shows a broadband increase in acoustic energy while the vehicle was traversing dirt roads which, based on the previous experiment results shown in this paper, was not a surprise. However, Figure 41 doesn't show the persistent 15-20 Hz energy seen in previously collected GLINDA2 data (Figure 12). Furthermore, an annotated spectrogram of the acceleration data collected by CLASP, presented in Figure 42, correlates well with the acoustic spectrogram.

Power spectral densities extracted from the pressure and acceleration data will provide more context on the effects of the vehicle dynamics on the sensors. A PSD operation was performed on both the pressure data and the vertical acceleration data collected by CLASP

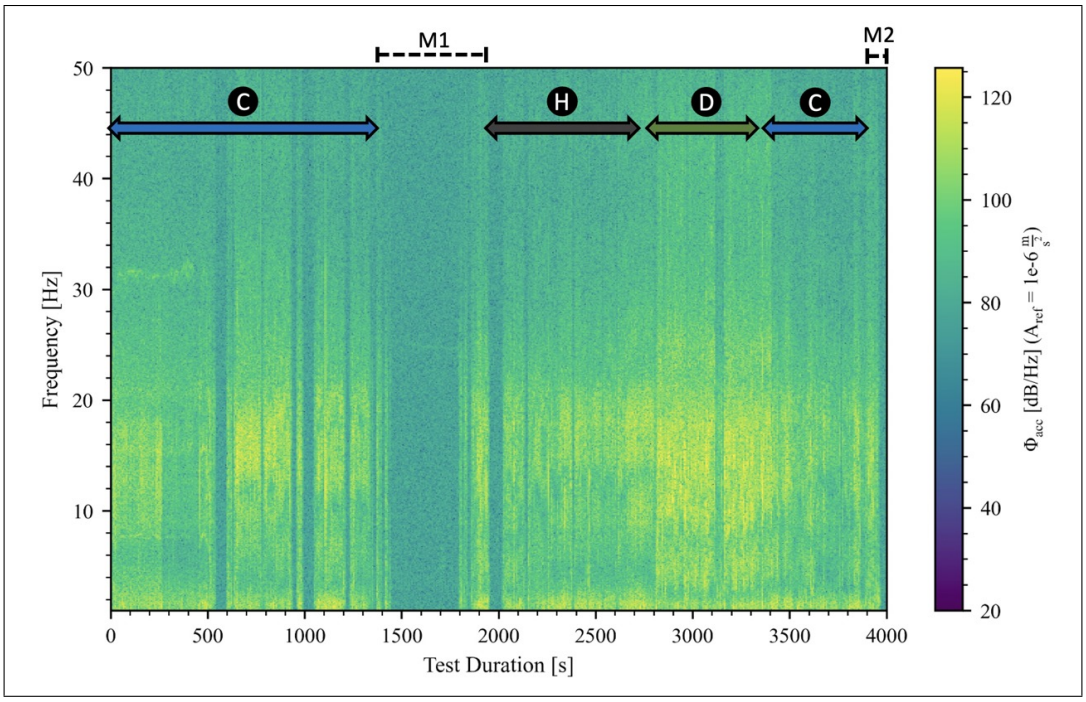

Figure 42: Spectrogram of CLASP acceleration data throughout vehicle-based field test. C: city roads; H: state highway; D: dirt road; M1/M2: stationary.

and GLINDA 2, where "vertical acceleration" is the acceleration in the gravity vector ($\hat{g}$) direction. In the spectrogram provided in Figure 41, the bands of low energy (while the vehicle was stationary) serve as a proper baseline. The PSDs of both acoustic and acceleration data during stationary periods of the vehicle-based test are presented in Figure 43. The reader should note the shape of the data sets in both Figure 43(top) and Figure 43(bottom); the acceleration data is essentially flat across the range of frequencies, but the acoustic data is not. This suggests that the tones in Figure 43(top) are purely acoustic. In fact, it was observed that the SUV used for testing idles between 600 rpm and 800 rpm (a function of engine temperature), and given that it was a 4-stroke engine, this would lead to a firing frequency of 5-6.5 Hz. Thus, the tone near 5 Hz was likely pistons firing within the engine of the SUV (an unimportant, but fascinating quantity to see in the data).

Since each test consisted of primarily constant velocity driving, the main source of acceleration oscillations was due to the bouncing of the vehicle (predominantly occurring in the gravity vector direction). Figure 44, Figure 45, and Figure 46 show the PSD of the

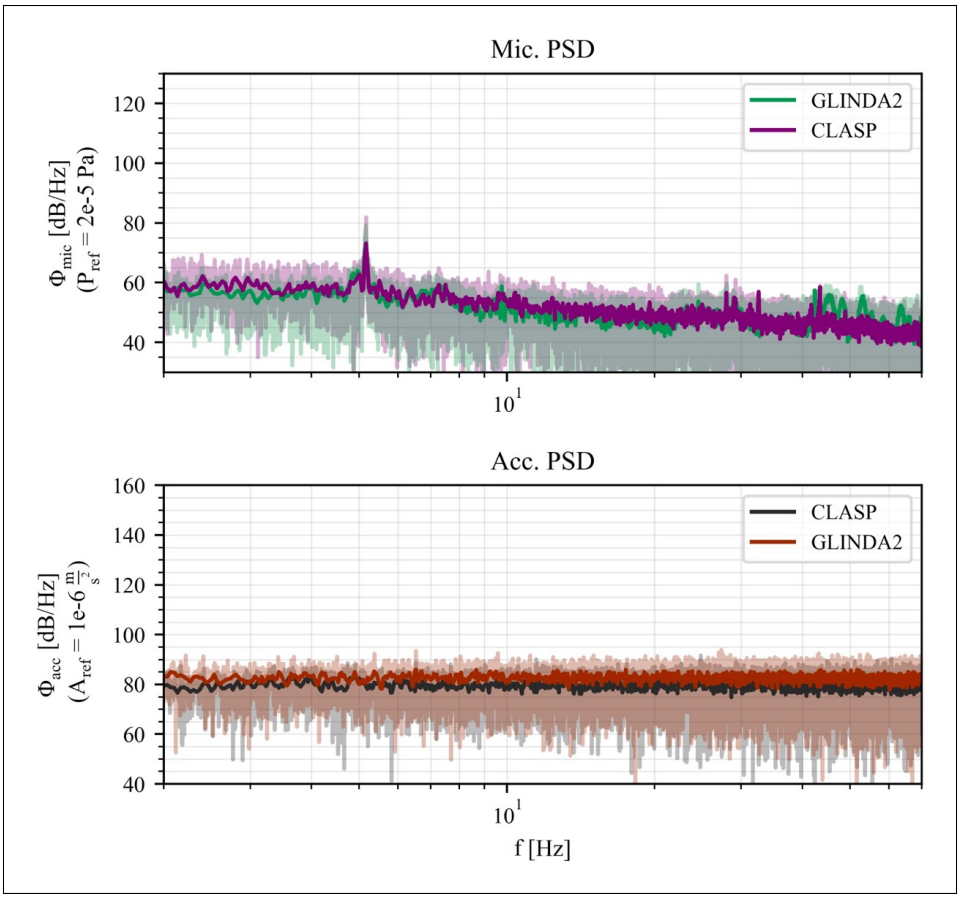

Figure 43: PSD of acoustic (top) and vertical acceleration (bottom) data during the stationary portions of vehicle field test.

data collected during the city road, state highway, and dirt road portions, respectively, of the vehicle-based field test. In these three figures, the large transparent lines are the PSD output for no windowing being applied, while the more opaque lines (provided in the legends of each figure) are the PSD results after windowing parameters have been applied. Additionally, the stationary PSD collected by CLASP (data from Figure 43) is included in each of the PSDs for reference.

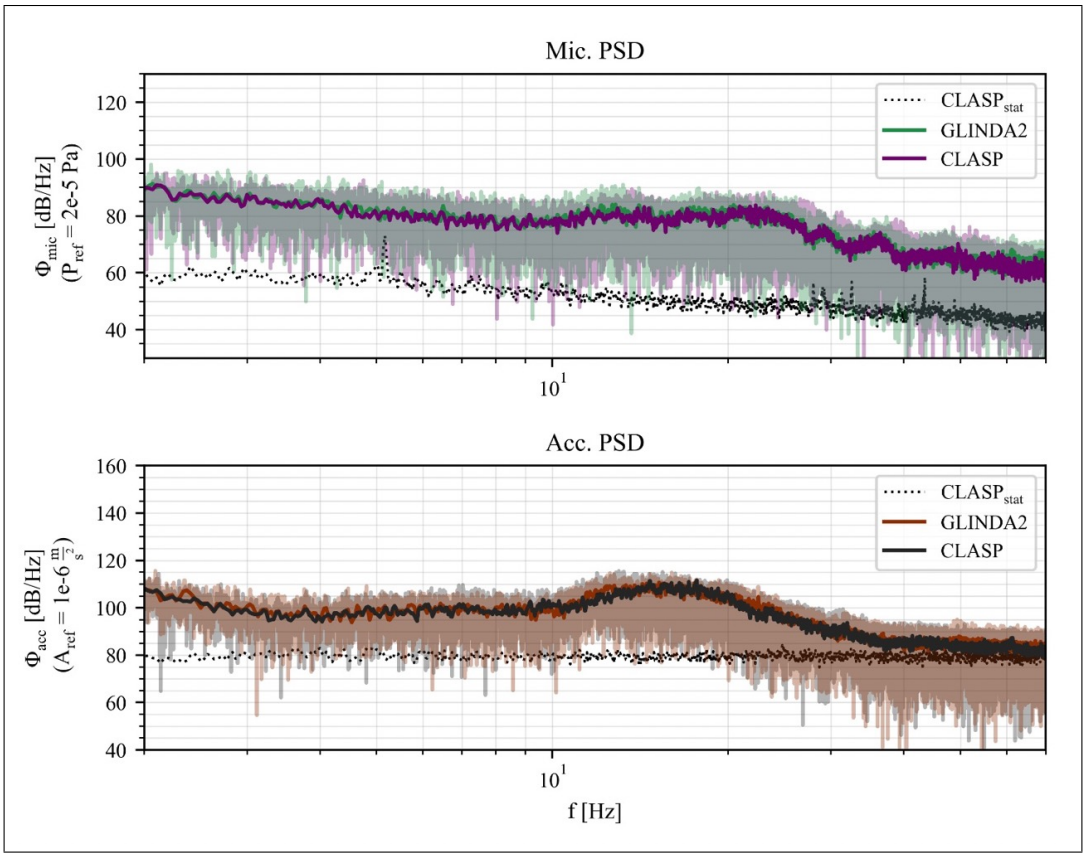

Figure 44: (top) PSD of acoustic and (bottom) vertical acceleration data during city roads portion of vehicle field test.

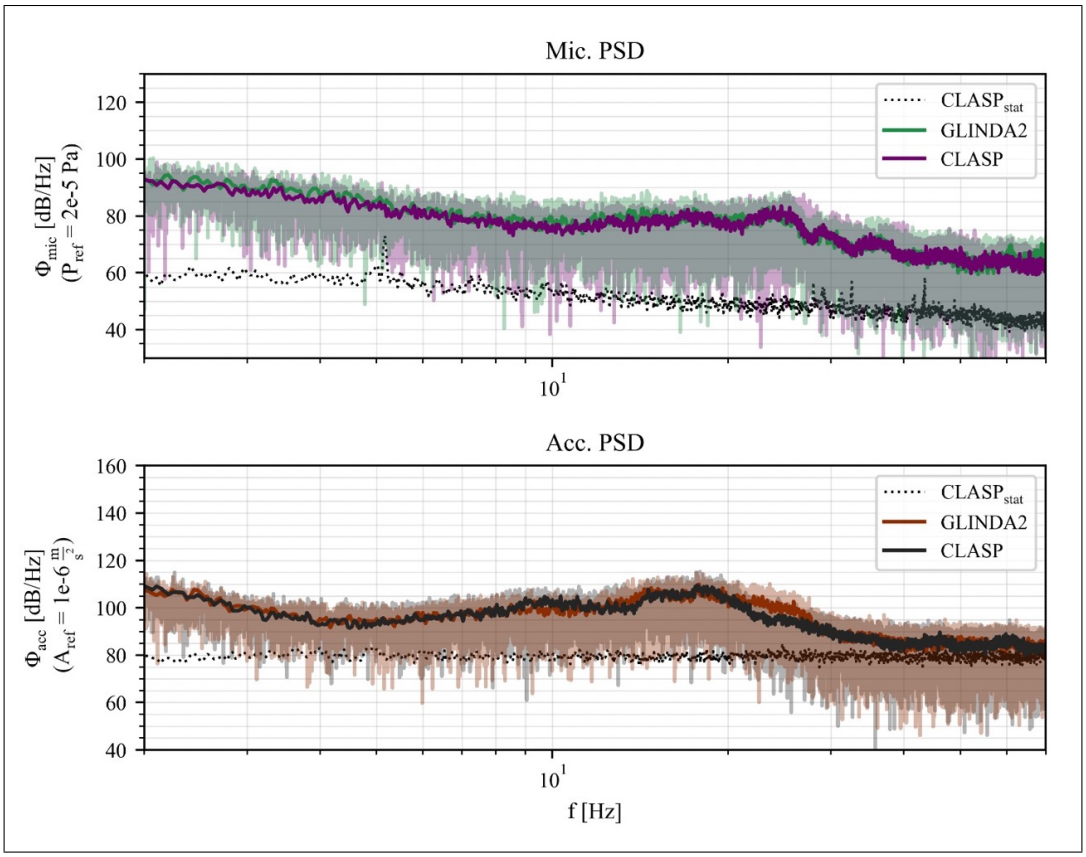

Figure 45: (top) PSD of acoustic and (bottom) vertical acceleration data during state highway portion of vehicle field test.

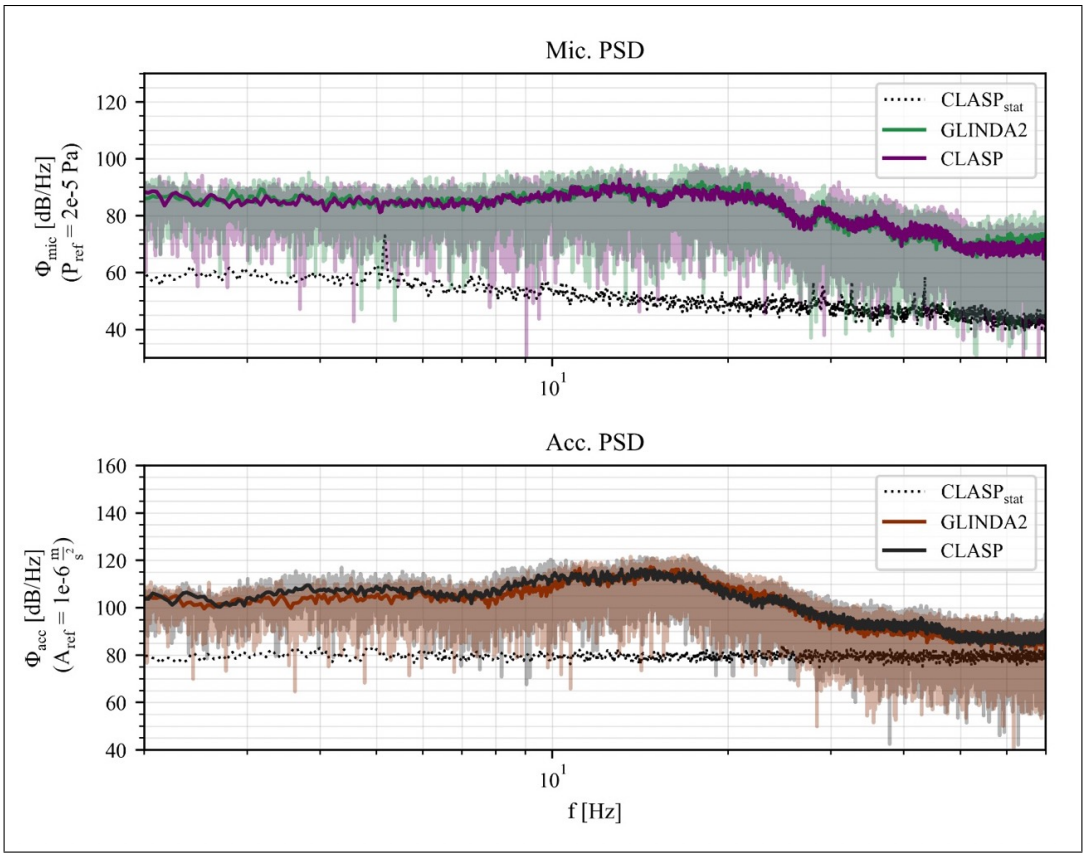

Figure 46: (top) PSD of acoustic and (bottom) vertical acceleration data during dirt road portion of vehicle field test.

Figures 44, 45, and 46 reveal more quantitative information than the spectrogram presented in Figure 41. Each of the road conditions show a swell of spectral content, for both acceleration and acoustic data, in the 10-30 Hz region. Additionally, the PSD of the data collected during the "dirt road" condition shows more overall energy, especially in the 10-30 Hz range, than the other road conditions which was also observed in the spectrogram mentioned previously in this section. The magnitude of these swells in spectral content, in the range of 10-20 Hz during each road condition, is similar to that seen in the data collected by both GLINDA systems during their field deployments (presented in Sections 1.4.2 and 2.1).

The PSDs of each road condition provide useful information, but there is an additional processing method that can further refine the results: the cross power spectral density. Cross power spectral density (CSD) describes the correlation between the spectral content of the power contained in two distinct signals. It's most commonly used among experimentalists to investigate how related two signals collected from similar sensors are, and is often represented by the Greek letter "gamma" (γ). Performing a CSD operation on two signals with different units seems to be atypical based on current literature, but there is nothing intrinsic about the CSD that prohibits this approach; normalizing the input signals, though, promotes objectivity when dealing with different units. The cross power spectral density of CLASP's acoustic data and road-normal (vertical) acceleration data, after normalizing both signals, can be seen in Figure 47.

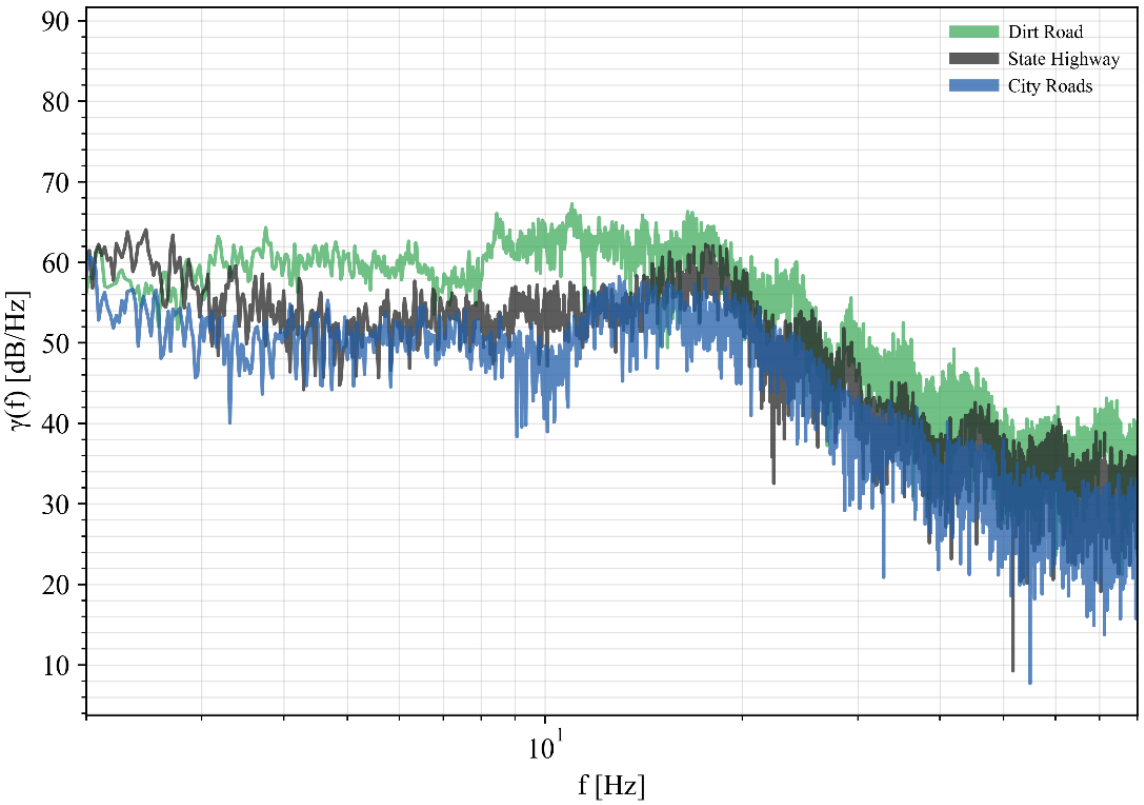

Figure 47: CSD of normalized acoustic and vertical acceleration data during vehicle-based field test.

Figure 47 confirms that the energy contained within the acoustic and road-normal (vertical) acceleration data from CLASP correlate substantially more in the infrasonic range of frequencies than frequencies above 20 Hz. Additionally, the CSD results indicate that within the region of high correlation, a particularly high CSD value exists in the 13-19 Hz band for all road conditions; the same frequency band which GLINDA1 and GLINDA2 saw high spectral content during their respective tornado chases. This correlation is apparent when comparing the CSD of GLINDA2's acoustic data during the vehicle field test, seen in Figure 48(top), and the PSD data collected by both GLINDA systems during their tornado chases, shown in Figure 48(bottom).

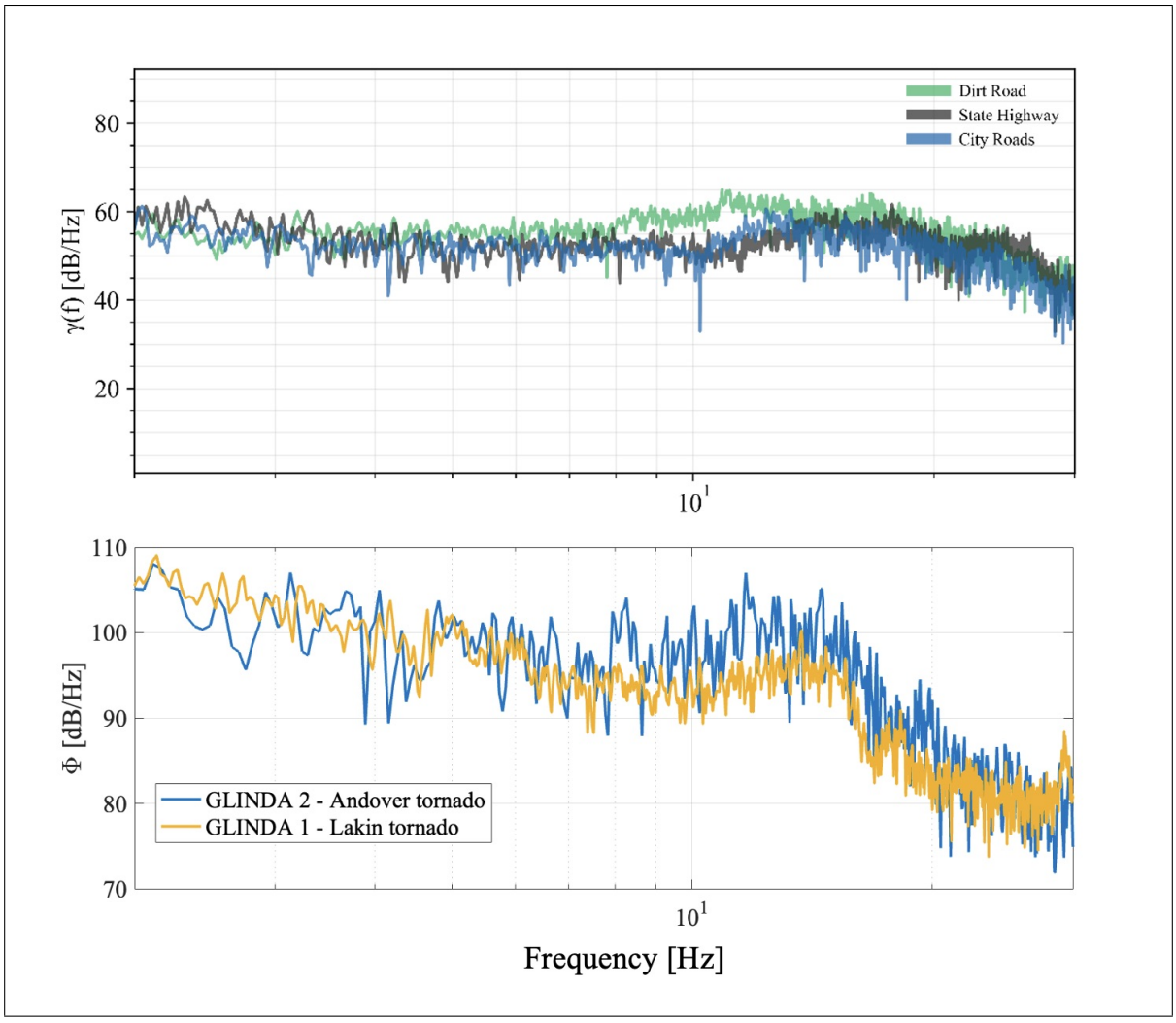

Figure 48: (top) CSD of normalized acoustic and normal acceleration data during vehicle-based field test from GLINDA2. (bottom) GLINDA1 and GLINDA2 data during tornado chases.

The trend in Figure 48(bottom) between 1-10 Hz resembles structure commonly observed from broadband noise (wind, rain, turbulence, etc.), based on previous studies (e.g. [70, 2]), and a sharp rise in both GLINDA1 and GLINDA2 spectra occurs around 11 Hz; implying a signal unlike the broadband noise caused the swell between 11-17 Hz in both sets of tornado data. Now, looking at Figure 48(top), there is also a steady trend of CSD values during the city roads and state highway portion between 1-10 Hz; just like Figure 48(bottom), this trend is interrupted by a sharp rise in spectral content that spans 11-25 Hz. It is likely the dirt road CSD data does not show a sharp rise of the same degree due to more broadband signal present

in the acoustic and acceleration PSD data (Figure 46). Ultimately, the similar behavior of both plots in Figure 48 suggests the GLINDA systems were influenced by vibrations and the infrasound observed is unlikely to be a product of a tornado.

Revisiting Figures 44, 45, and 46, there is one more aspect of the data in these figures that should be mentioned: the resemblance of both structure and magnitude present in CLASP and GLINDA2 acoustic PSD data. This suggests the seismo-acoustic coupling experienced is more so an acoustically-related parameter and less so a product of diaphragm/sensor dynamics; the different configurations of the components within GLINDA2 and CLASP produced nearly identical acoustic PSD results. Ultimately, the data presented in this section suggests that the primary factor responsible for seismo-acoustic coupling in a field environment is an oscillation of static pressure due to the height of the sensor changing.

5.3 UAV-mounted Test

5.3.1 UAV Testing

One platform which, based on literature, has not been experimentally evaluated for infrasound sensing are unmanned aerial vehicles (UAVs). Thus, an experiment was performed in collaboration with USRI, using the UAV described in Section 3.2.3. CLASP was secured to the UAV according to Figure 49a and three UAV states were considered during testing (inactive, idle spin-up, and hover). Additionally, the infrasound source mentioned in Section 3.2.1 was playing a 20 Hz tone, placed about 60 ft away from the UAV, throughout the experiment.

The layout of the infrasound source and the UAV can be seen in the schematic in Figure 50a, and a first-person view during the experiment can be seen in Figure 50b. The first of the three UAV states was an "inactive" state. During the inactive state, the UAV was not powered on and was stationary on the ground. The second of the three states was an "idle spin-up" state, where the UAV was stationary on the ground but its propellers were spinning

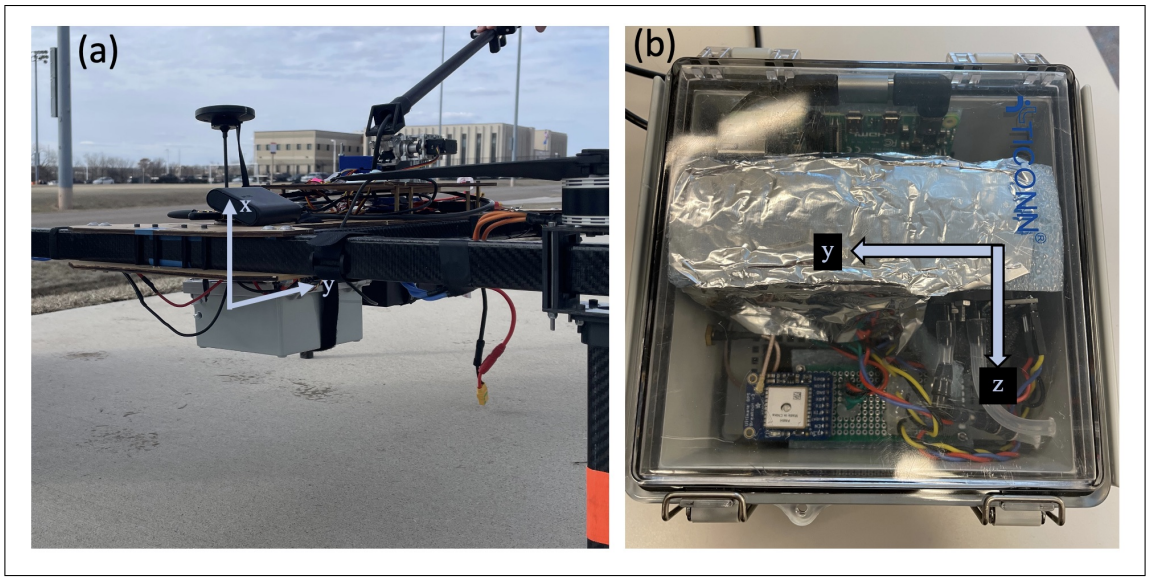

Figure 49: (a) CLASP attached to UAV. (b) CLASP coordinate system for reference.

at about 600 rpm. The last of the three states was a "hover" condition, in which the UAV was hovering 25 ft above the ground. The test matrix for this experiment can be seen in Table 15.

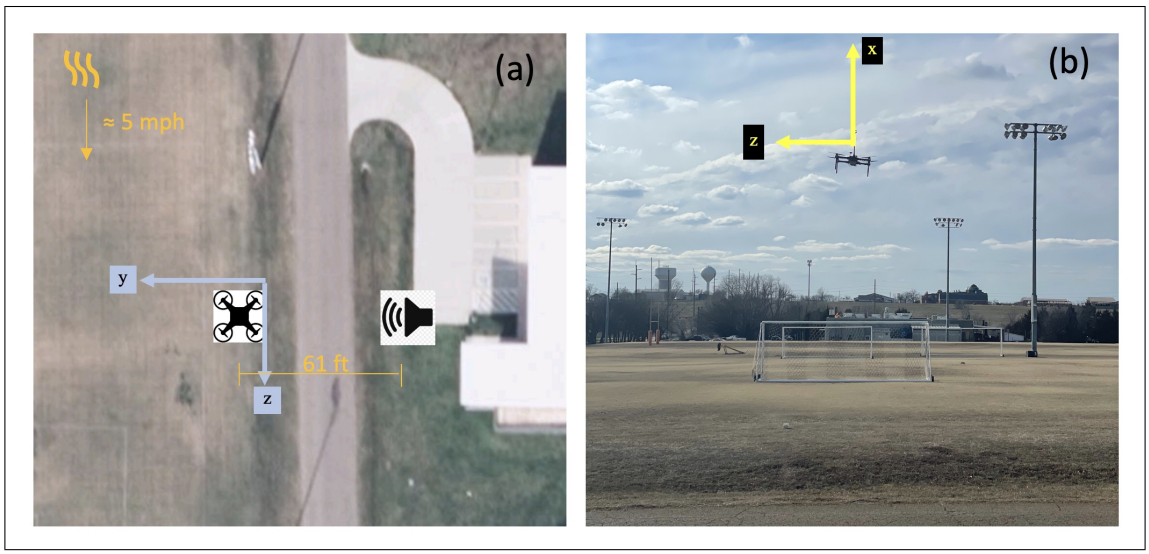

Figure 50: (a) Satellite view of experimental setup. (b) First-person view of hovering portion of experiment.

Test #	UAV State	Acoustic Source Input	Test Duration
1	Inactive	20 Hz	3 min
2	Idle spin-up	20 Hz	3 min
3	Hover	20 Hz	3 min

Table 15: UAV-based field test - test matrix.

While the UAV was inactive and grounded, the resulting PSD of both the acceleration and acoustic data from CLASP did not present any surprises. All noise floors are relatively low, and the tone from the subwoofer source was seen in the acoustic data, rising about 15 dB above neighboring spectral content. The data from the inactive portion of the experiment can be seen Figure 51, and a dashed line at the input subwoofer signal of 20 Hz is available for reference.

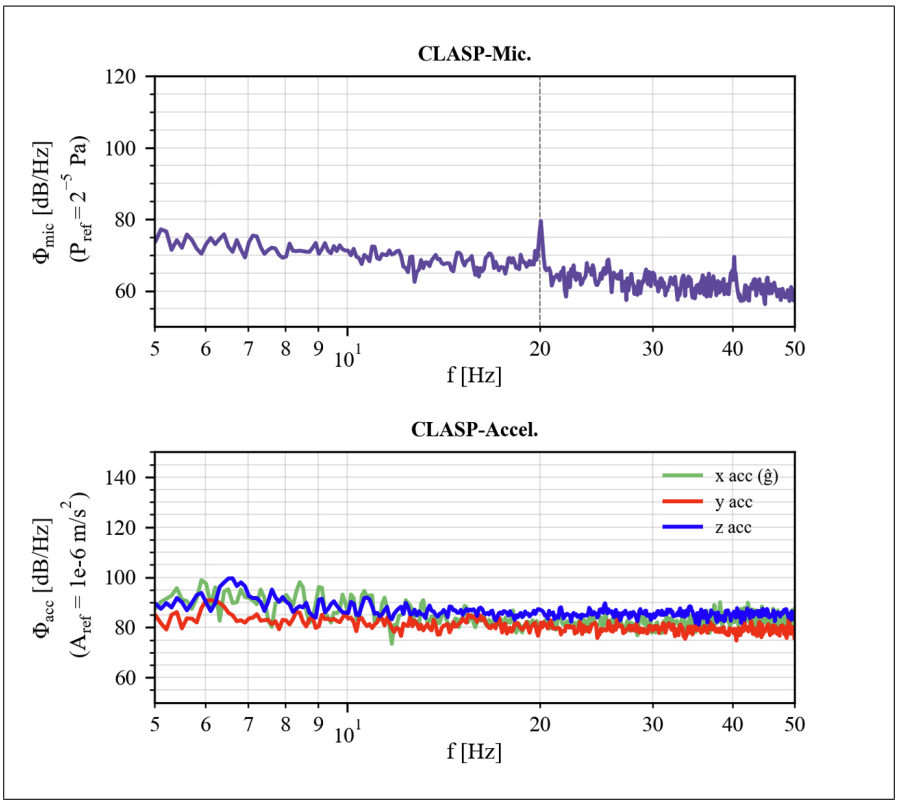

Figure 51: (top) Acoustic PSD and (bottom) acceleration PSD collected during grounded and inactive UAV testing.

After the UAV started its spin-up procedures, some interesting things can be seen in the data. Displayed in Figure 52(top), a significant suppression of the subwoofer signal

was observed. Attenuation of sound energy has been covered in many fluid dynamics and acoustics textbooks, and the relationship between turbulent wind and sound attenuation has been studied in prior work (e.g., [71, 72]). Thus, it was anticipated that some degree of attenuation would occur. However, the attenuation of about 3 dB is also accompanied by a global rise in the acoustic noise floor which, when combined, made identifying the tone from the subwoofer more difficult.

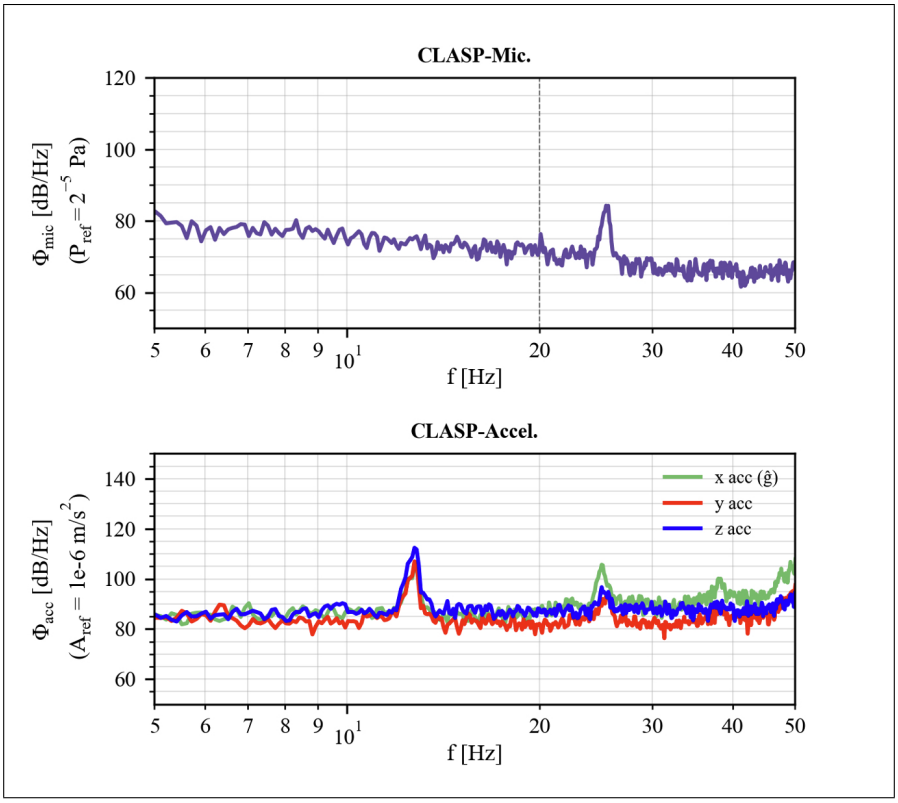

Figure 52: (top) Acoustic PSD and (bottom) acceleration PSD collected during idle spin-up UAV testing.

Additionally, Figure 52(bottom) shows tonal-like regions in the acceleration PSD. However, only one of these regions (around 25 Hz) correlates with an affected region in the acoustic PSD data as well. This coupling seems to have increased the acoustic spectral content by ≈15 dB. Moving focus to the other tonal-like region in the acceleration PSD data (around 13 Hz) invokes some questions. It is inconclusive why this region does not have a constituent tonal-like region in the acoustic data. Electromagnetic noise could have caused

this behavior due to the lack of protective foil around CLASP near the accelerometer; this is speculation though, as no other factors are suggested by the acoustic and acceleration data.

Once the UAV began to hover, it was suspected that the acoustic data would be drastically affected. One quickly develops an intuition of how turbulent and chaotic the pressure field surrounding the vehicle is after spending time around UAVs. The affects from hovering can be seen in Figure 53, and the UAVs impact on CLASP's acoustic signal floor is apparent; the acoustic floor rises drastically in this state. The magnitude of the broadband acoustic spectral content infers that even if there was no attenuation, CLASP would still not be able to detect the source; the energy from the source (shown in the grounded and inactive test results) was buried underneath the noise floor during hover. Additionally, the acceleration PSD in Figure 53(bottom) exhibits a broadband rise. When compared to the ground spin-up test, the PSD of the accelerometer data shows an increase in a broadband manner by 20-30 dB.

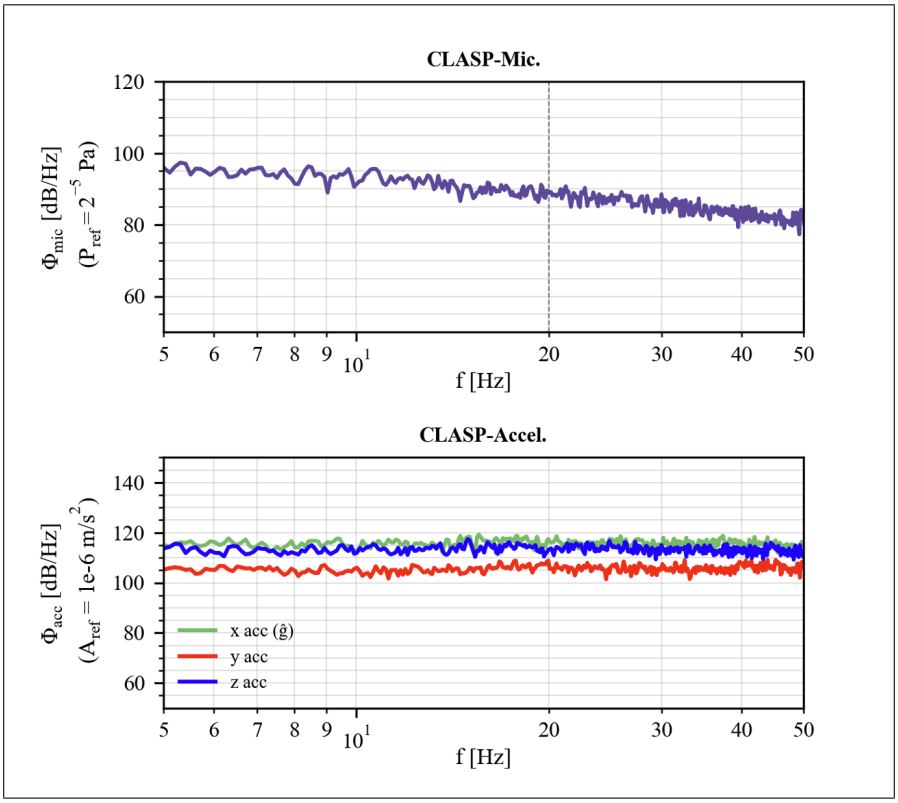

Figure 53: (top) Acoustic PSD and (bottom) acceleration PSD collected during hover UAV testing.

Ultimately, the data gathered from the spin-up test displays an attenuation of the acoustic source, likely due to the four propellers on the UAV introducing turbulence and shear. It is anticipated that this attenuation is present in the hover test data as well. However, the hover test experienced an increase in the vibrational noise floor along with an increase in the acoustic noise floor; swamping whatever may have remained of the infrasound source. All in all, significant work is required to lower the noise floor, as well as overcome the impact of vibrations, before infrasound sensing from a UAV is possible.

CHAPTER VI

CONCLUSIONS AND FUTURE WORK

6.1 Conclusions

The first conclusion worthy of discussion is that a custom sensor package, called CLASP, was made and presented in this thesis; of which is a low-cost option for fellow researchers to reference. CLASP performs similar to other non-proprietary sensors in the infrasound sensing space while also offering cloud-based storage capabilities, as well as an open-source framework to record acoustic pressure data, GPS data, and acceleration data. The customizability of CLASP served a crucial role in the experiments performed in the work presented, and offers a platform for others to directly use or modify using its open-source hardware and source-code. Ultimately, CLASP will likely continue to be utilized by the community as a viable alternative to expensive sensors while also providing additional all-in-one capabilities that aren't offered by most other infrasound sensors.

CLASP's role in the experimental endeavors of this thesis directs this discussion to the second noteworthy conclusion. Four experiments were performed in Chapter V, all of which were executed to determine what factors are at play in the coupling of vibrations and acoustic signals acquired by infrasound sensors. The shaker table tests in Section 5.1 showed that both the orientation of a sensor's pressure transducer and the inlet tube dynamics can amplify seismo-acoustic interactions. However, the UAV-based and vehicle-based experiments in Section 5.3 and Section 5.2 suggested something very important: optimizing for diaphragm orientation and tube dynamics is not enough. Using the optimized internal configuration of CLASP did not overcome the fact that the entire sensor is oscillating at various heights.

While the static pressure changes may be small at these scales, it's great enough to drastically affect the spectral content of an acquired acoustic signal. The experimental results suggest that there are at least three factors at play in seismo-acoustic interactions:

1. Vibrations of the diaphragm itself, or oscillations of the air surrounding the diaphragm
2. Vibrations of the tubing routed to the pressure transducer inlet
3. Vibrations cause a change in height, which results in an oscillating static pressure reading

Each of the factors in the list above can be seen in Figure 54. To re-iterate, the 3rd item in the list above is the most likely source of seismo-acoustic coupling based on the work in this thesis. For example, consider a displacement of 1.5 mm, which all testing platforms used in this thesis were capable of producing. The static pressure change due to a 1.5 mm height displacement is 0.018 Pa, and a 10-minute long simulated 15 Hz pressure signal of this sort is produced and plotted, along with the power spectral density of the signal, in Figure 55. Additionally, an approximation of the self-nose floor of CLASP is plotted in this figure (data collected during the experiment shown in Section 5.1.1) The majority of the spectral content in Figure 55 is around -100 dB because, relative to 20 μPa, no frequency other than 15 Hz is contributing. However, at 15 Hz, the PSD results show nearly 80 dB. Thus, pressure changes due to a displacement as small as 1.5 mm over a 10-minute period hold enough spectral energy to easily overcome the noise floor and show up in the experimental data presented in this thesis.

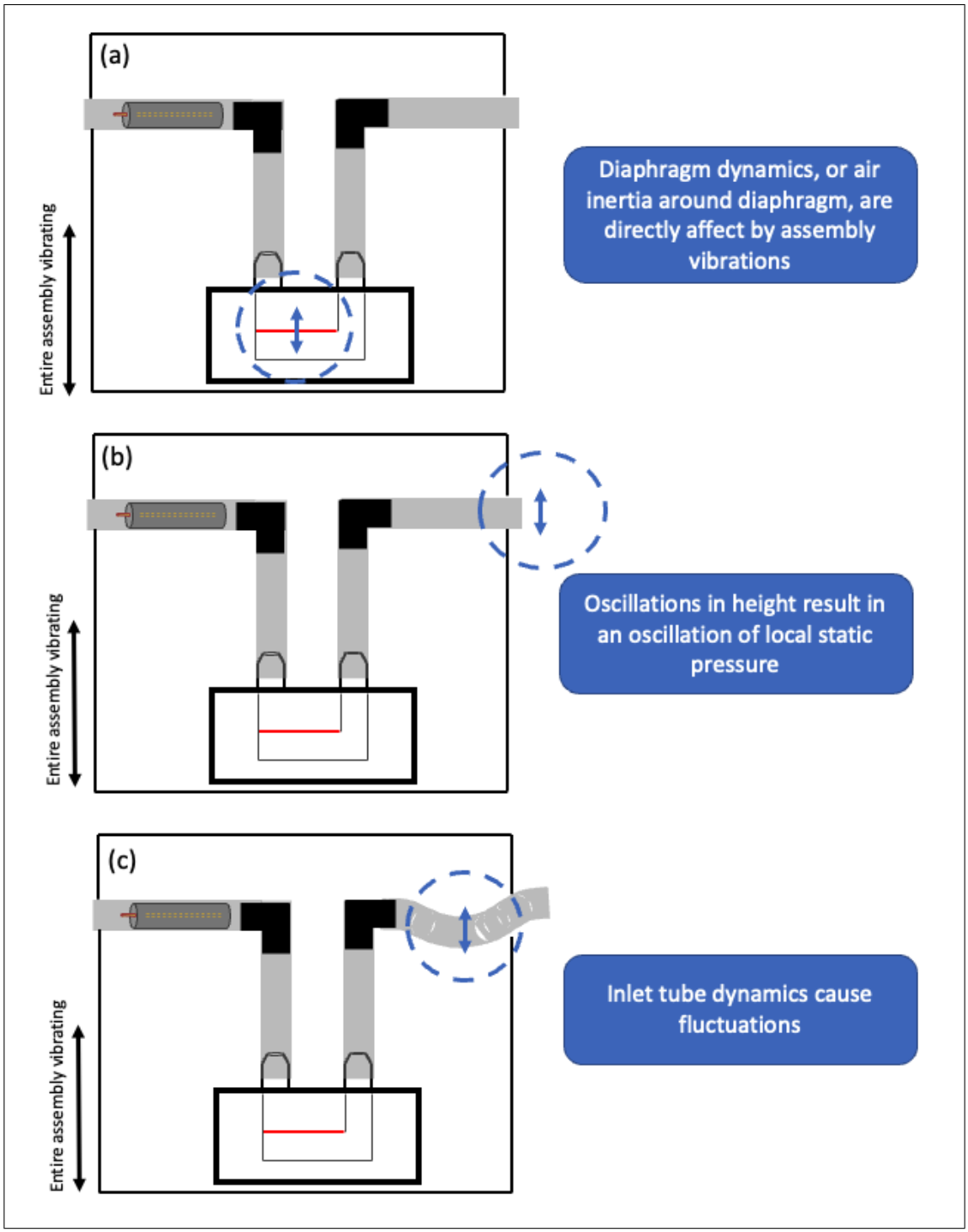

Figure 54: Hypothesized causes of seismo-acoustic coupling in low-cost sensors (sensor internal components are extremely simplified in this figure).

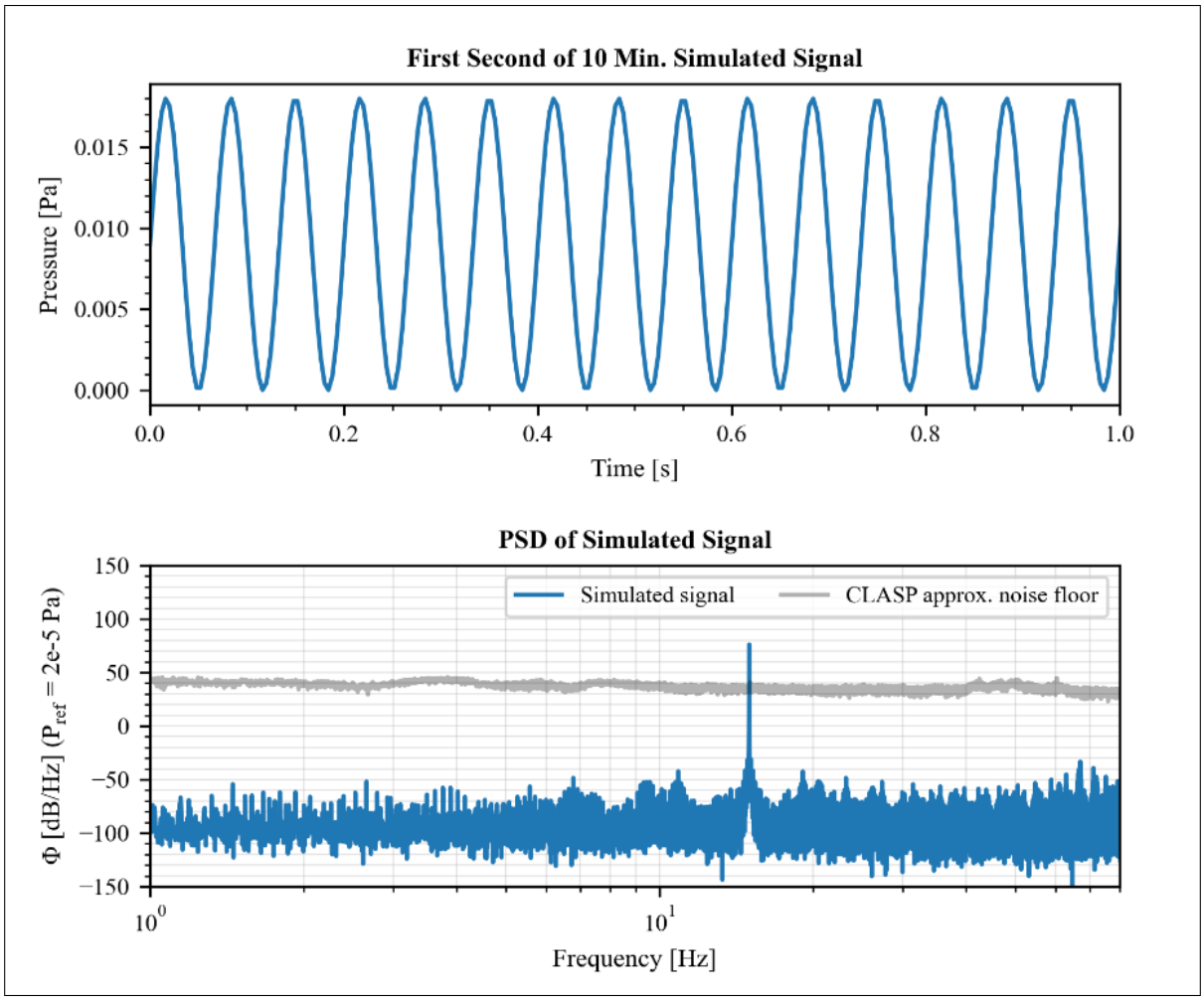

Figure 55: Simulated PSD of 15 Hz signal from 1.5mm height oscillation.

The points mentioned previously can be consolidated into three main takeaways. First, researchers should take measures to reduce unwanted seismo-acoustic coupling; diaphragm orientation and sensor component dynamics can have an impact. Second, an estimation of the height displacements a sensor will be exposed to needs to take place. If the sensor will be exposed to static pressure changes that, in the frequency domain, overwhelm a signal of interest, additional measures need to be taken; the effect shown in Figure 54b will make extracting results from data collected extremely difficult or impossible. Lastly, and most importantly, any infrasound measurements taken in vibrationally active environments need to be accompanied by data from an embedded IMU or accelerometer. Ultimately, the validity of acoustic data collected by infrasound sensors in mobile/seismic environments should not be confirmed without providing the spectral content of the accelerations experienced by the sensor.

6.2 Limitations and Future Work

As previously shown, the work presented in this thesis was broken up into sections that described CLASP and sections that investigated the impact of vibrations on mobile infrasound measurements. Thus, comments about limitations and future work are organized accordingly.

6.2.1 CLASP

CLASP is located in a unique space among other infrasound sensors. The impact of its price point and customizability cannot be overstated, but the use of off-the-shelf components comes at a cost. The noise floor of CLASP is higher, and the resolution is coarser, than existing proprietary options (mentioned in Table 4) which is understandable considering the price/unit difference between CLASP and other options. Ultimately, CLASP *can* provide utility as a stand-alone sensor, but will thrive more so in an array configuration. The

potential of using multiple CLASP units in an array should be explored; CLASP will likely have a higher return of investment, so to speak, when using multiple units in this manner.

Additionally, there are two desired functionalities of which haven't been implemented on CLASP yet: logging and a real-time interface. With only a few units in the field, logging is not crucial (but would be helpful). Considering a 6-sensor array of CLASP units would cost less than one of the sensors used in OSU1, though, it's likely that the number of CLASP units on-hand will grow. More units means more potential for issues to arise and those issues could be solved much quicker if CLASP had an extensive status/error log functionality. The real-time interface is a less important goal; but if implemented, would standardize monitoring and data visualization. The user deploying a CLASP unit could go about this task however they would like (a testament to open source projects) but a standardized real-time interface framework would place CLASP into a category of its own.

6.2.2 Infrasound Measurements in Seismic Environments

Section 6.1 discussed the limitations of mobile infrasound sensing, but there may be post-processing approaches that could help recover the acoustic data collected by sensors in seismic environments. For example, the acceleration data from an IMU could be integrated twice to deduce displacement values. From displacement, a corresponding pressure signal could be constructed and filtered out of the raw acoustic data collected by the sensor. However, there are a few major challenges with this task. One issue is that data collected by an affordable IMU is notoriously noisy and integration errors are unavoidable without the use of finely-tuned filters. Additionally, it is unclear if this technique would completely preserve the purely acoustic data as the phase between the vibrations and acoustic signal would be necessary information. Nevertheless, this approach should be explored in future endeavors.

Another limiting component of the mobile infrasound measurements presented in this thesis is simple: data has only been collected from one platform at a time. Consider CLASP in an application similar to the GLINDA systems except with multiple CLASP units deployed

at once; all in separate vehicles. They all would be affected by seismo-acoustic coupling in each sensors' respective vehicle, but the vibrations imposed on each sensor would vary (depending on each vehicle location, current road condition, etc.). Then, the coherence between all sensors could be utilized and may counteract the unique vibrations imposed on each sensor. The author of this thesis strongly encourages those who continue this work to attempt a coherence-based approach utilizing multiple CLASP units.

REFERENCES

[1] B R Elbing, C E Petrin, and M S Van Den Broeke. Measurement and characterization of infrasound from a tornado producing storm. *Journal of the Acoustical Society of America*, 146(3):1528, 1540, 2019.

[2] Trevor C. Wilson, Christopher E. Petrin, and Brian R. Elbing. Infrasound and Low-Audible Acoustic Detections from a Long-Term Microphone Array Deployment in Oklahoma. *Remote sensing (Basel, Switzerland)*, 15(1455):1455–, 2023.

[3] J. B. Johnson. Generation and propagation of infrasonic airwaves from volcanic explosions. *Journal of volcanology and geothermal research*, 121(1-2):1–14, 2003.

[4] Jeffrey B. Johnson, J. F. Anderson, R. E. Anthony, and M. Sciotto. Detecting geyser activity with infrasound. *Journal of volcanology and geothermal research*, 256:105–117, 2013.

[5] Stephanie Mayer, Alec van Herwijnen, Giacomo Ulivieri, and Jürg Schweizer. Evaluating the performance of an operational infrasound avalanche detection system at three locations in the swiss alps during two winter seasons. *Cold regions science and technology*, 173:102962–, 2020.

[6] J. D. Assink, G. Averbuch, P. S. M. Smets, and L. G. Evers. On the infrasound detected from the 2013 and 2016 DPRK's underground nuclear tests. *Geophysical research letters*, 43(7):3526–3533, 2016.

[7] Brandon White, Bryce Lindsey, Imraan Faruque, and Brian Elbing. Infrasound measurements of tornadoes and other severe storm events at close range. *Journal of the Acoustical Society of America*, 148(4):2492–2492, 2020.

[8] Brandon C. White. Measurement and Magnitude-Based System Identification of Tornado-Associated Infrasound. Master's thesis, Oklahoma State University, 2020.

[9] Duccio Gheri, Emanuele Marchetti, Giacomo Belli, Alexis Le Pichon, Vincent Boulenger, Patrick Hupe, Lars Ceranna, Pierrick Mialle, and Philippe Hereil. Monitoring of Indonesian volcanoes with the IS06 infrasound array. *Journal of volcanology and geothermal research*, 434:107753–, 2023.

[10] Alfred J. Bedard Jr and Thomas M. Georges. Atmospheric infrasound. *Physics today*, 53(3):32–37, 2000.

[11] J. Paul Mutschlechner and Rodney W. Whitaker. Infrasound from earthquakes. *Journal of Geophysical Research*, 110(D1), 2005.

[12] P. Campus and D. R. Christie. Worldwide observations of infrasonic waves. In *Infrasound Monitoring for Atmospheric Studies*, pages 185–234. Springer Netherlands, Dordrecht, 2009.

[13] Christoph Pilger, Lars Ceranna, Alexis Le Pichon, and Peter Brown. Large meteoroids as global infrasound reference events. In *Infrasound Monitoring for Atmospheric Studies*, pages 451–470. Springer International Publishing, Cham, 2018.

[14] Christopher E. Petrin and Brian R. Elbing. Infrasound emissions from tornadoes and severe storms compared to potential tornadic generation mechanisms. *Proceedings of Meetings on Acoustics*, 36(1):045005, 2019.

[15] C. P. Haynes and C. Millet. A sensitivity analysis of meteoric infrasound. *Journal of geophysical research. Planets*, 118(10):2073–2082, 2013.

[16] ABDUL JABBAR ABDULLAH. The "musical" sound emitted by a tornado. *Monthly weather review*, 94(4):213–220, 1966.

[17] Arthur Lacroix, Thomas Farges, Régis Marchiano, and François Coulouvrat. Acoustical measurement of natural lightning flashes: Reconstructions and statistical analysis of energy spectra. *Journal of geophysical research. Atmospheres*, 123(21):12,040–12,065, 2018.

[18] Arnesha Threatt. Investigation of natural and anthropomorphic sources of atmospheric infrasound. Master's thesis, Oklahoma State University, 2014.

[19] Yury S Rybnov, Alexander A Spivak, Vladimir A Kharlamov, and Andrey V Soloviev. Infrasound noises of megapolis. In *Proceedings of SPIE - The International Society for Optical Engineering*, volume 10833, pages 1083372–1083372–7. SPIE, 2018.

[20] J. Paul Mutschlechner and Rodney W. Whitaker. Propagation of near-infrasound over long ranges. Los Alamos, N.M, 1986. Los Alamos National Laboratory.

[21] J F Anderson and J B Johnson. The gem infrasound logger: A lightweight, low-power, low-cost, open-source infrasound logger. In *Graduate Student Showcase*, Boise, ID, 2018. Boise State University.

[22] Chaparral Physics. Model 20 / 24 infrasound sensor. `http://chaparralphysics.com/specs/specs_model_20_24-2015.pdf`, 2015.

[23] Infiltec. The inexpensive infrasound monitor project. `http://www.infiltec.com/Infrasound@home/`, 2022.

[24] Chaparral Physics. Model 60 tactical infrasound sensor (patent pending). `http://chaparralphysics.com/specs/specs_model60_2015.pdf`, 2015.

[25] Bion John Merchant and Randy K. Rembold. 2020 hyperion infrasound sensor equilibration evaluation. 2021. `https://www.osti.gov/biblio/1819811`.

[26] Brüel & Kjær. Product data - 1/2" pressure-field microphone type 4193. https://www.bksv.com/-/media/literature/Product-Data/bp2214.ashx, 2008.

[27] Allan J. Zuckerwar. Measurements, Acoustical. In *digital Encyclopedia of Applied Physics*. John Wiley & Sons, Ltd, 2003.

[28] Jonathan Walsh. *Vibration Signals in Sub-Miniature Microphones: Prediction and Measurement*. PhD thesis, Binghamton University, 2021.

[29] Charles B. King. Microphone vibration sensitivity: What it is, why it is important, and how to measure it. *The Journal of the Acoustical Society of America*, 152(4):A234–A234, 2022.

[30] Patent issued for method and apparatus for active reduction of mechanically coupled vibration in microphone signals (uspto 11153487), 2021.

[31] Bion J. Merchant. 2019 hyperion 5313a and 5119a infrasound sensor type approval evaluation. 2 2020. https://www.osti.gov/biblio/1601758.

[32] Experimental flow physics lab - home page. http://www.flowphysicslab.org/. Accessed: 2022-09-30, Published: 2016.

[33] B White, B Lindsey, B Elbing, and I Faruque. Infrasound measurements of tornadoes and other severe storm events at close range. In *73rd Annual Meeting of the APS Division of Fluid Dynamics*, Chicao, IL (virtual), 2020. American Physical Society.

[34] NOAA US Department of Commerce. April 29th 2022 tornadoes - including the Andover tornado. https://www.weather.gov/ict/event_20220430, Sep 2022.

[35] Val Castor and Amy Castor. Tracking tornado producing storm near Andover, Kansas. https://www.facebook.com/ValCastorNews9/videos/watch-live-tracking-tornado-producing-storm-near-andover-kansas/529999532139293, Apr 2022.

[36] Jacob F. Anderson, Jeffrey B. Johnson, Daniel C. Bowman, and Timothy J. Ronan. The gem infrasound logger and custom-built instrumentation. *Seismological research letters*, 89(1):153–164, 2018.

[37] Daniel C. Bowman and Siddharth Krishnamoorthy. Infrasound from a buried chemical explosion recorded on a balloon in the lower stratosphere. *Geophysical Research Letters*, 48(21), 2021.

[38] Arendal Sound. *1723 avalanche 800/1200 IQ*, 2020. Version 2.

[39] Vibration Therapeutic. *Model VT007 User Manual & Tech Specs*, 2017. SpecsPro LLC.

[40] Unmanned Systems Research Institute. `https://ceat.okstate.edu/mae/research/usri/`, 2023. Accessed: 2023-1-11.

[41] James Brenner. Inflow analysis for multi-rotors and the impact on sensor placement. Master's thesis, Oklahoma State University, 2019.

[42] P. Welch. The use of fast fourier transform for the estimation of power spectra: A method based on time averaging over short, modified periodograms. *IEEE transactions on audio and electroacoustics*, 15(2):70–73, 1967.

[43] Alan V. Oppenheim. *Discrete-time signal processing*. Prentice Hall signal processing series. Pearson, Upper Saddle River, 3rd ed. edition, 2010.

[44] E. Oran Brigham. *The Fast Fourier Transform and Its Applications*. Prentice-Hall, Inc., USA, 1988.

[45] Tarun Kumar Rawat. *Digital signal processing*. Oxford University Press, New Delhi, India, 2015.

[46] E. Oran Brigham. *The fast Fourier transform*. Prentice-Hall, Englewood Cliffs, N.J, 1974.

[47] M. S. Bartlett. Periodogram analysis and continuous spectra. *Biometrika*, 37(1-2):1–16, 1950.

[48] Tom Irvine. Power spectral density handbook. `https://endaq.com/pages/power-spectral-density`, 2019.

[49] Petrus M.T. Broersen. *Automatic Autocorrelation and Spectral Analysis*. Springer London, London, 1st ed. 2006. edition, 2006.

[50] Patrick Jungwirth. Power spectral density and hilbert transform, Dec 2016.

[51] Gerhard Heinzel, A. O. Rüdiger, and Roland Schilling. Spectrum and spectral density estimation by the Discrete Fourier transform (DFT), including a comprehensive list of window functions and some new at-top windows. 2002.

[52] Ricardo Gutierrez-Osuna. Short-time fourier analysis and synthesis. Texas A&M University, 2019. `https://vnit.ac.in/ece/wp-content/uploads/2019/10/STFT_analysis_synthesis.pdf`.

[53] Otis Solomon. *PSD computations using Welch's method. [Power Spectral Density (PSD)]*. United States. Dept. of Energy, Washington, D.C, 1991 - 1201.

[54] Mendel Kleiner. *Acoustics and Audio Technology (3rd Edition)*. J. Ross Publishing, Inc, 2012.

[55] Guido Van Rossum and Fred L. Drake. *Python 3 Reference Manual*. CreateSpace, Scotts Valley, CA, 2009.

[56] Fundamental algorithms for scientific computing in python. `https://docs.scipy.org/doc/scipy/`, 2023.

[57] ALL SENSORS. *ADCX Series Millivolt Output Pressure Sensors*, 2023. Rev. C.

[58] R. W. Whitaker and J. P. Mutschlecner. *The design and operation of infrasonic microphones*. United States. Dept. of Energy, Washington, D.C, 1997 - 0501.

[59] D. H. Keefe. Acoustical wave propagation in cylindrical ducts: Transmission line parameter approximations for isothermal and nonisothermal boundary conditions. *Journal of the Acoustical Society of America*, 75(1):58–62, 1984. Cited By :168.

[60] O Marcillo, J B Johnson, and D Hart. Implementation, characterization, and evaluation of an inexpensive low-power low-noise infrasound sensor based on a micromachined differential pressure transducer and a mechanical filter. *Journal of Atmospheric and Oceanic Technology*, 29(1):1275, 1284, 2012.

[61] Texas Instruments. *INA118 Precision, Low-Power Insrumentation Amplifier*, 2022. Revised Sep. 2022.

[62] Analog Devices. *Low Power, Precision, Auto-Zero Op Amps*, 2013. Rev. B.

[63] Texas Instruments. *ADS111x Ultra-Small, Low-Power, I^2C-Compatible, 860-SPS, 16-Bit ADCs With Internal Reference, Oscillator, and Programmable Comparator*, 2018. Revised Jan. 2018.

[64] Raspberry Pi (Trading) Ltd. *Raspberry Pi 4 Model B Datasheet*, 2019. Release 1.

[65] CD Technology. *CD-PA1616S GPS patch antenna module*, 2017. Rev. 4.

[66] Nick Craig-Wood. Rclone instructions. `https://rclone.org/docs/`, 2014.

[67] Bryce B. Lindsey. clasp_src. `https://github.com/brylind/clasp_src`, 2021.

[68] Michael Dowd, Keith Thompson, and Bruce Smith. Time series analysis, Jan 2004.

[69] Brian R. Elbing and Richard J. Gaeta. *Integration of Infrasonic Sensing with UAS (Invited)*.

[70] Brian R. Elbing, Christopher E. Petrin, and Matthew S. Van Den Broeke. Infrasound measurements from a tornado in Oklahoma. *Proceedings of Meetings on Acoustics*, 33(1):045003, 2018.

[71] Tatiana A. Andreeva and William W. Durgin. Wind tunnel investigation of sound attenuation in turbulent flow. *Ultrasonics*, 61:15–19, 2015.

[72] Shoichi Tanaka and Biho Shiraishi. Wind effects on noise propagation for complicated geographical and road configurations. *Applied acoustics*, 69(11):1038–1043, 2008.

APPENDICES

APPENDIX A: Supplemental Information for Methods and Equipment Used in Experiments

A.1 Shaker Table

Accelerations observed from shaker table at 21 Hz and "low" amplitude setting can be seen in Figure 56. "Vertical", "longitudinal", and "lateral" are acceleration directions perpendicular to the table, along the length of the table, and along the width of the table, respectively.

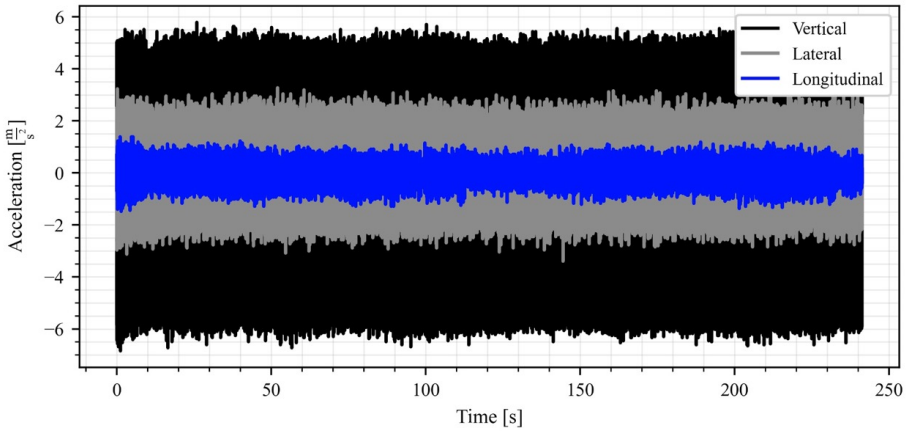

Figure 56: Shaker table observed accelerations.

A.2 UAV

The nominal payload on-board the UAV used during experiments can be seen in Figure 57.

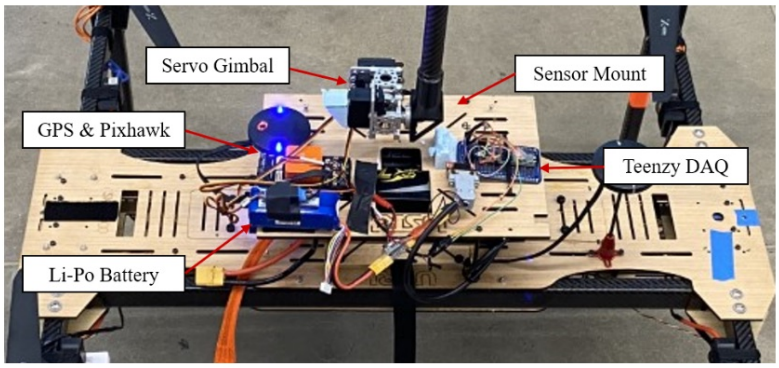

Figure 57: UAV nominal payload.

APPENDIX B: Supporting CLASP Design and Setup Procedures

B.1 CLASP PCB Schematic

Figure 58 shows the schematic of CLASP's PCB.

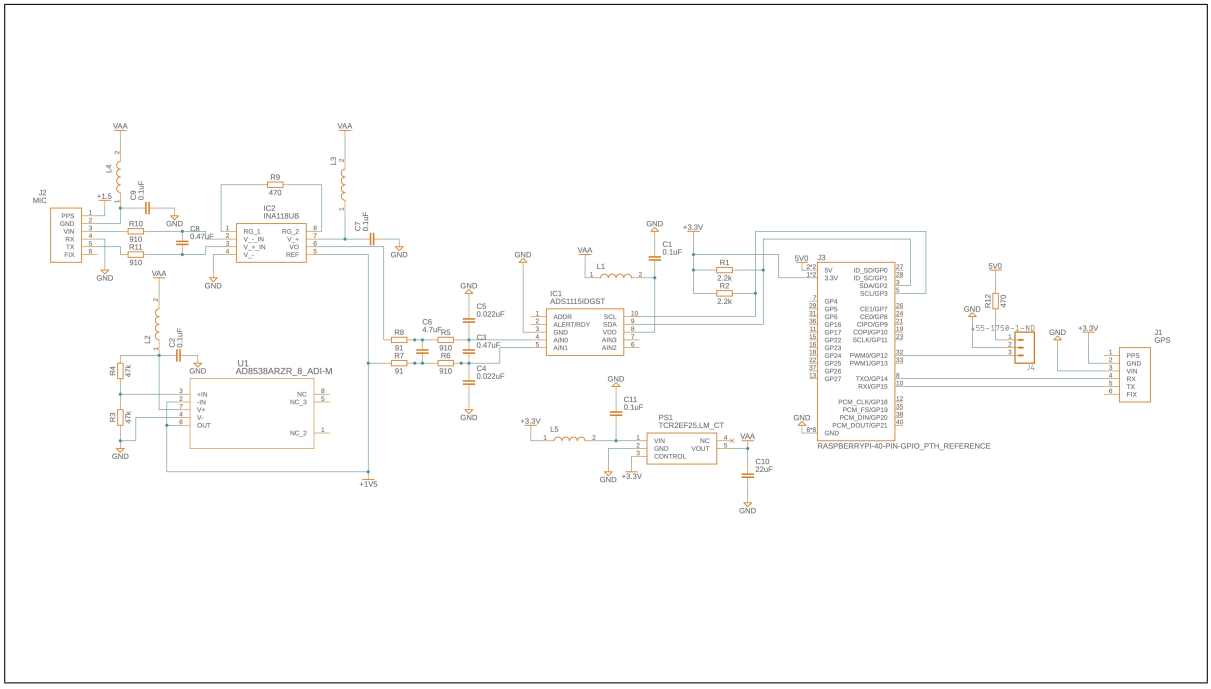

Figure 58: CLASP PCB detailed schematic.

B.2 CLASP Source-code Required Packages

The required Python packages to execute CLASP's source-code can be seen in Table 16. Most of these packages are not directly imported, but are dependencies of imported packages.

Adafruit-Blinka==8.10.0	pexpect==4.8.0	docutils==0.16
adafruit-circuitpython-ads1x15==2.2.21	pgzero==1.2	drumhat==0.1.0
adafruit-circuitpython-adxl34x==1.12.8	phatbeat==0.1.1	envirophat==1.0.0
adafruit-circuitpython-busdevice==5.2.3	pianohat==0.1.0	ExplorerHAT==0.4.2
adafruit-circuitpython-gps==3.10.7	picamera==1.13	Flask==1.1.2
adafruit-circuitpython-requests==1.12.11	piglow==1.2.5	fourletterphat==0.1.0
adafruit-circuitpython-typing==1.8.3	pigpio==1.78	gpiozero==1.6.2
Adafruit-PlatformDetect==3.38.0	Pillow==8.1.2	html5lib==1.1
Adafruit-PureIO==1.1.9	psutil==5.8.0	idna==2.10
arandr==0.1.10	pycairo==1.16.2	isort==5.6.4
astroid==2.5.1	pycups==2.0.1	itsdangerous==1.1.0
asttokens==2.0.4	pyftdi==0.54.0	jedi==0.18.0
automationhat==0.2.0	pygame==1.9.6	Jinja2==2.11.3
beautifulsoup4==4.9.3	Pygments==2.7.1	lazy-object-proxy==0.0.0
blinker==1.4	PyGObject==3.38.0	logilab-common==1.8.1
blinkt==0.1.2	pyinotify==0.9.6	lxml==4.6.3
buttonshim==0.0.2	PyJWT==1.7.1	MarkupSafe==1.1.1
Cap1xxx==0.1.3	pylint==2.7.2	mccabe==0.6.1
certifi==2020.6.20	pyOpenSSL==20.0.1	microdotphat==0.2.1
chardet==4.0.0	pyserial==3.5b0	mote==0.0.4
click==7.1.2	pysmbc==1.0.23	motephat==0.0.3
colorama==0.4.4	python-apt==2.2.1	mypy==0.812
colorzero==1.1	pyusb==1.2.1	mypy-extensions==0.4.3
cryptography==3.3.2	rainbowhat==0.1.0	numpy==1.19.5
cupshelpers==1.0	reportlab==3.5.59	oauthlib==3.1.0
dbus-python==1.2.16	requests==2.25.1	olefile==0.46
distro==1.5.0	requests-oauthlib==1.0.0	pantilthat==0.0.7
responses==0.12.1	sense-hat==2.4.0	parso==0.8.1
roman==2.0.0	simplejson==3.17.2	toml==0.10.1
rpi-ws281x==4.3.4	six==1.16.0	touchphat==0.0.1
RPi.GPIO==0.7.0	skywriter==0.0.7	twython==3.8.2
RTIMULib==7.2.1	sn3218==1.2.7	typed-ast==1.4.2
scrollphat==0.0.7	soupsieve==2.2.1	typing-extensions==4.4.0
scrollphathd==1.2.1	spidev==3.5	unicornhathd==0.0.4
Send2Trash==1.6.0b1	ssh-import-id==5.10	urllib3==1.26.5
wrapt==1.12.1	sysv-ipc==1.1.0	webencodings==0.5.1
	thonny==3.3.14	Werkzeug==1.0.1

Table 16: Packages required by CLASP.

B.3 Commands and Inputs Required for CLASP i^2c Speeds and GPS Module Communication

The configuration file located at /boot/config.txt on the Raspberry Pi 4 is used to adjust many system-level parameters. One of which is the i^2c connection speeds utilized by all sensors of the CLASP package other than the GPS module. To increase the i^2c connection speed to, say, 400 kB/s, implement the text starting with "i2c_arm_baudrate" seen in Figure 59. 400 kB/s is the speed CLASP utilizes in order to sample the the microphone's digitized signal and the accelerometer's digitized signal at 250 Hz and 400 Hz, respectively.

```
# Uncomment some or all of these to enable the optional hardware interfaces
dtparam=i2c_arm=on, i2c_arm_baudrate=400000
#dtparam=i2s=on
```

Figure 59: Command to increase i^2c speed on Raspberry Pi 4.

While not necessary, disabling the on-board Bluetooth can help prioritize the UART connection of the GPS module that CLASP uses. To accomplish this, one must open the configuration file located at /boot/config.txt and add the text seen in Figure 60.

```
# disable bluetooth to give GPS breakout serial priority
dtoverlay=disable-bt
```

Figure 60: Command to disable on-board Bluetooth on Raspberry Pi 4.

Additionally, in order for the current user ("pi" on CLASP, as that is the default username) to have access to the serial port used to communicated with the GPS module, the user needs to be added to the "tty" and "dialout" groups. The easiest way to accomplish this is to open an active terminal on the Raspberry Pi and enter the commands in Table 17.

Command	Description
sudo usermod -a -G dialout <username>	Adds user of choice to dialout group (requires super-user permissions)
sudo usermod -a -G tty <username>	Adds user of choice to tty group (requires super-user permissions)

Table 17: Terminal commands required to add user to tty and dialout groups.

B.4 CLASP service files

Service files should be placed in "/etc/systemd/systemd" directory. The contents of the service file that starts the Python script which starts the rclone program can be seen in Figure 61, and the service file that attempts a git pull and also runs the Python scripts that start data acquisition among all sensors can be seen in Figure 62.

```
pi@GLINDAproto:/etc/systemd/system $ cat rclone_autopush.service
[Unit]
Description=Uses rclone to push data continuously to google drive
After=multi-user.target

[Service]
Type=idle
User=pi
ExecStart=/usr/bin/python3 /home/pi/glinda_main/src/rclone_autopush.py
Restart=always
RestartSec=3

[Install]
WantedBy=multi-user.target
```

Figure 61: Systemd service that initiates rclone script on CLASP.

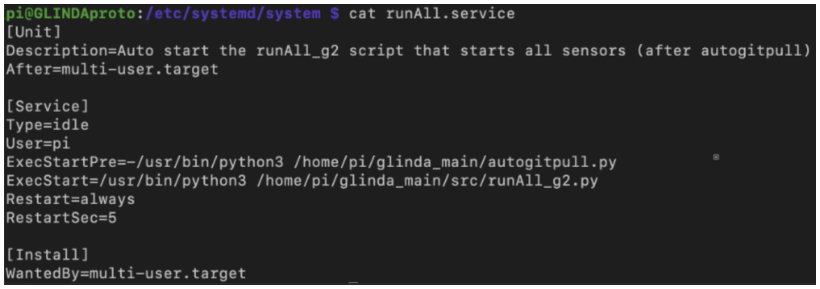

Figure 62: Systemd service that initiates git pull and data acquisition Python scripts on CLASP.

Lastly, after the formation of services, one needs to enable and reload the systemd services. The two commands required to accomplish this task can be seen in Table 18.

Command	**Description**
sudo systemctl enable <service file name>.service	Enables the service of choice (requires super-user permissions)
sudo systemctl deamon-reload	Reloads systemd services (requires super-user permissions), required after changes to systemd directory

Table 18: Terminal commands required to configure CLASP service files.

APPENDIX C: Supplemental Materials from Experiments

C.1 Plugged Inlets

Figures 63 and 64 show the configuration "1" and "2" of the shaker table experiment with plugged pressure transducer ports. Figure 65 shows the noise floor collected while GLINDA2 and CLASP were acoustically-isolated (plugged ports) and not experiencing any vibration input (this data was used for the VCR metric).

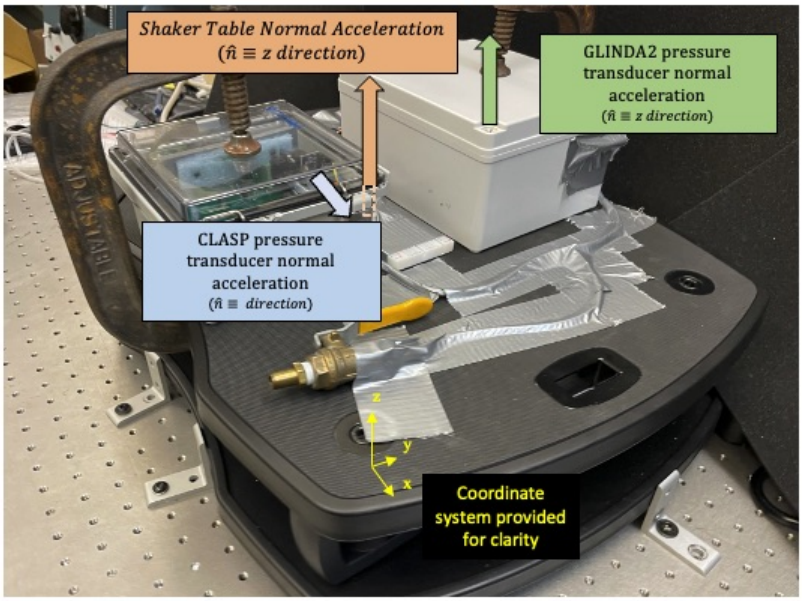

Figure 63: Configuration 1 - Vibration test with inlets plugged.

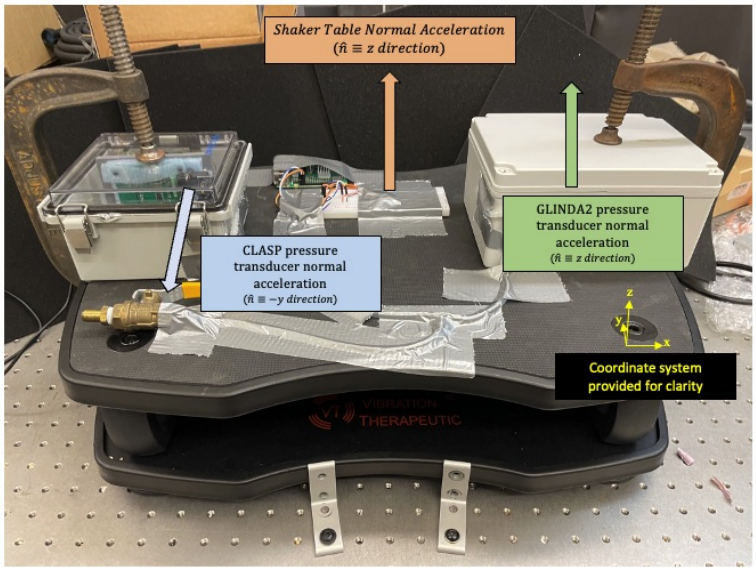

Figure 64: Configuration 2 - Vibration test with inlets plugged.

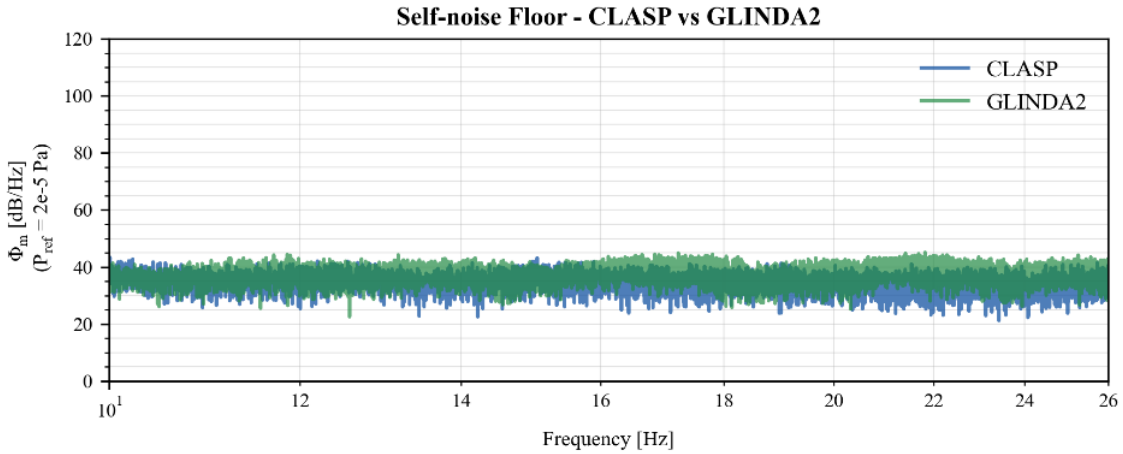

Figure 65: Self-noise collected during plugged test (no vibrations) used for noise floor reference.

C.2 Nominal Inlets (unplugged)

Figures 66, 67, and 68 show images taken during the unplugged acoustic inlet shaker table tests.

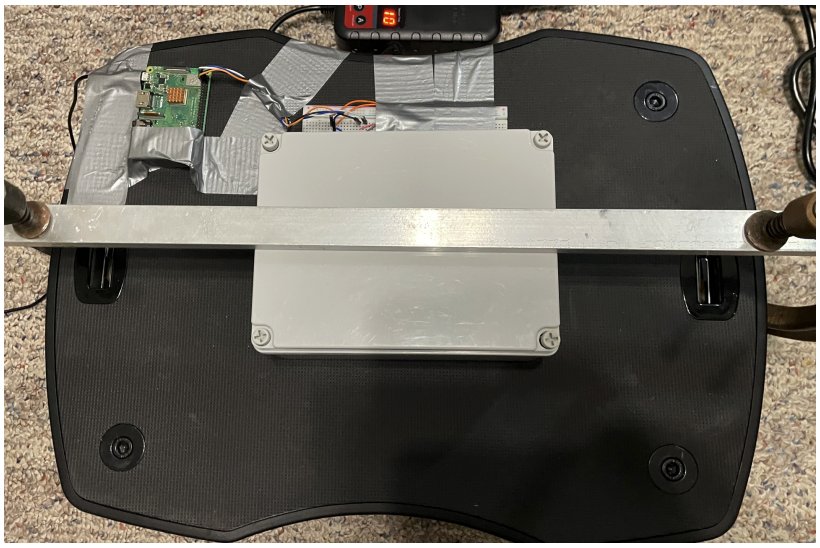

Figure 66: Vibration test with nominal inlets - GLINDA 2.

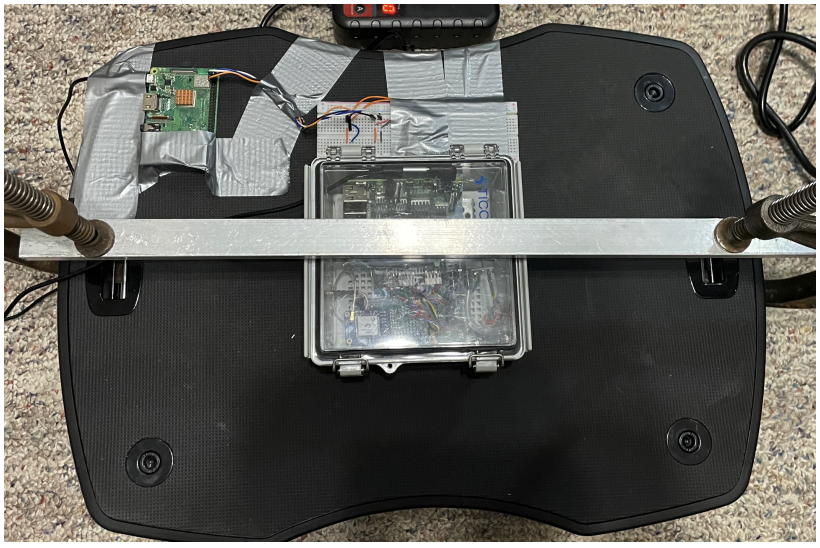

Figure 67: Vibration test with nominal inlets - CLASP.

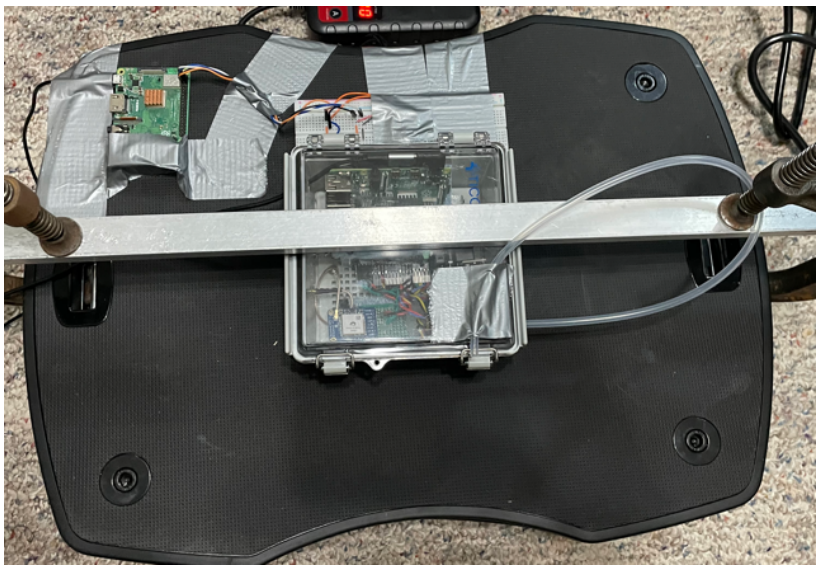

Figure 68: Vibration test with nominal inlets - CLASP with long inlet hose.

C.3 Vehicle-based test

Figure 69 shows the different road sections driven during the vehicle-based vibration experiment.

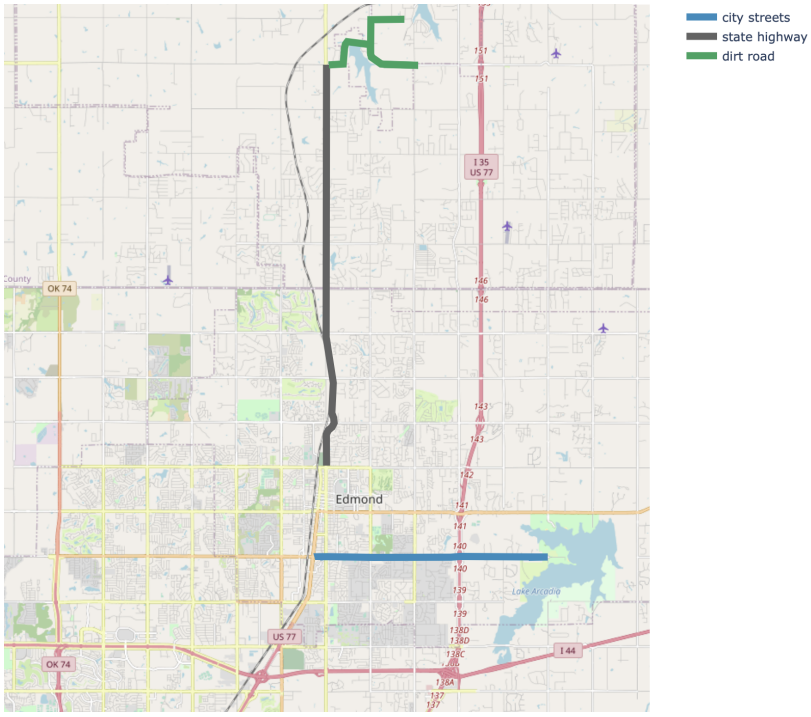

Figure 69: Routes and road types during vehicle-based test.

VITA

Bryce B. Lindsey

Candidate for the Degree of

Master of Science

Thesis: THE IMPACT OF VIBRATIONS ON MOBILE INFRASOUND SENSING AND THE DEVELOPMENT OF A CUSTOM SENSOR PACKAGE

Major Field: Mechanical and Aerospace Engineering

Biographical:

Education:

Completed the requirements for the Master of Science in Mechanical and Aerospace Engineering at Oklahoma State University, Stillwater, Oklahoma in May, 2023.

Completed the requirements for the Bachelor of Science in Aerospace Engineering at Oklahoma State University, Stillwater, Oklahoma in 2021.

Completed the requirements for the Bachelor of Science in Mechanical Engineering at Oklahoma State University, Stillwater, Oklahoma in 2021.

Experience:

Applied Aerodynamics Graduate Intern at Sandia National Laboratories

Research Assistant at Oklahoma State University

Active Duty Landing Support Specialist in the United States Marine Corps